

NASA TECHNICAL NOTE



NASA TN D-7612

NASA TN D-7612

**ANALYTIC AND EXPERIMENTAL EVALUATION
OF SHADOW SHIELDS AND THEIR SUPPORT
MEMBERS FOR THERMAL CONTROL
OF SPACE VEHICLES**

by Robert J. Boyle and Robert J. Stochl

*Lewis Research Center
Cleveland, Ohio 44135*



NATIONAL AERONAUTICS AND SPACE ADMINISTRATION • WASHINGTON, D. C. • JUNE 1974

1. Report No. NASA TN D-7612	2. Government Accession No.	3. Recipient's Catalog No.	
4. Title and Subtitle ANALYTIC AND EXPERIMENTAL EVALUATION OF SHADOW SHIELDS AND THEIR SUPPORT MEMBERS FOR THERMAL CONTROL OF SPACE VEHICLES		5. Report Date June 1974	6. Performing Organization Code
		8. Performing Organization Report No. E-7344	
7. Author(s) Robert J. Boyle and Robert J. Stochl		10. Work Unit No. 502-24	11. Contract or Grant No.
9. Performing Organization Name and Address Lewis Research Center National Aeronautics and Space Administration Cleveland, Ohio 44135		13. Type of Report and Period Covered Technical Note	
		14. Sponsoring Agency Code	
12. Sponsoring Agency Name and Address National Aeronautics and Space Administration Washington, D.C. 20546		15. Supplementary Notes	
16. Abstract The thermal performance of shadow shields, and their support struts, for the thermal protection of cryogenic propellants in a simulated deep-space environment was investigated analytically and experimentally. Very low overall heat-transfer rates were obtained when highly reflective aluminized Mylar shadow shields were used. The thermal interactions between the shields and support struts were investigated with fair to good agreement between the analysis and experimental data. The exterior surface of both fiberglass and titanium struts was coated to reduce the heat input into the test tank. The vacuum level inside the test facility strongly influenced the heat-transfer rates.			
17. Key Words (Suggested by Author(s)) Thermal performance Shadow shields Spacecraft, cryogenics		18. Distribution Statement Unclassified - unlimited Category 33	
19. Security Classif. (of this report) Unclassified	20. Security Classif. (of this page) Unclassified	21. No. of Pages 136	22. Price* \$4.75

CONTENTS

	Page
<u>SUMMARY</u>	1
<u>INTRODUCTION</u>	2
<u>EXPERIMENTAL APPARATUS</u>	3
FACILITY	3
TEST CONFIGURATION	4
INSTRUMENTATION	6
<u>PROCEDURE</u>	8
<u>METHOD OF ANALYSIS</u>	8
STRUTS	9
SHIELDS IN PRESENCE OF STRUTS	10
RING BETWEEN SHEETS OF A SHIELD	13
ANALYTIC MODEL	13
<u>RESULTS AND DISCUSSION</u>	15
TESTS WITHOUT SHIELDS	15
Insulated Struts	16
Half-Black and All-Black Struts	17
Titanium with hydrogen	17
Titanium with nitrogen	18
Effect of strut end plug	19
Fiberglass with hydrogen	19
Fiberglass with nitrogen	20
Heat-Transfer Results	21
TEST WITH SHIELDS	23
Shield and Strut Temperatures	24
Twelve fiberglass struts, evenly spaced shields	25
Eleven titanium struts, evenly spaced shields	29
Eleven titanium struts, closely spaced shields	30
Heat-Transfer Rates with Shields	33
Heat transfer by gaseous conduction	33
Comparison of heat-transfer rates	35
<u>CONCLUDING REMARKS</u>	37
<u>SUMMARY OF RESULTS</u>	37
APPENDIXES	
A - SYMBOLS	40

B - DERIVATION OF THERMAL ENERGY EQUATIONS	43
Solution of Equations	52
Determination of script \mathcal{F} 's	52
Determination of view factors	57
Radial sheet conduction	58
Effect of the Number of Nodes	58
Appropriateness of a Planar Tank Surface	59
C - SHIELD ANALYSIS BASED ON DIRECTIONAL PROPERTIES	60
Description of Analysis	60
Case I - ray strikes wall	63
Case II - ray strikes other end	66
Application of Equations	67
D - ANALYSIS FOR GASEOUS CONDUCTION	69
Free Molecular Flow	70
Case I - two surfaces	70
Case II - three or more surfaces	74
<u>REFERENCES</u>	78

ANALYTIC AND EXPERIMENTAL EVALUATION OF SHADOW SHIELDS AND THEIR SUPPORT MEMBERS FOR THERMAL CONTROL OF SPACE VEHICLES

by Robert J. Boyle and Robert J. Stochl

Lewis Research Center

SUMMARY

The thermal performance of shadow shields, and their support struts, for the thermal protection of cryogenic propellants in a simulated space environment was investigated analytically and experimentally. The results of this investigation are applicable to space vehicles which are primarily sun oriented with the cryogen in the shadow of a warm payload. The shields are between the payload and tank and promote the reflection of energy to the cold background of space. Tests were conducted in a vacuum chamber having high-absorptivity, liquid-hydrogen-cooled walls. A single heat source operated at 294 or 389 K (530⁰ or 700⁰ R) simulated the payload, while either liquid hydrogen or liquid nitrogen was used in the tank as the cryogen. Heat-transfer rates and temperature profiles were obtained for the following configurations: (1) twelve 2.22-centimeter (0.875-in.) diameter titanium and fiberglass struts, without shadow shields; (2) two 1.35-meter (53-in.) diameter shadow shields inserted between the heater and the test tank in addition to the 12 struts. Configuration 1 was used to determine the effects of thermal conductivity and exterior coating, and configuration 2 to determine the strut-shield interaction and the effects of spacing between the shields and heater.

The analytic and experimental strut temperatures without shields showed good agreement. However, there was some underprediction of the strut temperatures near the tank. There was good agreement between the predicted and experimental heat-transfer rates after the nongray absorptivity of the tank surface was accounted for.

Inserting two shadow shields between the heater and test tank reduced the measured heat-transfer rate by a factor of nearly 30. Each shield, formed by stretching two highly reflective sheets across a support ring, reflected much of the energy to the highly absorbing cold walls.

Generally, there was good agreement between the predicted and experimental strut and shield temperatures except for the cold sheet of the warm shadow shield, where there was a significant overprediction. The agreement for the cold shield was improved by using directional properties for the aluminized sheets.

INTRODUCTION

For long-duration interplanetary missions involving cryogenic propellants, it becomes necessary to reduce the heat flux into the propellant tanks to extremely low values. Radiation heat transfer is very significant in the vacuum of space. At the present time there are two forms of radiation barriers which can effectively reduce radiant heat transfer: (1) multilayer insulation, which consists of closely spaced radiation barriers separated by low-conducting spacers; (2) shadow shields, also consisting of radiation barriers but spaced further apart so as to allow heat to escape to the surrounding low-temperature space environment. Studies reported in references 1 to 3 have shown that if the major radiant heat load is from one direction, such as it would be if a spacecraft were sun oriented, the use of shadow shields can provide performance which is superior to that of an equal number of closely spaced shields (multilayer insulation).

To date, analytic and experimental studies of shadow shield performance (refs. 4 and 5) have been largely confined to the consideration of shields not connected to supports and of supports not connected to the shields. Thus, the heat transfer and temperature through the shields and supports have been separately verified. However, the thermal interaction between shields and supports had not been defined analytically or verified experimentally.

Therefore, a program was undertaken (1) to develop a detailed analysis which would include the strut-shield interaction in predicting shadow shield thermal performance; (2) to examine experimentally the effect of certain configuration variables on the performance of a scale model of a realistic shadow shield system; and (3) to use the experimental results to verify the analysis, and if necessary, to extend the analytic capabilities for predicting system performance by additions describing significant experimental findings. Reference 6 briefly describes the more important findings of this program.

Tests were performed in a vacuum on a system composed of two shadow shields supported by struts and located between a warm heat source simulating a payload and a propellant tank. Liquid hydrogen and liquid nitrogen were used to simulate the propellant. Liquid-hydrogen-cooled walls having a high-absorptivity surface coating simulated space. The heat source was maintained at a temperature of either 294 or 389 K (530^o or 700^o R).

Experimental data were obtained to determine the effect of shield spacing, strut-shield bushing material, strut material, and selective coatings of the strut surface on

the overall performance of a basic shadow shield system. The results of the analytic program are presented and compared with experimental data. The symbols used in the analysis are presented in appendix A; appendixes B, C, and D discuss the equations used.

Although test measurements were made in the U.S. customary system of units, the International System (SI) is included for reporting purposes.

EXPERIMENTAL APPARATUS

FACILITY

All tests were conducted inside a 7.61-meter (25-ft) diameter spherical vacuum chamber, shown in figure 1, to eliminate or minimize gaseous heat conduction into the test configuration. The vacuum capability of this chamber was approximately 8×10^{-7} torr at room temperature. A general schematic of a test configuration and associated equipment is shown in figure 2. The test configuration was placed inside a cylindrical, liquid-hydrogen-cooled cryoshroud. The cryoshroud was 2.44 meters (8 ft) in diameter and 2.44 meters (8 ft) in length. The inside surfaces of the cryoshroud were coated with a high-absorptivity paint to simulate the environment of deep space.

The cold guard, shown at the top of the cryoshroud in figure 2, contained the same fluid as the test tank and was used to eliminate or minimize solid-conduction heat transfer through support tubes, fill and vent lines, and instrumentation wires. This cold guard was constructed of stainless steel and had a diameter of 0.457 meter (1.5 ft) and a length of 0.482 meter (1.58 ft).

The pressures inside the test tank and the cold guard were controlled by separate closed-loop control systems capable of maintaining each pressure within 1.38×10^{-4} N/cm² (0.0002 psia) of a desired value. These pressure control systems, shown schematically in figure 2, consisted of high-resolution differential pressure transducers which sensed very small pressure variations inside the test tank and the cold guard relative to an absolute reference pressure. The electrical output signals from the transducers were transmitted to control units for electrohydraulic pressure regulating valves in the respective vent lines. The reference pressure was provided by a fixed volume of gaseous nitrogen maintained at a constant temperature by an ice bath. The pressure inside the test tank was maintained at 11.26 N/cm² (16.33 psia); the pressure inside the cold guard was maintained at 11.38 N/cm² (16.50 psia).

The rate of heat transfer to the test tank was measured in one of two ways. Each method relied on maintaining a constant pressure inside the test tank. When the heat-transfer rate was positive (into the tank) one of five mass flowmeters was used to measure the boiloff gas flow rate. The flow rate of the gas is directly proportional to

the net heat-transfer rate. The flowmeters differed in the magnitude of their full-scale reading. The meter for the smallest flow rate had a capacity of 0.00283 standard cubic meter per hour (scmh) (0.1 std. ft³/hr (scfh)) of hydrogen. Each meter differed in capacity by a factor of 10. The capacity of the smallest meter corresponds to a net heat-transfer rate of about 0.03 watt (0.1 Btu/hr) with hydrogen in the tank and to a rate seven times greater with nitrogen in the tank. When the heat-transfer rate into the tank was negative, electrical energy was dissipated by a resistor inside the tank. The rate of energy was controlled so that there was neither boiloff nor a pressure change for the tank. The electrical energy then equaled the rate at which heat was lost from the tank. Only with nitrogen as the test fluid and shields between the tank and heater was the heat-transfer rate to the tank negative. This energy loss was chiefly radiation from the tank to the hydrogen-cooled cryoshroud.

TEST CONFIGURATION

The basic configuration for a shadow shield test is shown schematically in figure 3 (a) and pictorially in figure 3(b). Except for the cold guard, all the equipment shown was obtained through a contract with Arthur D. Little, Inc., and is described in reference 7. The cold guard and the test tank were both suspended from the top of the cryoshroud. The tubular supports between the flange on the neck of the test tank and the top of the cryoshroud passed through the cold guard tank. As shown in figure 3(b), these supports and the tank neck were covered with aluminum foil to reduce their radiant interchange with the environment. The support ring was clamped to the test tank, and the struts were bolted to the support ring. The heat source was an electrically heated plate. It was attached to the struts by bushings and set screws, in the same manner as the shields, as is discussed later in this section. The 0.556-cubic-meter (19.65-ft³) copper test tank was 1.22 meters (4.0 ft) in diameter and had a wall thickness of 0.686 centimeter (0.270 in.). This tank was made by attaching a 20.3-centimeter (8.0-in.) cylindrical section to two spun heads. The exterior of the tank was also covered with aluminum foil having an emissivity of 0.03 at room temperature. With nitrogen in the tank, this foil covering reduced the amount of energy radiated from the tank. With hydrogen in the tank, the effect of stray radiant heat-transfer rates to the tank was also reduced. Also, the net heat-transfer rates to the hydrogen tank were low enough to be of the same magnitude as those desired for long-duration space missions.

An aluminum support ring was used to attach the struts to the test tank. A detail of this support ring is shown in figure 4. The struts were attached to the bottom of the ring, and the bottom of the ring was positioned 1.9 centimeters (0.75 in.) up on the cylindrical portion of the test tank. This support ring is in the shape of a Z bracket with the web being 13.3 centimeters (5.25 in.) long and forming an annular cavity around

the tank. The effect of this cavity on the heat-transfer rate is discussed in the section Heat-Transfer Results.

In each test the 12 evenly spaced tubular struts were used to suspend the heater and shadow shields, if present, from the support ring. The struts were either fiberglass or titanium and had an outside diameter of 2.22 centimeters (0.875 in.) and a nominal wall thickness of 0.038 centimeter (0.015 in.). The measured wall thickness varied between 0.038 and 0.048 centimeter (0.015 and 0.019 in.), with most of the measurements being closer to the lower value. Normally, the distance between the support ring and the heater was 0.56 meter (1.83 ft).

Figure 5(a) shows the three types of exterior surfaces used on the struts: insulated, all black, and half black.

(1) Insulated surface: The purpose of the insulation was to reduce heat transfer from the surface of the strut. Five layers of aluminized Mylar were wrapped around the exterior of the strut for its entire length. Each layer of Mylar was separated from the next by two layers of silk net.

(2) All-black surface: The purpose of the all-black surface was to allow the external surface of the strut to radiate energy to the low-temperature cryoshroud. The entire exterior of the strut was coated with a high-emissivity paint. One drawback to this approach is that the paint will also be highly absorbent to the thermal energy from a high-temperature source such as the heater.

(3) Half-black surface: The half-black surface was an attempt to compensate for the difficulty of a good emitter being a good absorber. Half of the strut had low-absorptivity aluminized Mylar tape cemented to it; the other half had the high-emissivity paint along its entire length. The inward-facing side of the strut had a good view of the heater; therefore, it was this side that had the tape applied to it. The outward-facing side viewed the cryoshroud, and it was this side which had the high-emissivity coating.

Figure 5(b) shows the internal construction of the strut. The adapter plug was used to secure the strut to the support ring. This plug was made of the same material as the strut and was 1.91 centimeters (0.75 in.) long for the titanium strut and 3.18 centimeters (1.25 in.) long for the fiberglass strut. Twenty highly reflective aluminum disks were used to reduce internal radiant heat transfer between the warm end of the strut and the cold end. These disks were held in place with aluminized tape.

The relative positions of the various strut configurations are given in the table of figure 5(c). This figure gives both the strut instrumentation patterns and their relative locations. A primary consideration in their placement was that all black struts not be in adjacent positions. The intention was to reduce the effects of direct radiant heat transfer between struts.

Figure 6(a) depicts a shadow shield, while figure 6(b) shows the general construction details of the shield. The shadow shields were 1.35 meters (53 in.) in diameter. Each

shield consisted of two sheets of nylon-reinforced, double-aluminized Mylar approximately 0.0025 centimeter (0.001 in.) thick. Reference 4 showed experimentally that the use of two sheets per shield for two shields gives an effectiveness approaching four shields each having only a single sheet. Each sheet was stretched across and laced to a 1.91-centimeter (0.75-in.) thick circular aluminum channel, as illustrated in figure 6(b). The total measured film thickness for each sheet was between 60 and 100 nanometers (600 and 1000 Å). This total includes the aluminum film on both sides of the sheet. Figure 6(b) also illustrates the method used to attach the shields to the struts. An aluminum block was attached with screws to the channel where each strut passed through the shield. A pair of split bushings were inserted between the struts and the block and secured by a set screw. Both Micarta and aluminum bushings were used to evaluate the effect of bushing material thermal conductivity on the strut temperature profile. The three Bakelite tabs shown attached to the shield ring in figure 6(a) were used as terminals for the sheet thermocouple lead wires. Heavier gage wires went from the terminal connections to the recording instruments. The possible effect of the bakelite tabs on the shield ring temperatures are discussed in the section Bushings between strut and shield ring.

The heater shown in figures 3(a) and (b) was used to simulate a payload. This heater had the same diameter as the shield and was made from a 0.32-centimeter (0.13-in.) thick aluminum plate. To accentuate the effect of the heater, the side facing the tank was coated with a high-emissivity paint. Electric heating strips were bonded to the other side of the plate, and an automatic control maintained the plate temperature setting within 2 percent of the desired value during a run. The heater was attached to the struts in the same manner as the shields were attached, except that only aluminum bushings were used.

The cryoshroud and baffles shown in figure 3(a) were used to simulate the environment of space. Both the cryoshroud and baffles were cooled by flowing liquid hydrogen through tubes welded to the surfaces. The cryoshroud inner surface and baffles were painted with a high-absorptivity paint which was not, however, perfectly black. The movable baffles were used to compensate for this. They were aligned with the heater and each shield and served to physically block stray radiation. The thickness of the inner edge of each baffle was slightly greater than the thickness of a shield.

INSTRUMENTATION

Instrumentation was provided for measuring shield, strut, and heater temperatures; temperatures at various locations on the test hardware; pressures of the test tank and cold guard; pressure level of the vacuum chamber; and vaporization rate from the test tank.

The shadow shield temperatures were obtained with copper-constantan thermocouples. Figure 6(a) shows a typical application of the thermocouples for a shield. A total of twenty-seven 40-gage (0.00762-cm (0.003-in.) diameter) thermocouples were used on each shield (seven on the exterior of both the top and bottom sheets) at various intervals across the shield radius. Six thermocouples were placed on the interior surface of one sheet, and seven were placed along the shield ring. All thermocouple lead wires were laid along isotherms for some distance before they left the shield to eliminate temperature errors caused by heat conduction through the wires. The thermocouple junctions and lead wires were covered with either aluminized Mylar or strips of sheet material to reduce any erroneous temperature measurements caused by local variations in emissivity.

The strut temperatures were obtained with 40-gage Chromel-constantan thermocouples. The locations of the thermocouples on the struts are shown in figure 5(c). The first symbol of the strut code shown in the table of this figure denotes the strut material, while the second symbol denotes the instrumentation pattern. Where there is no second symbol, the strut was not instrumented and was half black. By using different thermocouple patterns in the same test, temperatures were obtained for as many as 14 axial locations for each type of strut. Thermocouples were placed on the inward- and outward-facing sides of both the half-black and all-black struts. Each of the insulated struts was instrumented by placing three thermocouples on the body of the strut and four on the outward side of the outer layer of insulation. The strut temperatures had an uncertainty of ± 4.4 K (8° R) at liquid-hydrogen temperature. This uncertainty improved to ± 2.8 K (5° R) at liquid-nitrogen temperature and to about ± 0.6 K (1° R) at room temperature.

A total of thirteen 26-gage (0.0404-cm (0.0159-in.) diameter) copper-constantan thermocouples were used at various intervals across the heater surface.

Platinum resistance sensors were used to measure tank and cold guard wall temperatures as well as temperature inside these vessels. Platinum resistance sensors were also used for fill and vent line and cryoshroud temperatures. These sensors had an uncertainty of ± 1 percent at both liquid-hydrogen and liquid-nitrogen temperatures.

Test tank, cold guard, and line absolute pressures were measured with bonded strain-gage-type transducers which had an estimated uncertainty of $\pm 1/4$ percent.

The vacuum levels, both inside the cryoshroud and in the space between the cryoshroud and chamber wall, were determined by ionization gages.

The vaporization rate from the test tank was metered by one of a series of five mass flowmeters. These meters, which had full-scale ranges of zero to 0.0028, 0.028, 0.28, 2.83, and 28.3 scmh (0.1, 1, 10, 100, and 1000 scfh), respectively, were calibrated with gaseous hydrogen. The uncertainty associated with these meters was $\pm 1/2$ percent.

PROCEDURE

In a typical experimental run, the chamber was evacuated to approximately 1×10^{-6} torr. The temperature of the heater was set and controlled near the desired value - either 294 K or 389 K (530° or 700° R). The cryoshroud was then cooled to approximately 22 K (40° R) with liquid hydrogen. The test tank and cold guard were then filled with either liquid hydrogen or liquid nitrogen. The pressures inside the test tank and cold guard were maintained at 11.26 and 11.38 N/cm^2 (16.33 and 16.50 psia), respectively, by the back-pressure control system. The test configuration was maintained at these conditions until the boiloff and all strut and shield temperatures stabilized. Strut and shield temperature stabilization was defined as temperatures which did not vary by more than the error band of the measuring system based on a minimum of three consecutive readings spaced approximately 2 hours apart. The time required to reach a steady-state condition was between 24 and 60 hours depending upon the particular test configuration.

Null or tare tests were also performed in an attempt to determine the magnitude of possible stray heat leaks into the test tank. These tests were conducted with liquid hydrogen in the test tank, cold guard, and cryoshroud and with no electrical energy supplied to the heater. These tests were terminated when a steady boiloff was obtained and all temperatures were between those of the test tank and a cryoshroud.

Subsequent test conditions were obtained by changing the test fluid in the tank and cold guard and/or changing the heater temperature.

METHOD OF ANALYSIS

The solution of the analytic equations results in temperature distributions for both the shields and struts. The analytic heat-transfer rate to the test tank was found from these temperatures. To perform the analysis, the strut, sheets, test tank, and heater were divided into a series of nodes. Each shield ring was taken to be a single node. A heat balance was performed on each node. Generally, only radiation and solid conduction were considered in the heat balances. Gaseous conduction terms were added only in a few analytic cases. Figure 7 is a schematic showing the heat-transfer terms to both strut and sheet nodes. For clarity, only one shield is shown between the heater and the tank. The quantities used in the heat balance for each type of node are considered shortly in the discussion of the nodes.

To calculate the radiation terms to either type of node, Hottel's script \mathcal{F} method, described by Wiebelt in reference 8, was used. The necessary view factors were found either from analytic expressions or numerically by using the computer program described in reference 9. The enclosures needed to use the script \mathcal{F} method corres-

pond to the physical enclosures created by the baffles. The size of storage in the computer limited the number of nodes in any one enclosure to 61. Fortunately, with shields and their baffles present, several enclosures can be defined, so that the total number of nodes can be increased. The enclosures are discussed further in appendix B. When all the radiation and conduction terms were calculated, they became input to the CINDA-3G computer program. This program is a thermal analyzer and is described in reference 10.

STRUTS

The struts were used to attach the heater to the tank. The thermal analysis yielded the temperature distribution along each of the struts. The heat-transfer rate into the test tank by strut conduction was found from the temperature gradient in the strut at the tank end. The analysis yielded a heat balance for each node along the strut. Figure 7 is a schematic showing the sources of energy to a node. Heat entered or left the strut node by conduction and radiation. The conduction heat transfer may be either axial or circumferential. It was assumed that there was no radial gradient in the wall thickness of the strut. On its exterior surface the node absorbed radiant energy which primarily originated on the heater. The spacing between struts was large compared to their diameter. Therefore, the view factor between struts was taken as zero. Thus, the only way radiant energy leaving any of the struts influenced the node under consideration was by reflection off another surface such as the tank.

The purpose of the cryshroud and baffles was to simulate the environment of space. Since the cryoshroud and baffles were cooled by liquid hydrogen, most of the radiant interchange was from the node to the cryoshroud and baffles. The analysis also accounts for radiant interchange on the inside of the strut. The radiation barriers, shown in figure 5(b), were installed inside the struts to prevent direct radiation between the cold and warm ends of the strut. However, they did not prevent cross radiation between the outward and inward halves of the strut. The analysis accounts for such cross radiation.

The fiberglass struts conducted thermal energy poorly. The amount of incident radiant energy was much greater on the inward-facing half of the strut than on the outward-facing half. The inward half saw the heater well, while the outward half had a good view of the cryoshroud. Therefore, there was a good possibility of a thermal gradient around the circumference. Despite the large circumferential strut gradient in some of the tests, it was found that, at most, only two circumferential nodes were needed for each axial location.

Two factors worked to reduce any circumferential strut gradient. Both conduction and internal radiation between the inward- and outward-facing halves of the strut tended to reduce the gradient. Many of the analytic results presented assumed a uniform cir-

cumferential temperature. When this assumption was made for the half-black struts, a separate exterior radiation balance was taken for each half of the node circumference. This procedure was necessary because the simpler analysis using an average circumferential emissivity gave an erroneous prediction.

All surfaces were assumed to be opaque, and the temperatures were determined with the assumption of gray surfaces. For a gray surface the emissivity and absorptivity are equal. (The effect of a nongray tank surface on the heat-transfer rate was also considered.)

In the test configuration the heater and tank were both axisymmetric, with a common axis of revolution. The struts were all parallel to this axis and were located on a common radius.

The baffles and cryoshroud are the surrounding which enclosed the struts, heater, and tank. This "surrounding" was assumed to be at constant temperature and to have uniform surface properties.

SHIELDS IN PRESENCE OF STRUTS

Figure 7 also shows a planar shield schematic with the sources of heat transfer to a shield node. The struts can influence the temperature of the shields in two ways. The surface of the sheet seeing the struts has radiant interchange with them. Also, with the struts connected to the ring, there can be conduction between the struts and the ring. This conduction affects the ring temperature, which in turn influences the sheet temperatures.

From the viewpoint of the struts, the shields radiatively influence the strut temperatures in much the same way as the heater or tank does. A radiation balance for a strut node was made by considering an enclosure containing the surfaces which interact with the strut node by radiation. These surfaces either saw the strut node directly or emitted radiation which was incident on the strut node after it was reflected off another surface. For a strut node between two shields, the enclosure consisted of the surface of a sheet of each shield, along with the surfaces of the baffles, the cryoshroud, and the other struts. The other struts were present in the enclosure because, even though their view factors to the strut in question were assumed to be zero, their emitted energy was reflected off surfaces such as the tank and reached the strut in question. If the strut node was between the heater or tank and a shield, a sheet was replaced by the surface of the heater or tank. When the strut node was between the sheets of a single shield, it was inside the aluminum blocks used to attach the shields and struts. Generally, the strut was assumed to be at the same temperature as the block.

The analysis for the sheet temperatures considered only a radial temperature gradient and assumed uniform circumferential properties. The analysis determined the

temperature of each node on each sheet. The radiation balance depended on the surfaces seen by the sheet. The outside of the sheet node faced the heater, the tank, or another shield. The inside of the same sheet node faced the other sheet of the same shield and the shield ring. The surfaces seen by the inside of the node depended on the radial position of the node. For radial positions less than that of the ring, the enclosure consisted of the inside surface of both sheets as well as the ring. For radial positions greater than the ring, the enclosure consisted of the outward side of the ring, the edge of the baffle, and that portion of the inside surfaces of both sheets at a radial position greater than the ring, as shown in figure 7. The analysis assigned the mass of the two legs of the channel shown in figure 6(b) to the web of the channel. Also, the surface coating of each leg was assigned to the inside surface of the outermost sheet node. This procedure is discussed more fully in appendix B. The enclosure containing the outside surface of the sheet also contained the strut and baffle surfaces and the surfaces of the cryoshroud, in addition to the surfaces of the heater, the tank, or another shield.

Even though there was not absolute circumferential symmetry, we felt that the assumption was still justified. The radiation balance on an outside sheet surface at a point midway between two struts was different than the balance for a point directly in front of a strut. However, since the surface area of all the struts in the enclosure was small compared to that of the sheet, the struts did not strongly influence the sheet temperature by radiation. Also, the relatively large number of 12 evenly spaced struts supported the assumption of circumferential symmetry.

The aluminum blocks used to attach the shields and struts disturbed the symmetry for the enclosure between the sheets of a shield. However, this effect on the sheet temperatures was probably small. The emissivity of the blocks was relatively low but different from that of the ring, and an area-weighted emissivity was used in the analysis.

The starting point for the analysis of the shield temperatures was the assumption that all surfaces were diffusely emitting and reflecting. Experimental results suggested that accounting for directional properties could improve the predictions for the sheet temperatures. The directional property model considers emissivity and reflectivity to be a function of the angle with the surface normal. Unfortunately, the calculation of radiant interchange factors is much more complex when this model is used than for diffuse surfaces. The directional interchange factors were found from a Monte Carlo simulation. And to keep the computer cost from becoming excessive, a simplified model was used. The major simplification in the model is that the sheets are at uniform temperature, and this assumption was supported by the experimental data. The change in each sheet temperature caused by directional properties was found for the simplified model. This change was then applied to the temperatures for each sheet that were calculated for the test configuration by using the diffuse assumption. The analysis

for the test configuration assuming diffuse surfaces is discussed in appendix B. Appendix C contains the analysis for the simplified configuration which used directional properties.

The directionally dependent interchange factors were found between the entire sheet and another surface. This other surface was either the heater, the surrounding, the shield ring, or another sheet. Calculating the interchange factor for the entire sheet resulted in a significant reduction in computer time. In addition to the directional interchange factors, the Monte Carlo simulation was used to determine directionally independent interchange factors for diffusely reflecting whole sheets. These factors incorporated nonuniform radiosity and were for the same simplified geometry and hemispherical emissivity as the directionally dependent interchange factors. The diffuse interchange factors for the test configuration yielded nonuniform radiosity results when many sheet nodes were used.

After the interchange factors were found, the following thermal analyses were made: (1) a directionally dependent analysis, which yielded a temperature for each sheet of each shield; (2) a directionally independent analysis for diffusely reflecting uniform-temperature sheets, performed for the same simplified configuration as the first analysis and using Monte Carlo-determined whole-sheet interchange factors; (3) the thermal analysis for the test configuration based on the equations given in appendix B. This last analysis gave strut and shield ring temperatures, as well as sheet temperatures. It is based on experimental surface properties and includes several nodes on each surface, with each sheet having 12 nodes.

The temperatures for each sheet from the third analysis were corrected to account for directional properties by applying a temperature ratio. This ratio was the sheet temperature found in the first analysis divided by the temperature found in the second analysis.

The analysis presented in appendix C for the directional interchange factors was based on electromagnetic theory. The surface properties were determined from the extinction coefficient and index of refraction and are a function of the angle with the surface normal. The emissivity was relatively large at high angles to the normal. The measured values for the extinction coefficient and index of refraction are given in reference 11 for aluminum at a wavelength of 12 micrometers. The equation for the directional emissivity can be integrated to obtain the hemispherical emissivity. This hemispherical emissivity at a wavelength corresponding to room temperature was only about 25 percent less than the average measured emittance for the sheet material.

RING BETWEEN SHEETS OF A SHIELD

The analysis for the shield ring depended largely on the analysis for the sheets and struts. The radiant energy absorbed on both the inside and outside surfaces of the ring was found as part of the sheet analysis. The mathematical enclosure used to determine the script \mathcal{F} values encompassed two physical enclosures. The first enclosure contained the inner portions of both sheets and the inside surface of the ring. The other enclosure was much smaller and was the annular space between the shield ring and the baffle edge.

ANALYTIC MODEL

The independent variables of the analytic model used for the comparisons with the experimental results are given in table I. This table lists the dimensions used, along with the emissivities and thermal conductivities. The radius of the shield ring was chosen to be the same as the radius of the strut circle. The actual ring lay outside this radius. However, the strut attachment blocks were on both sides of this radius. Using the strut circle radius seemed to be a reasonable approximation for the ring-block combination. Also, the web thickness of the shield ring was neglected in the steady-state analysis. The radius of the shield was used to calculate the baffle area even though there was some clearance between the outer edge of the shields and the inner edge of the baffles in the actual test configuration. This was done because the outer portion of the sheets and ring saw either the baffle or the cryoshroud, which had the same surface coating and temperature as the baffle.

The centerline spacing dimensions in table I are for the two shield spacings used in the testing. The spacing between shields was measured between the top sheet of the lower shield and the bottom sheet of the upper shield. This spacing was held constant for every test. Both the fiberglass and the titanium struts had the same thickness. The length of the strut was slightly greater than the sum of the minor tank radius and the overall spacing. The reason for this was that the struts were attached to the aluminum tank band at a point part way up on the cylindrical portion of the test tank.

The thermal conductivity shown in table I for fiberglass was reported in reference 7 and that for titanium in reference 12. The conductivity of the sheet was a composite of those for aluminum and Mylar. References 13 and 14 give the conductivity for each of these materials. The conductivity of aluminum is sufficiently high that most of the radial conduction in the sheet is through the aluminum.

Even though attempts were made to achieve the same heater temperature in each test, this was not achieved. Since the heat-transfer rates are dependent on the temperature to the fourth power, each test comparison was made for the actual heater setting for the test. The pressure inside the test tank was controlled very accurately.

Therefore, there was little variation in the tank temperature. The temperature in the cryoshroud varied between 22 and 39 K (40° and 70° R), with an average value of 28 K (50° R). This variation in shroud and baffle temperature did not significantly affect the analytic results, except for heat transfer by gaseous conduction.

The bottom area of the tank as shown in figure 3 is the surface area which could absorb energy from the heater. However, the total area of the tank was used to determine the emissive power of the tank. This area consisted of the surface area of the bottom, top, and sides, as well as the area of the piping between the top of the tank and the bottom of the cold guard. The effective total area of the cryoshroud included the surface area of both an imaginary baffle at the tank near the strut attachment ring and a real baffle at the heater. Also included was the wall of the cryoshroud between them. The imaginary baffle was used to simplify the analysis. The actual shroud can be seen in figure 3(b) to extend around the entire tank. However, in calculating the radiant interchange with the heater, the imaginary baffle was placed near the tank, and that portion of the shroud not between it and the heater baffle was ignored.

Table I shows that the emissivity of the sheet material was assumed to vary linearly with temperature. The room-temperature emissivity of the sheet material was measured with a Gier Dunkle emissometer and had an average value of 0.03. Calculations showed that the coating thickness was sufficient so that bulk properties would apply in making emissivity predictions as a function of temperature. Reference 15 shows that the electrical resistivity of aluminum is nearly linear with temperature to as low as about 76 K (137° R). This indicates a linear temperature dependency for emissivity.

Although the emissivity of the aluminized surfaces was assumed to vary linearly with temperature, in actuality it probably does not. Experimental work given in reference 16 has yielded results that show a temperature dependency which is between linear and a constant value. The effect of these two assumptions on the shield temperatures is shown in figure 8. The heater temperature was 389 K (700° R), and even though the coldest sheet temperatures were only about one-third of this value, the effect on the shield profiles was relatively small.

When the emissivity of the shields was measured, there was a relatively large percentage of uncertainty in the value. Figure 9 shows the variation in shield temperatures caused by a variation in emissivity. This variation of ± 0.005 is the same as the uncertainty in the measured emissivity, which was ± 15 percent. These curves are for an emissivity independent of temperature. This figure shows that this emissivity results in a significant change in the sheet temperatures for the colder shield.

The room-temperature emissivity of the inside of the shield ring was taken as an area-weighted average of the measured emissivity of the blocks (0.15) and the ring itself (0.03). A linear temperature dependence was also assumed for this emissivity.

The emissivity of the painted surface was assumed to be the same as that used in previous shadow shield tests reported in reference 4.

RESULTS AND DISCUSSION

This section of the report presents all the experimental results and their accompanying analytic predictions. Table II gives a description of each test. The tests were numbered according to the order in which they were run. The primary purpose of each test is mentioned along with the strut and shield configurations. The pressure given is that measured inside the shroud. It is significant in determining the contribution of gaseous conduction to the overall heat-transfer rate. The effects of gaseous conduction are considered in the latter part of this section.

The tests conducted without shields between the heater and the tank are discussed first. Comparisons are made that show the effects of insulating the struts. Also, the relative profiles for the half-black and all-black struts are examined. Then the heat-transfer rates in these tests are discussed.

Following the no-shield comparisons, the experimental and analytic comparisons for tests with shields are presented. The presence of shadow shields greatly reduced the heat-transfer rate to the test tank for two reasons: first, they greatly reduced the amount of radiant energy absorbed by the tank; second, the strut temperature profile was altered significantly in the presence of shields. With the altered strut profile the conduction heat-transfer rate was greatly reduced. Both the shield and strut temperature profiles are discussed, along with the associated heat-transfer rates.

In the figures which follow, the analysis is based on the information in table I unless otherwise noted. Also, the figures often contain more than one analytic curve. Generally, when this occurs the solid curve is to be compared with the experimental data, while the dashed curve shows the analytic effect of a change in some variable.

TESTS WITHOUT SHIELDS

Two series of tests were conducted without shields. In the first series, liquid nitrogen was used in the test tank. In the second series, liquid hydrogen was used. For both series, 12 struts were used, half of which were fiberglass and half titanium. Because of a limitation on the number of thermocouples which could be monitored, not all the struts were instrumented. For each material, one insulated and one all-black strut were installed and thermocoupled. The remaining struts were half black, with three of the fiberglass and two of the titanium struts being instrumented. Table III

presents an overview of the strut temperatures. The entries in the table often are the result of averaging readings. Because there was good agreement in the thermocouple readings for struts of the same type, we felt that it was appropriate to average the readings. Additionally, when there were thermocouples at the same location for the same type of strut but they were on the inward and outward sides of the strut, they too were averaged. The temperature difference between the inward and outward sides is discussed when the experimental and analytic results are compared for each of the configurations.

There are two parts to table III. Table III(a) gives the temperature ratios for the thermocouples on the body of both the insulated and uninsulated struts. The values in the table were normalized in a linear conduction manner. The entries in table III(b) are for the thermocouples on the outside layer of the insulated struts. Since their values were primarily determined by radiation, these temperatures were normalized by being divided by the heater temperature.

Insulated Struts

The insulated struts have been described previously, and a view of their construction is given in figure 5(c). Figure 10 compares the experimental and analytic temperature profiles for insulated fiberglass and titanium struts obtained with a room-temperature heater and liquid hydrogen in the test tank. Figure 10(a) gives the comparison for the fiberglass strut, while figure 10(b) gives the comparison for the titanium strut. In each part of the figure there are two analytic profiles. One profile is the strut temperature profile and should be compared with the temperatures of the thermocouples on the body of the strut. The other profile is for the outward side of the outer layer of insulation and should be compared with the readings for the outer layer. In determining the analytic temperature profiles, heat transfer by radial conduction through the insulation was considered, along with axial and circumferential conduction between nodes on the insulation. All the nodes on the insulation received radiant energy from the heater. For both the fiberglass and titanium struts, there was good agreement between the analytic and experimental strut profiles. For both struts the outer insulation profiles were about the same. The agreement in the outer layer profiles was good at the warm end and relatively poor at the cold end. The temperatures for the outer layer were strongly influenced by the radiation environment.

The next figure shows the effect of varying the insulation radial thermal conductivity for the fiberglass and titanium struts. Figure 11 is similar to figure 10 except that the heater temperature has been increased from room temperature to the high-temperature value. Figure 11 gives curves for three values of the insulation conductance multiplier.

The nominal values for the thermal conductivity both in the radial direction and for the outer layer are given in table I. The value of thermal conductivity in the table is representative of that obtained when insulation was installed on a cryogenic test tank. A multiplier of 1 for the value in the table was used to determine the curves in figure 10. A multiplier of 0 corresponds to no heat transfer between the strut and the outer layer. The curve for a conductance multiplier of 0.2 indicates that the insulation conductivity may have been lower than expected. The insulation was carefully applied to the struts. However, it is reasonable to expect that the conductivity of the insulation would be different from that applied to a tank. The effect of insulation conductance was much less for the titanium strut than for the fiberglass strut. Although it is not shown in either part of figure 11, a conductance multiplier of 2 yielded almost the same results as a multiplier of 1.

Figures 12 and 13 contain the same type of data as figures 10 and 11, respectively, except that nitrogen was used in the test tank in place of hydrogen. Substitution of nitrogen into the test tank yielded about the same agreement between the experimental and analytic temperatures as was obtained with hydrogen.

By inspection of parts (b) of figures 10 to 13, the following inferences can be made: The analytic prediction for the outer layer probably used an insulation conductivity which was too large. Also, in each figure, except figure 12, the analytic profile overpredicted the strut temperature at the warm end, indicating the possibility of a significant thermal block at this end.

Half-Black and All-Black Struts

The half-black and all-black struts had temperature profiles markedly different than those of the insulated struts. This result is shown in the next series of nine figures (figs. 14 to 22). The first four figures are for titanium struts with each heater setting and test tank fluid. The next figure compares the effect of the strut end fitting on the temperature profile. The last four figures are for fiberglass struts with the same boundary conditions. In each of the eight figures there are two parts. Parts (a) give the temperature profiles for the half-black struts, while parts (b) give them for the all-black strut.

Titanium with hydrogen. - The experimental and analytic comparisons for the titanium struts with hydrogen in the test tank are shown in figure 14 for the room-temperature heater and in figure 15 for the high-temperature heater. In general, there was good agreement between the analysis and test data. Comparing parts (a) and (b) of each figure shows that the strut coating used strongly influenced the temperature profile. The all-black strut was considerably warmer than the half-black strut along

almost its entire length. And the analytic gradient at the tank end was significantly steeper than that for the half-black strut.

The analysis yielded only a very small circumferential gradient at the warm end of the half-black strut and no gradient at the cold end. Experimentally, there was evidence of a circumferential gradient throughout most of the length of the strut. However, it was relatively small. On both parts of each figure there are two types of analytic profiles. The first one is for a single-node analysis and assumes no circumferential gradient in the strut. The second is for a two-node analysis with one temperature prediction for the inward side of the strut and another for the outward side of the strut. For the half-black struts the analytic profiles for the outward side and single node are coincident. This is not true for the all-black strut, however. The inward-side profile and the outward-side profile are about equidistant from the single-node profile. Since the thermocouples were only on the outward side of the all-black strut, the experimental data should be compared with the coldest profile in part (b) of each figure.

Comparison of figures 14 and 15 shows about the same agreement between the analysis and the experimental data. This is significant in that while there was a difference of only 30 percent in the heater setting, there was a difference of nearly 200 percent in the amount of radiant energy absorbed along the length of the strut. Thermocouples on the tank support ring showed it to be running 22 K (40° R) warmer than the tank surface for the high heater setting. Figure 15(a) also shows the effect of imposing this warm tank boundary condition on the analytic strut temperature profile. Somewhat surprisingly, this effect was small and did not account for the analysis underpredicting the cold-end temperature profile. The underprediction could be caused by contact resistance at the tank end of the strut, as is discussed subsequently.

Titanium with nitrogen. - Figures 16 and 17 give the temperature profiles for titanium struts under the same conditions as figures 14 and 15 except that nitrogen replaces hydrogen in the test tank. Because the circumferential gradient was so small for the half-black struts, only the one-node temperature profile is shown. This is not the case for the all-black strut. The one-node profile is shown for this strut to give the average strut profile, and the two-node profiles are shown to compare the outward-side profile with the experimental data. With nitrogen in the tank the agreement was about as good as with hydrogen in the tank. Naturally, the cold-end gradient was less with nitrogen in the tank.

An additional profile is shown in each part of figure 15. This is a one-node profile with no radiation from the heater or tank. The strut exchanged radiant energy only with the cryoshroud. These profiles differ markedly from the experimental profiles. They are shown to give an indication of the strut gradients which could be achieved if heater radiation could be isolated from the struts such as by shadow shields. These isolated profiles show a negative heat-transfer rate to the tank, while the test profiles show positive heat-transfer rates. Interestingly, the isolated all-black strut has a more

negative gradient than the isolated half-black strut. This result is in contrast to the test profiles, where the all-black strut has a more positive gradient than the half-black strut.

As mentioned previously, the insulated titanium strut data indicate a possible thermal block at the warm end of the strut. Figure 17(a) shows the effect of the thermal block on the temperature profile of the half-black titanium strut. The thermal block was simulated by reducing the boundary temperature of the warm end of the strut 23 K (42° R). The resulting change in the strut temperature profile was very small.

Effect of strut end plug. - Figure 5(b) shows a plug at one end of each strut. This plug was used to attach the strut to the support ring adjacent to the tank. It was expected that the plug would tend to thermally short the strut at the tank end. However, the data did not support this intention, and the analysis generally neglects the effect of the plug and assumes that the end of the strut is at the tank temperature. Only after the short due to the plug was assumed to be in series with a contact resistance between the support ring and the bolt used to attach the strut to the ring was there a significant improvement in the strut temperature predictions at the cold end. Figure 18 shows temperature profiles for the cold end of the strut when contact resistance and the plug were included. The effect is shown for the single-node profile of the half-black fiberglass and titanium struts, as well as for the outward-side profile of the all-black fiberglass strut.

The contact resistance is subject to a high degree of uncertainty, and the value used for the sketch was determined from the best fit of the titanium strut data obtained with a room-temperature heater. Analytic profiles were determined, including a range of resistances for the half-black, all-black, and insulated struts obtained with both tank temperatures. Fortunately, a normalized conductance of 0.2 yielded good agreement for all six cases. The normalized conductance is the heat-transfer coefficient multiplied by the radius of the contact surface and divided by the thermal conductivity of the bolt. Figure 18(a) shows that the two resistances in series account for the analysis underpredicting the cold-end temperatures for the titanium strut. Figures 18(b) and (c) show the effect of applying this same contact resistance and plug short for half-black and all-black fiberglass struts. (The overall comparisons for all the fiberglass strut data are discussed subsequently.) Including the contact resistance and the plug for the half-black fiberglass strut caused the analysis to somewhat underpredict the experimental data. The all-black strut had fewer thermocouples and only one near the tank. The standard analysis overpredicted the temperature at this location, while including the resistances resulted in good agreement.

Fiberglass with hydrogen. - Figures 19 and 20 give the experimental and analytic comparisons for the half-black and all-black fiberglass struts with hydrogen in the test tank. Figures 19(a) and 20(a) show that the analytic circumferential gradient was small

even though it persisted almost to the tank end of the strut. Generally, there was good agreement between the analysis and the thermocouples on the outward side of the strut. The indicated experimental circumferential gradient was larger than the analytic gradient.

Figure 19(b) shows the necessity of including cross radiation in the analysis. The circumferential gradient was about doubled when cross radiation was neglected. Also, figures 19(b) and 20(b) show that the agreement between the outward-side profile and the experimental data was good when cross radiation was included. Close inspection of the single-node profiles in figures 19(b) and 20(b) shows that the cold-end temperature gradient was nearly proportional to the heater temperature.

Fiberglass with nitrogen. - Figures 21 and 22 give the analytic and experimental temperature profiles for the same conditions as figures 19 and 20 except that nitrogen replaces hydrogen in the test tank. The agreement between the analysis and the experimental data was about the same as with hydrogen in the tank. Figure 21(a) shows that a very large change in the assumed thermal conductivity of the half-black fiberglass strut resulted in a very small change in the strut temperature profile. However, since the heat-transfer rate of the struts was proportional to the conductivity, the heat-transfer rate would change significantly.

Figures 21(a) and (b) show the analytic profiles for the fiberglass strut when there was no radiation from the heater or tank. The change from the test profiles was more pronounced for the fiberglass struts shown here than for the titanium struts shown in figures 16(a) and (b).

Comparing figures 19 and 22 shows the extent to which radiant heat transfer dominated the fiberglass strut temperature profiles. Over the middle 80 percent of the length of the half-black strut, the normalized analytic temperatures were within 10 percent for either heater temperature. The normalized temperatures are the strut temperatures shown in the figures divided by the heater temperatures. The analytic effect of thermal conductivity on the temperatures of the all-black strut was small. This can be seen by comparing the two curves in figures 19(b) and 22(b) for which cross radiation was neglected. In figure 22(b), when cross radiation was neglected, so was strut conduction for both the inward-side and outward-side profiles. In figure 19(b), strut conduction was retained. The shapes of the corresponding curves in each figure are similar and the normalized temperatures are very close. Only at the ends of the strut are the effects of strut conductivity really noticeable. The test tank acted as a shadower to prevent radiant energy from the heater being absorbed by the strut in the vicinity of the tank. Shadowing was neglected in the analytic predictions. However, conservative estimates of shadowing showed it to have a very small effect even for fiberglass struts.

Part (b) of figures 19 to 22 show a significant overprediction of the strut profiles at the cold end. Figure 18(c) shows that the combination of contact resistance and cold-

end short could account for this overprediction.

In addition to the standard analysis, figures 16 and 21 show strut temperature profiles assuming no radiation from the heater or tank. The change in the tank-end gradient in going from the standard profile to the no-radiation profile was very large. Consequently, the decision to insulate the struts in a space vehicle, from a thermal management standpoint, would be strongly influenced by the emissivity of the payload surface. In an actual vehicle the emissivity of the payload would probably be less than that of the near-black surface used in the tests. Additional analysis showed that reducing the emissivity to 0.3 resulted in a gradient change about half as great as that between the curves shown in figures 16 and 21. Further reducing the emissivity to 0.1 resulted in a change from the standard analysis of over 70 percent as much as going to a nonradiating heater. It is shown in the discussion of the shield test data that, when shields are present, even for a nearly black heater the gradients at the tank end of the strut approach those for a nonradiating heater.

Heat-Transfer Results

Experimental and analytic heat-transfer rates into the test tank are compared in table IV. Results are given for the four different boundary conditions used in the testing. Only the total experimental heat-transfer rate was actually measured. The conductive heat-transfer rates neglect both contact resistance and the thermal short. The values given for the experimental conductive heat-transfer rate are semiempirical. The experimental strut gradient at the cold-end tank boundary was found by taking the temperature difference between the tank and the thermocouples located 3.8 centimeters (1.5 in.) from the tank ring. The average thermocouple reading was used for each strut configuration at this location. This gradient was then used along with the analytic thermal conductivity to determine the experimental conduction heat-transfer rate. The degree of agreement between the analytic and experimental conduction heat-transfer rates could be deceptive. Any difference between the actual experimental conductivity or thickness and the assumed analytic conductivity and thickness was not accounted for in the results shown in table IV. Even though only half of the struts were titanium, they accounted for about 90 percent of the conduction heat-transfer rate. Also, the analytic heat-transfer rate for an all-black titanium strut was over twice that of a half-black strut. The analytic or experimental strut conduction heat-transfer rates do not include the effect of contact resistance and end plug. Interestingly, the heat-transfer rate decreased by less than 10 percent when these effects were included for the analytic results.

The experimental radiant heat-transfer rate was found by subtracting the conduction heat-transfer rate from the total heat-transfer rate. This radiant heat transfer was the major source of heat to the tank. Two different analytic predictions are given in table IV for the radiant heat-transfer rate. They are designated as the gray and nongray predictions. The gray analysis is discussed in appendix B. This analysis assumed that the emissivity and absorptivity were equal for each surface. The nongray analysis assumed that the absorptivity of the test tank for the end facing the heater was equal to the absorptivity of the tank surface if it were at the heater temperature. Also, the emissivity of the tank was determined by the tank temperature. The rationale behind this assumption was that the incident energy on the tank had the frequency distribution corresponding to the heater temperature.

With one exception the gray analysis badly underpredicted the radiant heat-transfer rate, while the nongray analysis was in good agreement with the experimental data. (No explanation has been found for the anomalous result with the room-temperature heater and nitrogen in the tank.) Almost one-third of the nongray heat-transfer rate and almost all the gray heat-transfer rate occurred in an unanticipated fashion. The ring used to attach the struts to the tank stood off from the tank by 0.63 centimeter (0.25 in.). This is shown in the schematic of figure 7. After a depth several times the annular width, this annular cavity was blocked when the ring was attached to the tank. This arrangement resulted in a highly absorbent annulus which transmitted radiant energy to the tank. It is surprising that the heat-transfer rate to the annulus was one-third of the total nongray heat-transfer rate since the width of the annulus was only about 1 percent of the radius of the tank.

Since the nongray assumption had a significant effect on the heat-transfer rate, the question arose as to whether this assumption would affect the strut temperatures. The percentage variation was relatively small for the absorptivity of the painted surfaces between the heater temperature and hydrogen temperature. However, it was large for the aluminized surfaces. A nongray analysis for the half-black struts yielded no significant change in the strut temperatures from the gray analysis.

The heat-transfer rate to the test tank was strongly influenced by the tank absorptivity and the heater temperature. Even with the nongray analysis the absorptivity of the tank was not known precisely. With a room-temperature heater the absorptivity was the measured tank emissivity. In a previous discussion the uncertainty in the measurement for low-emissivity surfaces was given as about 15 percent.

The temperature across the surface of the heater varied by about 2 percent during a test. Because the heat-transfer rate was dependent on the heater temperature to the fourth power, a 2 percent variation in heater temperature resulted in about an 8 percent variation in the radiant heat transfer to the test tank.

TESTS WITH SHIELDS

With the shields placed between the heater and tank as shown in figure 3, the heater did not view the tank. The highly reflective shields caused much of the energy emitted by the heater to be reflected to the highly absorbing cryoshroud instead of being incident on the tank. Because of the high reflectivity of the shields this process was very efficient in that the radiant heat-transfer rate to the test tank was reduced to less than 1 percent of its no-shield value. The shields also reduced the radiant energy incident on the struts. The struts, instead of viewing the high-emissivity heater for their entire length, saw the low-emissivity shield surfaces for most of their length. Also, the shields were colder than the heater, further reducing the incident radiant energy on the struts.

Table V gives the linearly normalized strut temperatures for the tests with shields. In every test there was at least one half-black fiberglass strut. Only in tests 6a to 6d were the remaining 11 struts fiberglass. In all the other tests the 11 struts were titanium. Of the tests with titanium struts, test series 2 and 3 had evenly spaced shields where the spacing between the heater and the warmest sheet was the same as that between the shields. Series 4 and 5 had closely spaced shields where the warmest sheet was close to the heater with the spacing between shields remaining the same. The data presented in this table were obtained in the same way as the data in table III.

For each strut configuration table V shows that the normalized temperatures were in reasonably good agreement between tests when the tank temperature and shield spacing were the same. This indicates that the strut temperatures were nearly linear with respect to the heater temperature. The actual analytic and experimental strut and shield temperatures are compared in the discussions of the individual tests.

Table VI gives the average normalized shield sheet and shield ring temperatures for each of the tests. For each side of a sheet that was thermocoupled, there were generally two thermocouples at different circumferential locations for each radial location. The analysis assumed circumferential symmetry, and the results in this table are the average at the two circumferential positions. The entries in this table indicate that the radial gradient across each sheet was relatively small. The tank temperature for each test can be found from table V, and table VI shows that the normalized sheet temperatures were nearly independent of the tank temperature. Also there was good agreement in the normalized sheet temperatures for tests with the same shield spacings but different heater temperatures. This result shows that the sheet temperatures were nearly proportional to the heater temperature.

The temperature of the warm shield ring was strongly influenced by the shield spacing. However, this was not as obvious for the cold shield ring. Somewhat surprisingly, the shield ring temperatures did not appear to be strongly influenced by the strut material.

A large fraction of the sheet temperature entries in table VI are indicated to be corrected values. This correction was made to account for the higher emissivity of the tape used to cover the sheet thermocouples. Initially, all the thermocouples were covered with aluminized tape to minimize errors in the thermocouple readings. These errors would occur if the emissivity at the thermocouple were different from the local emissivity of the sheet. Even though the tape had a low room-temperature emissivity of about 0.06, it was twice that of the basic sheet material. This difference in emissivity resulted in significant errors in the thermocouple readings. The magnitude of this error is shown in table VII. Here the ratio of corrected temperature to uncorrected temperature is given for each side of each sheet thermocoupled. The uncorrected temperature is the standard analytic temperature. The analytic corrected temperature was found by doubling the emissivity of a single radial node for the surface under consideration. The ratio of corrected to uncorrected temperatures was then applied to the experimental readings to obtain the corrected experimental readings shown in table VI. The local variation was found by doubling the emissivity of the surface of only a single node of the sheet. Fortunately, the resulting temperature corrections were not a function of radial position, heater temperature, or shield spacing.

In this section of the report the shield and strut temperatures for the tests with shields are compared. Following this, the heat-transfer rates for each of the tests are discussed. All the shield tests are grouped into three categories: (1) 12 fiberglass struts with evenly spaced shields, (2) 11 titanium struts and 1 fiberglass strut with evenly spaced shields, and (3) 11 titanium struts and 1 fiberglass strut with closely spaced shields. The analysis and experimental data are compared for the tests in each category. The form for the presentation of the data is the same for each group of tests. The sheet and shield ring temperatures are analyzed. Then the strut temperatures are compared. The heat-transfer rates to the test tank with shields present were often strongly influenced by gaseous conduction inside the shroud. The effects of gaseous conduction on the heat-transfer rates and shield temperatures are discussed in the section Heat transfer by gaseous conduction.

Shield and Strut Temperatures

The tests with shields was conducted primarily to study the thermal interactions between struts and shields. No insulated struts were tested with shields. When there were 12 fiberglass struts, 3 of them had an all-black coating, while the remaining 9 had a half-black coating. When there were 11 titanium struts, 1 had an all-black coating. The other 10 titanium struts and the single fiberglass strut had a half-black coating.

Tests were made for two different shield spacings. The spacing information is given

in table I. For evenly spaced shields the distances between the heater and the warmest sheet, between the shields, and between the coldest sheet and the tank at its centerline were each approximately 9.2 centimeters (3.6 in.). These three distances plus the thicknesses of both shields gave an overall centerline spacing of 31.8 centimeters (12.5 in.). For the tests with closely spaced shields the overall spacing between the heater and the tank remained the same. However, the warmer shield was moved to a distance of 1.3 centimeters (0.5 in.) from the heater, while the distance between shields remained as it was.

Twelve fiberglass struts, evenly spaced shields. - The tests with 12 fiberglass struts (tests 6a to 6d) were conducted with both heater settings and both fluids in the test tank. Because fiberglass has a much lower thermal conductivity than titanium, the analysis predicted lower heat-transfer rates to the hydrogen-filled test tank with fiberglass struts than with titanium struts.

Shields: Figures 23 and 24 give the sheet and shield ring temperatures for all four boundary conditions. The sheet temperature profiles shown in figure 23 are very similar to those encountered throughout the entire series of tests. Figure 23 shows data for the high heater settings; part (a) is for liquid hydrogen in the test tank, while part (b) is for liquid nitrogen. Comparing figures 23(a) and (b) shows that, in these tests, the fluid in the tank had a negligible effect on the sheet temperatures. The radial gradient for each sheet was very slight. There was also no circumferential gradient. This is not too obvious from the data, though it is indicated somewhat in figure 23(b). At each radial position other than the center there were two thermocouples spaced approximately 180° apart on the sheet surface. These two readings were often so close that they appear as a single symbol in the figures. Both the warmest and coldest sheet had thermocouples on each surface of the sheet. The corrected temperatures show no gradient across the thickness of either sheet.

The data in figure 23(a) show good agreement between the analysis and the experimental data for each sheet, except the cold sheet of the warm shield. The causes for this discrepancy remain a mystery. This same phenomena appears in the data presented in reference 4. Figure 23(b) shows the temperature profiles when the directional effects were neglected. The assumption of directional properties chiefly affected the sheets of the cold shield and did not improve the correlation for the cold sheet of the warm shield. One of the arguments that complicates acceptance of the directional model is that adjusting the analytic temperatures for the cold sheet of the warm shield to the experimental values resulted in good agreement for temperatures of both sheets of the cold shield when directional effects were neglected. However, the directional model was retained since the thermocouples may give only a local temperature which is not the same as that of the sheet itself. (The section Thermocouple covering discussed the effect of thermocouple covering on the recorded temperatures.) The issue is further clouded

by the data presented in figure 9. These data show that, for the experimental uncertainty in the room-temperature shield emissivity, there was a significant uncertainty in the sheet temperatures for the colder shield at either heater setting. This uncertainty prevented assigning the correct analytic model on the basis of the cold-shield sheet temperatures. Not only were the experimental and analytic temperatures noticeably different for the cold sheet of the warm shield, but also the radiant heat transfer to this sheet could be greatly in error since it is proportional to the sheet temperature to the fourth power. If the experimental readings were taken to be the true sheet temperatures, the heat absorbed by the sheet was only about 60 percent of the predicted value.

Figure 24 gives the sheet and ring temperature profiles with the room-temperature heater setting and both fluids in the test tank. The experimental temperatures for the coldest sheet were significantly lower with hydrogen in the tank than with nitrogen in the tank. This temperature difference was probably caused by the higher pressure inside the shroud with hydrogen in the tank than with nitrogen. The coldest sheet temperatures were the ones which responded most rapidly to pressure changes. The effect of the pressure inside the shroud on the sheet temperatures is considered further in the section Heat transfer by gaseous conduction.

Figure 24(a) shows the analytic effect of shield conductivity on the temperature profiles. The shields were virtually nonconducting. However, shield conductivity did have a noticeable effect on the warm-shield ring temperature. In the standard analysis the outermost sheet nodes were at the same temperature as the corresponding shield ring. Figure 24(b) shows the effect of changing this assumption by thermally disconnecting the outermost nodes from the shield rings. (The emissivity of the surfaces of the outermost nodes was maintained consistent with the standard analytic model.) Since figure 24(a) shows the sheets to be nearly nonconducting, the effect of this change was confined to the area close to the ring. The purpose of the auxiliary curves is to show the effects of disconnecting the sheets from the rings. A high emissivity was maintained on the inward side of the outermost node for each sheet. This high emissivity resulted in sheet temperatures at the edge that were lower than that of the ring. Had the low sheet emissivity been used for the inward side of the outermost node, the temperature drop for the edge of the sheet would have been less. Although it is not shown on the figure, the ring temperatures decreased only slightly when the disconnected assumption was used.

Also shown in figure 24(b) are four horizontal lines denoting uniform-temperature sheet profiles. These profiles are for infinitely conducting sheets and are shown for illustrative purposes only, since the test sheets had low thermal conductivity. The temperature of the warmest sheet was much lower for the uniform-temperature sheet than in the standard analysis. With infinite conductivity the sheets could transfer energy

to the outer edge, where it was dissipated to the surroundings. This heat transfer was further improved by the inward side of the outermost node having a high emissivity. Since the sheets were infinitely conducting, they were assumed to be disconnected from the rings. Otherwise, the whole shield would be at a single temperature. As it is, the temperature difference between sheets for each shield was relatively small.

The square symbols in figures 23 and 24 give the experimental temperatures for the shield rings. The short horizontal line connected to the sheet profiles is the analytic prediction for the ring temperature for each shield. A horizontal line was used because the ring, being massive, had no thermal gradient. For the high-temperature heater data shown in figure 23 the agreement was good. For the room-temperature data shown in figure 24 the agreement was poorer. The agreement would be even worse if the effect of the instrumentation tabs was neglected. Parts (b) of figures 23 and 24 give the ring temperature for the cold shield, neglecting the effects of the tabs. The warm-shield ring temperature was not affected by the instrumentation tabs.

Basically, these tabs radiated to the cryoshroud and absorbed energy from the warmer sheet. The surface area of the side of the tabs facing the cryoshroud was only about 10 percent of the painted ring surface. The other side of the tabs absorbed energy from the warmer sheet and exchanged energy primarily with both sheets. The tabs were nearly isothermal with the shield ring to which they were bolted. The tabs did not noticeably affect the temperature of the warm-shield ring because the temperature ratio between the cold sheet of the warm shield and the ring of this shield was less than 1.5. Consequently, the heat-transfer rate from the sheet to the tabs was not great. However, the temperature ratio between the cold sheet of the warm shield and the tabs on the cold shield was about 2.5, resulting in a higher heat-transfer rate. Even though the area on each side of the tabs was only about 5 percent of the outer sheet node area, the tabs had a high absorptivity, resulting in more than doubling the heat absorbed by the outermost node of the warm sheet of the cold shield. When titanium struts were used, conduction between the struts and the rings was sufficient to mask out the effect of the tabs.

Struts: Figures 25 to 28 give the comparisons between the analytic and experimental strut temperatures for each of the heater settings and tank fluids. There are three parts to each figure. Part (a) is for the half-black struts with radiation barriers. Part (b) gives the temperature profiles for the single half-black strut with the radiation barriers removed. Part (c) gives the temperature profiles for the all-black struts. On these figures the tests are designated as being for evenly spaced shields, while their location relative to the strut distance is much closer to the heater. This is a result of the even spacing designation referring to the distance between the heater and tank along the configuration centerline while the struts are attached to the perimeter of the test tank.

Because the struts were relatively cold for a considerable portion of their length, it was expected that removing the internal radiation barriers would not have a significant effect on their temperature profiles. This can be seen experimentally by comparing the data in part (b) of each figure with that in part (a) of the same figure. This is also shown by the analytic curves in part (b) of each figure. In addition to the standard analytic curve, which assumed no axial internal radiation, there is a temperature profile assuming axial radiation through the strut with a black interior. In each figure there is a small noticeable difference between the two analytic curves. These curves have the same relative shape in each figure, not being strongly influenced by heater setting or test tank fluid. Even though the effect of the radiation barriers on the profiles was small for the relatively slender struts tested, they did block heat transfer from the strut to the test tank and thereby removed a source of uncertainty in the heat-transfer rate.

The analysis shown in each of the four figures underpredicted the strut temperature profile at the cold end for both the half-black and all-black struts. The agreement was better at the warm end of the strut. Part of the disagreement resulted from the analysis underpredicting the ring temperature for the cold shield, especially with the room-temperature heater. It is shown for the worst of the four cases in figure 28. In addition to the predicted temperature profiles, the strut profiles for the half-black and all-black struts are given, assuming the ring temperatures were the experimental values. Using the analytic ring temperatures resulted in good agreement over only the warmest third of the strut length. However, using the experimental temperatures resulted in nearly two-thirds of the strut profile being in good agreement with the experimental data.

For each of the four boundary conditions, there was experimental evidence of a circumferential gradient only near the heater. This tentative evidence was the same for both the all-black and half-black struts. Figure 25(c) shows an appreciable analytic circumferential gradient near the heater of the all-black strut. Calculations showed no analytic circumferential gradient for the half-black strut.

Figures 26(a) and (c) show the effect of varying the thermal conductivity of the strut material on the temperature profile. The perturbed thermal conductivity is a constant and was found by evaluating the polynomial in table I at the mean temperature between the heater and the tank. The mean temperature was close to that of the warm-shield ring, so that near the test tank the conductivity was perturbed significantly. This perturbation noticeably changed the strut profile but did not account for the disparity between the analytic and experimental profiles.

Figures 27(a) and (c) show the effect of varying the temperature of the cryoshroud from the value given in table I. These data are for the room-temperature heater and hydrogen in the test tank. The perturbation of increasing the shroud temperature by

40 percent was based on the maximum shroud temperature recorded during the tests. Typically, a few cryoshroud sensors read this high, while the others were lower. This increase in the shroud temperature did affect the cold-end temperature of the struts. Using the higher shroud temperature and recognizing that the analysis underpredicted the cold ring temperature accounted for most of the difference between the analytic and experimental profiles with hydrogen in the tank. However, since the effect of a warmer shroud was confined to strut temperatures less than 60 K (108° R), the agreement with nitrogen in the test tank would not be improved.

Figures 28(a) and (c) examine the effect of assuming that the end fitting at the tank ring caused a thermal short in the strut. The effect of the short dissipated rather quickly along the strut from the tank ring. Because of this rapid dissipation the thermocouples only suggested the possibility of a short; they did not positively confirm it.

As a whole, the strut data in figures 25 to 28 show low positive strut temperature gradients with hydrogen in the test tank and negative gradients with nitrogen as the fluid. The heat-transfer rates for the all-black struts were slightly less than those for the half-black struts. Also, analysis showed that when shields were present, the heat-transfer rates for both the all-black and half-black struts were less than the heat-transfer rates for insulated struts. These results are in contrast to the results of the tests with no shields in two respects:

(1) With no shields the heat-transfer rates for either the half-black or all-black struts were greater than the rates for the insulated struts.

(2) With no shields the rates for the all-black struts were greater than the rates for the half-black struts.

Eleven titanium struts, evenly spaced shields. - The three tests discussed in this section (tests 2, 3a, and 3b in table II) are tests with 11 titanium struts and 1 fiberglass strut. One titanium strut had an all-black coating, while all the other struts were half black.

Shields: Figures 29 and 30 give the sheet and ring temperature profiles for these tests. The sheet temperature profiles are very similar to those shown in figures 23 and 24, with the analysis again overpredicting the temperatures of the cold sheet of the warm shield. There was good agreement between the analytic and experimental temperatures for both the warm- and cold-shield rings, at either heater setting. The dip in the temperature profile for the warm sheet of the cold shield, as shown in figure 30, was caused by a shortcoming in the analytic procedure. This shortcoming resulted from the simplification in the directional model of assuming uniform-temperature sheets. Therefore, correcting for directional properties caused the temperatures across the entire sheet to be lowered by the same amount. However, the ring temperature was not changed by the directional correction, and the sheet temperature profile at the edge of the sheet had to connect to the ring temperature. This resulted in the sharp upturn in

the sheet profile at the shield ring. If the restriction of uniform-temperature sheets were removed from the directional model, lateral conduction would result in the dip being smoothed.

Figure 30(a) shows additional sheet temperature profiles. These profiles were calculated by assuming that the emissivity on the internal surfaces of the sheets was one-third less than that on the outside surface. The results show that such an emissivity difference was necessary to account for the temperature difference between the analytic and experimental profiles for the cold sheet of the warm shield. Because of its more protective environment, it is possible that the internal emissivity would be less than that on the external surface. However, after the testing was completed and the shields were disassembled, the internal and external emissivities were measured. No significant difference was found between the two sides. This does not preclude one existing during the tests, but a large difference is unlikely.

Struts: Figures 31 to 33 show the analytic and experimental strut temperatures for the three tests. Part (a) of each figure contains the profiles for the half-black titanium struts, while part (b) is for the half-black fiberglass strut. Part (c) contains the temperature profiles for the all-black titanium strut. Generally, there was good agreement between the analysis and the experimental data. There was much better agreement for the single fiberglass strut than for the 12 fiberglass struts discussed previously. The analytic temperature for the fiberglass strut profiles in each figure has a bump at the location of the cold shield. This bump was caused by the shield ring temperature being strongly influenced by conduction through the titanium struts. Enough energy was transferred through the bushing to thermally short the fiberglass strut to the shield ring.

Figures 31 to 33 show that with either hydrogen or nitrogen in the test tank, there was good agreement in the temperature profiles for all the titanium struts. The effect of considering strut contact resistance and the end plug thermal short was much less when shields were present. Analytic temperature profiles including this effect are coincident with those shown in the figures from the start of the plug to the heater. The strut temperature was constant from the start of the strut to the end of the plug.

Eleven titanium struts, closely spaced shields. - Tests 4, 5a, and 5b were conducted to examine secondary effects in the strut-shield thermal system. The effect of moving the warm shield closer to the heater was investigated. The errors introduced by using aluminized tape to cover the sheet thermocouples were examined. Also, the thermal effects resulting from replacing Micarta as the shield ring bushing material were studied. In this series, nitrogen was the only fluid used in the test tank. One test was made with a room-temperature heater setting, and two were made with a high-temperature setting. All three tests were made with the warmest sheet spaced 1.3 centimeters (0.5 in.) from the heater. The spacing between the shields remained the same

as in the evenly spaced shield tests. Consequently, the distance between the coldest sheet and the tank centerline increased by 7.9 centimeters (3.1 in.).

Shield spacing: Figure 34 shows the analytic and experimental temperatures with the room-temperature heater setting, and figure 35 is for the high-temperature heater setting. Both the analytic and experimental sheet profiles shown in figure 34 are very similar to those shown in figures 24 and 30 for the evenly spaced shields. Figure 34 also shows the variation in the analytic profiles caused by neglecting directional effects. Because of the closer spacing between the heater and the warmest sheet, the directional effects were less for the warm shield with closely spaced shields than with evenly spaced shields. The agreement between the analytic and experimental warm ring temperatures was not as good as with evenly spaced shields. This result can be seen in both figures 34 and 35(b). A possible reason for this lack of agreement was the difficulty in setting the shields perfectly level. Typically, there was a difference in elevation of about 0.3 centimeter (0.13 in.) around the edge of the shield. The linear temperature gradient between the heater and the warm-shield ring is

$$\frac{(296-200)}{1.3} \frac{\text{K}}{\text{cm}} \left(\frac{(533-360)}{0.5} \frac{\text{°R}}{\text{in.}} \right) .$$

A 25 percent variation in the denominator of the gradient would significantly influence the ring temperature and would be sufficient to account for the difference between analytic and experimental ring temperatures.

The data in figure 35(a) show that the struts significantly affected the ring temperature. This test was conducted primarily to study the effects of the bushings between the struts and the shield rings. The bushings were completely removed from some of the struts so that only 9 of the 11 titanium struts were connected to the shield ring. In addition to the analytic prediction assuming nine struts connected to the shield ring, a profile is shown in figure 35(a) that assumed that none of the struts were connected to the shield rings. The primary effect was a change in both shield ring temperatures. In addition, the temperatures near the outer edge of both sheets of the colder shield were lowered.

Thermocouple covering: Figure 35(b) shows the results of two different methods used to cover the thermocouples and their leads. The initial method was to use aluminized tape. Even though this aluminized surface had a room-temperature emissivity of 0.06, which was twice the emissivity of the sheet surface, the ratio of the tape emissivity to that of the bare wire was less than one-tenth. In an effort to determine the effect of the tape covering, three of the thermocouples on the colder sheet of each shield were

covered with the sheet material. Strips of the sheet material were taped over the thermocouple leads in the same way that the tape had been applied. The sheet material was attached to double-backed tape and applied directly to the aluminized tape.

The results in figure 35(b) show a significant increase in the measured temperatures for the cold sheet of the warm shield when the sheet material was used as the covering. The increase was very slight for the cold sheet of the cold shield. This figure also shows an apparent temperature difference across the warmest sheet. This temperature difference did not really exist and was caused by all the thermocouples on both sides of this sheet being covered with aluminized tape. Those on the outside faced the heater and had a higher absorptivity than the sheet material. Thus, the local temperature was higher. Those on the inside faced the colder sheet and had a higher emissivity. Thus, the local temperature was lower.

The appropriateness of applying the sheet temperature corrections given in table VII is shown by the data in figure 35(b) for the thermocouples on the outside of the cold sheet of the warm shield. The experimental temperature ratio of the sheet-covered thermocouples to the tape-covered thermocouples was very close to that given in table VII for the same sheet. The analytic data in table VII give the ratio which was applied to the readings for the tape-covered thermocouples to reflect the temperature of the actual sheet.

Struts with closely spaced shields: Figure 36 shows the analytic and experimental temperature profiles for the half-black titanium and fiberglass struts, as well as for the all-black titanium strut. These results are very similar to those shown in figure 33 for evenly spaced shields. The agreement was good between the analysis and experimental data for each of the three types of struts.

Bushings between struts and shield ring: All the previous testing was done with Micarta bushings between the struts and the blocks attached to the shield rings. Prior to performing the analysis, Micarta was chosen as a low-conductivity bushing material. The analysis showed these bushings to have little thermal resistance. Consequently, the standard analysis neglected the resistance between the struts and the shield ring. Figures 37 to 40 show the results of tests designed to investigate the effects of the bushing material.

Figures 37 and 38 show the results for the half-black titanium struts. For two struts the Micarta bushings were replaced with aluminum bushings. For two additional struts the bushings were removed altogether. Figure 37(a) gives the experimental temperatures for the struts with bushings and the high heater setting. Figure 37(b) gives the temperature for the struts with no bushings. Figure 38 is similar to figure 37 except that the heater was at room-temperature setting. There are two analytic profiles for each part of each figure. The standard analysis assumed that the struts were connected to the ring so that they were at the same temperature as the ring when they

passed through the shields. The other profile assumed no heat transfer between the struts and the ring when the struts passed through the shields. An examination of figures 37 and 38 shows that with either bushing material the half-black titanium struts were thermally connected to the shield rings. As would be expected the results for the struts with no bushings agreed with the disconnected profile.

Figures 39 and 40 give the temperature profiles for the half-black fiberglass strut and the all-black titanium strut with the same heater settings as in figures 37 and 38, respectively. Part (a) of each figure gives the results with the bushings removed for the half-black fiberglass strut. Unlike the half-black titanium strut temperatures shown in figures 37(b) and 38(b), the half-black fiberglass strut temperatures shown in figures 39(a) and 40(a) were in good agreement with the profile that assumed the strut was thermally connected to the shield rings when there were no bushings. Even without bushings, enough energy was transferred from the inside of the aluminum block by radiation to thermally bind the fiberglass strut to the ring. Calculations that assumed the strut to be physically disconnected, so that there was no conduction path, but which included radiation between the strut and the block showed the low-conductivity fiberglass strut to be thermally connected to the rings. The all-black titanium strut shown in figures 39(b) and 40(b) had Micarta bushings, and its profiles agreed with the connected profile. There was less of a difference between the connected and disconnected profiles for the all-black titanium strut than for the half-black titanium struts, because the radiant heat-transfer rate was higher on the all-black surfaces.

Heat-Transfer Rates with Shields

When the shields were placed between the heater and the tank, the measured heat-transfer rate was approximately 1 watt (3.4 Btu/hr) or less. The heat-transfer rate was positive with hydrogen as the test fluid and negative when nitrogen was used. With hydrogen in the tank the pressure inside the shroud was in the range 1×10^{-6} to 7×10^{-5} torr. (This is the range of test pressures shown in table II plus the pressure during an additional test, 6a', which had conditions similar to test 6a but a higher shroud pressure of 7×10^{-5} torr.) In this range, heat transfer by gaseous conduction was significant with respect to the measured value. For this reason the discussion of the heat-transfer rates with shields is preceded by a discussion of the effects of gaseous conduction.

Heat transfer by gaseous conduction. - The analysis used to determine the gaseous conduction heat transfer is presented in appendix D. The analysis was used for comparison with a series of null tests. In the null tests the heater was allowed to cool to the cryoshroud temperature. This temperature was about 5.5 K (10^0 R) warmer than that

of the hydrogen in the test tank.

Figure 41 gives the measured heat-transfer rate for a series of null tests as a function of the vacuum ionization gage pressure. The null test results are denoted by triangular symbols. Also shown in this figure are square symbols giving the heat-transfer rate with the heater at room temperature or higher and hydrogen in the test tank. The square symbol at 7×10^{-5} torr pressure (test 6a') is a duplicate of test 6a except with a higher pressure. The data for this test have not been included in the previous discussion.

There are two analytic curves, each corresponding to a different assumption for the pressure inside the shroud. One assumption was that the pressure measured by the gage is the pressure between the tank and the cryoshroud. This assumption was valid in the continuum region, where the pressure was greater than about 2×10^{-3} torr. The other assumption was that P/\sqrt{T} is a constant and is valid in the free molecular region where the pressure was less than about 2×10^{-5} torr. Even though the gage was mounted to the cryoshroud, other tests showed that the gage temperature could have been as much as a factor of 10 times higher than the cryoshroud temperature. The dashed curve in figure 41 assumes this to be the case, and results in a factor of 3 difference in the heat-transfer rate at low pressure. The analytic curves give the trend of the null test and show that the heat-transfer rate was relatively independent of pressure at the higher pressures.

Comparing the square symbols with the triangular symbols in figure 41 shows that the null gaseous conduction heat-transfer rate was a significant portion of the heat-transfer rate with either heater setting. Furthermore, gaseous conduction was even more significant with the heater operative. That portion of the gaseous conduction heat transfer to the tank which occurred between the coldest sheet and tank was higher with the heater turned on. This was a consequence of the sheet being much warmer than the cryoshroud when the heater was at room temperature or higher. With nitrogen in the test tank the pressure inside the shroud was 3.3×10^{-7} torr or lower, so that heat transfer by gaseous conduction was small.

Gaseous conduction affects not only the heat transfer to the tank but also can affect the sheet temperatures for the shield. Figure 42 gives the normalized experimental temperatures for the coldest sheet as a function of shroud pressure. The temperatures for the data points were normalized by dividing the experimental temperature by the predicted temperature and assuming no gaseous conduction. Also shown is an analytic curve giving the coldest sheet temperature as a function of pressure. This normalized temperature is the predicted temperature divided by the temperature at zero pressure. This normalized temperature first decreased and then increased with increasing pressure because the gaseous conduction terms were nonlinear with respect to pressure. In the free molecular region the terms are proportional to pressure but independent of the

spacing between surfaces. In the continuum region, however, the terms are independent of pressure but proportional to the inverse of the distance between surfaces. In the free molecular region the coldest sheet cooled with increasing pressure. In the continuum region the other sheet of the shield was close enough to reduce the temperature difference between the sheets of the shield. This resulted in the cold sheet warming with pressure, as is shown at the higher pressures in figure 42. The experimental data given in this figure show that the lower than expected temperatures for the coldest sheet in figure 24(a) could be accounted for by the effect of gas pressure inside the shroud. Because of the higher radiant heat transfer on the warmer sheets, they were not as responsive to the effects of gaseous conduction.

Comparison of heat-transfer rates. - Table VIII gives the experimental and analytic heat-transfer rates. The measured values are given as the total heat-transfer rate. The adjacent column is the strut conduction heat-transfer rate based on the analytic thermal conductivity and the experimental strut temperatures 3.8 centimeters (1.5 in.) from the tank end. Both the thermal short and contact resistance were neglected in calculating the experimental and analytic strut conduction heat transfer. The analytic strut conduction terms given in the last column result from the analytic temperatures. While the agreement between the analytic and the experimental temperature differences was not good, the experimental values were subject to much uncertainty. For test 2 with hydrogen in the tank the uncertainty in the thermocouple was about 60 percent of the temperature difference; in test 3a with nitrogen, the uncertainty was about 50 percent. Only when there were titanium struts was the strut conduction heat-transfer rate significant.

With hydrogen in the test tank, heat transfer by gaseous conduction predominated. This calculation was based on the experimental shroud and coldest sheet temperatures. Unfortunately, there is a very high degree of uncertainty in these values. The accommodation coefficients are not known accurately. For the tests with hydrogen, two values of the gaseous conduction heat-transfer rate are given. Those under the heading " $P/\sqrt{T} = \text{Constant}$ " correspond to an assumption that is valid in the free molecular region. Those under the heading " $P = \text{Constant}$ " are for an assumption that is valid in the continuum region. Because the pressure was relatively low in the tests with nitrogen only, the results for the free molecular pressure assumption are given. Even with nitrogen in the tank it was assumed that the medium for gaseous conduction was hydrogen since hydrogen was always in the shroud. Assuming the medium was nitrogen would have reduced the rate by about 40 percent.

The radiation heat-transfer rate was significant only with nitrogen in the tank and was nearly a constant for all tests with the same fluid. The surface of the tank facing the heater exchanged radiant heat with the coldest sheet and the struts. In addition, the entire surface of the tank exchanged energy with the cryoshroud. As mentioned pre-

viously, the strut support ring at the tank formed an annular cavity. Assuming this annular cavity to be a black emitter resulted in the cavity emitting nearly 40 percent of the total radiant heat-transfer rate.

The unaccounted heat-transfer rate was the measured value minus the sum of strut and gaseous conduction as well as radiation. Tests 3a and 3b had nearly the same measured heat-transfer rate. Tests 4 and 5b also had nearly the same rate. The rates for both pairs differed by about 0.4 watt (1.3 Btu/hr). Analytically, all four rates should have been nearly the same. Examination of test data revealed a possible leak in the measuring system during tests 2, 3a, and 3b which would account for some of the difference. In all the other tests the unaccounted-for heat-transfer rate was about 0.4 watt (1.4 Btu/hr) or less with the free molecular pressure assumption.

CONCLUDING REMARKS

The tests showed that shadow shields can be very effective in reducing the heat transfer to a cryogenic propellant in a deep-space mission. The low-emissivity shields reflect the radiant energy emitted from the surface of the payload to space, thereby preventing it from being absorbed on the surface of the propellant tank.

The analysis and the experimental data for the heat-transfer rates with no shields were in good agreement only after account was taken of the nongray absorptivity of the tank surface and the heat absorbed by an annular cavity adjacent to the test tank. These results showed the following:

- (1) When the absorptivity is a strong function of temperature, consideration must be given to the temperature of the emitting surface as well as that of the absorbing surface.
- (2) Care must be taken to ensure that all surfaces have the desired properties so as to minimize stray heat transfer to a propellant tank.

For the tests conducted with shadow shields there was significant disagreement between the analytic and experimental temperatures for the cold sheet of the warm shield. The cause of this disagreement remains a mystery even though many calculations were made to determine the effects of possible means of heat transfer to both the whole shield and the thermocouple junctions. No explanation consistent with the experimental data was found which would align the analytic and experimental temperatures for this sheet. This problem complicates the acceptance of the directional model. Assuming the experimental temperatures for the cold sheet of the warm shield to apply for the entire sheet resulted in the analysis accurately predicting the temperatures of both sheets of the cold shield without having to apply the directional corrections. However, if the analysis was used to predict the true temperatures for the cold sheet of the warm shield, the directional model was needed to predict the temperatures of both sheets of the cold shield.

With shields present, both the analysis and the experimental data showed heat-transfer rates to be slightly less for the all-black struts than for the half-black struts. Thus, with shields it may not be necessary to resort to the complexity of a low-emissivity coating on the inward side of the strut and a high-emissivity coating on the outward side to obtain low heat transfer to the propellant tank. Coating the entire exterior of the strut would result in heat-transfer rates less than that of an insulated strut.

In the test program conducted, the heat-transfer rates with shields and hydrogen in the tank were dominated by gaseous conduction. These tests underscore the necessity of having a good vacuum when low heat-transfer rates are expected. With nitrogen in the tank, radiation from the tank was the major mode of heat transfer. Consequently, the agreement between the analysis and experimental data might have been better if surface properties had been known more accurately at cryogenic temperatures.

The results of the test program show that the analysis is a good tool for the prediction of thermal performance associated with cryogenics in space. In tests with no shields the analysis gave good predictions for the heat-transfer rates and adequate predictions for the strut temperatures. With shields present the analysis gave good predictions for the temperatures of the titanium struts and fair predictions for the fiberglass struts. The applicability of the analysis for the prediction of heat-transfer rates and shield temperatures is more clouded. Only after account had been taken of directional properties did the analysis adequately predict the sheet temperatures for the cold shield. However, the uncertainty in the room-temperature sheet emissivity resulted in uncertainties for the sheet temperatures of the colder shield which were relatively large. The analysis significantly overpredicted the temperatures of the cold sheet of the warm shield. One would be more confident in the analysis if the cause of this discrepancy was resolved.

SUMMARY OF RESULTS

The thermal performance of shadow shields, and their support struts, for the thermal protection of cryogenic propellants in a simulated deep-space environment was investigated analytically and experimentally. Tests were run with both liquid hydrogen and liquid nitrogen as the test fluids. Heat transfer was measured by boiloff or by maintaining thermodynamic equilibrium. A heater with a high-emissivity coating was operated at temperatures of 294 and 389 K (530^o and 700^o R) in place of the payload. The high-emissivity heater was used to accentuate the thermal radiation effects. Tests were run on both fiberglass and titanium struts.

Qualitatively, the agreement between the analysis and the experimental temperature and heat-transfer data was good. With nitrogen in the test tank, both the experimental data and the analysis showed that the heat-transfer rate to the tank went from positive to negative when shields were placed between the heater and the tank. With hydrogen as the test fluid the experimental data showed reductions in the heat-transfer rate by about a factor of 30 when shields were placed between the heater and the tank. The analysis showed that, when there was no gaseous conduction heat transfer, there was a reduction of nearly two orders of magnitude in the heat-transfer rate when shields were used.

The qualitative agreement in the strut temperatures was good. When no shields were present, both the analysis and experimental data showed that the radiant energy from the heater so influenced the half-black and all-black strut temperature profiles that their tank-end gradients were much greater than that for an insulated strut. Using shields, however, resulted in tank-end gradients that were actually negative with nitrogen in the test tank. This effect resulted from the shields reflecting much of the heater energy to the cryoshroud while the struts still radiated to the cryoshroud.

The biggest area of quantitative disagreement was in the temperature of the cold sheet of the warm shield. The analysis predicted the temperature of the warmest sheet well. Accounting for directional properties resulted in good agreement for the temperatures of both sheets of the cold shield.

Generally, there was good agreement in the strut temperature profiles both with and without shields. Without shields the analysis tended to underpredict the tank-end temperature gradient for the titanium struts. However, this probably was the result of neglecting a series combination of a thermal short and contact resistance at the tank end of the strut. With shields, there was good agreement in the temperatures of the titanium struts; however, the analysis underpredicted the tank-end profile in the tests where all the struts were fiberglass.

There was good correlation between the analytic and experimental heat-transfer rates in the tests with no shields. With shields and hydrogen in the test tank, the quantitative agreement in the heat-transfer rates was not good. This disagreement was caused by the failure of the analytic assumptions to predict accurately the heat transfer by gaseous conduction. The gaseous conduction heat transfer is subject to a high degree of uncertainty, and the pressure inside the shroud was sufficiently high that this mode of heat transfer was the dominant one. With shields and nitrogen in the test tank, the net heat-transfer rate was from the tank. The pressure was sufficiently low that gaseous conduction was not significant. Nevertheless, the analysis accounted for only about 40 percent of the heat-transfer rate.

Both the analysis and the experimental data showed that the shield temperatures were relatively independent of the choice of fluid in the tank and nearly proportional to the heater temperature. Also the agreement was unaffected by changing the spacing of

the warm shield relative to the heater. Even the relatively low-conducting Micarta bushings were unable to prevent the struts from being thermally bound to the shield rings.

Lewis Research Center,
National Aeronautics and Space Administration,
Cleveland, Ohio, October 17, 1973,
502-24.

APPENDIX A

SYMBOLS

A	area, cm^2 (in. ²)
a	accommodation coefficient
B	radiosity, W/cm^2 (Btu/hr-in. ²)
\bar{C}	coefficient matrix, cm^2 (in. ²)
c	specific heat, J/g-K (Btu/lb- ⁰ R)
c_v	specific heat at constant volume, J/g-K (Btu/lb- ⁰ R)
d	distance, cm (in.)
E	energy of molecules per unit time and area, W/cm^2 (Btu/hr-in. ²)
F	view factor
\bar{F}	matrix of view factors
\mathcal{F}	script radiant interchange factor
\bar{f}	vector of view factors
G	incident energy per unit time and area, W/cm^2 (Btu/hr-in. ²)
\bar{G}	matrix of incident energies, W/cm^2 (Btu/hr-in. ²)
\bar{g}	vector of incident energies, W/cm^2 (Btu/hr-in. ²)
H	incident radiant energy due to all temperatures, W/cm^2 (Btu/hr-in. ²)
h	vector component on vertical axis, cm (in.)
J	reflected energy, W/cm^2 (Btu/hr-in. ²)
k	thermal conductivity, $\text{W}/\text{cm-K}$ (Btu/hr-in. - ⁰ R)
L	mean free path, cm (in.)
l	length, cm (in.)
M	molecular weight
m	number of surfaces in an enclosure
N	number of struts
\bar{N}	normal vector, cm (in.)
n	number of nodes in an enclosure
P	coordinate position, cm (in.)
p	pressure, torr
q	heat-transfer rate per unit area, W/cm^2 (Btu/hr-in. ²)
R	radius, cm (in.)
R_u	universal gas constant, units as appropriate
\mathcal{R}	random number
r	radial position, cm (in.)

S	distance between area elements, cm (in.)
s	mass of molecules passing a unit area in unit time, g/cm ² -hr, (lb/in. ² -hr)
T	temperature, K (⁰ R)
\bar{T}	vector of temperatures, K (⁰ R)
t	thickness, cm (in.)
\bar{U}	vector perpendicular to \bar{N} and \bar{W}
V	volume, cm ³ (in. ³)
\bar{V}	vector between points, cm (in.)
\bar{v}	mean molecular velocity, cm/hr (in./hr)
\bar{W}	vector perpendicular to \bar{N} and \bar{V}
x	axial distance, cm (in.)
β	angle with normal
γ	ratio of specific heats
δ_{ij}	Kronecker delta
ϵ	emissivity
η	index of refraction
θ	circumferential angle
κ	extinction coefficient
λ	wavelength, cm (in.)
μ	viscosity, g/cm-hr (lb/in.-hr)
ξ	jump distance of temperature discontinuity, cm (in.)
ρ	density, g/cm ³ (lb/in. ³)
σ	Stefan-Boltzmann constant, W/cm ² -K ⁴ (Btu/hr-in. ² - ⁰ R ⁴)
τ	time, hr
ψ	circumferential angle on strut
ω	solid angle

Subscripts:

a	axial
c	circumferential
H	heater
i, j, k, l	indices denoting surfaces
r	ring
s	source
sh	sheet of shield
sh1	one of two sheets in an enclosure
sh2	the other of two sheets in an enclosure
sr	surroundings

st	strut
T	tank

Superscripts:

c	conduction
i	inside
o	outside
r	radiation
*	cumulative value
'	in stream

APPENDIX B

DERIVATION OF THERMAL ENERGY EQUATIONS

The temperature profiles for the shields and struts were found by taking energy balances. To do this, the entire system was divided into one or more enclosures. A schematic of the thermal system is shown in figure 7. The heater and tank were two sources at known temperature. The shields were placed between these two surfaces. The purpose of the shields is to reduce the amount of energy emitted from the heater that is absorbed by the tank. Therefore, it was assumed that a surface sees only one shield or source. It was assumed that the shields and sources are axisymmetric. In addition, there may be one or more struts. The surroundings were the final element considered in the energy balance. The surroundings would be either space or the walls of the test chamber. The energy balances were performed by first dividing the system into a series of enclosures. There were two types of enclosures, and both are shown schematically in figure 43. In the first type of enclosure, figure 43(a), the shields see the surroundings. This enclosure may contain one sheet from each of two shields and the struts between the shields. A source may be substituted for either of the shields without affecting the analytic procedure. The surroundings are shown by a dashed line. When the surroundings are black and at zero temperature, such as for the analysis of a vehicle in space, their area does not affect the energy balance. In the tests, baffling was used so that the dashed lines truly represent the actual surroundings.

The second type of enclosure, figure 43(b), contains only a shield and surroundings. Here the inner portion of the sheets does not see the surroundings. They are blocked from doing this by the circumferential ring. The inner parts of the sheets see only each other and the inside surface of the ring. If the sheets extend beyond the ring, the outer portion of the sheets will see both the outer surface of the ring and the surroundings. Generally, when there is a ring present, the distance between sheets is small. For this reason the effect of radiant heat transfer on the struts in this type of enclosure was neglected.

The temperature for each node on the shields and struts was found by equating the net rate at which heat is absorbed by the node to the rate of change of thermal capacitance of the element. For a vacuum it is necessary only to consider radiant and conductive heat transfer. Except for the sources and the surroundings, each node has two surface elements. For the shield sheets, these elements lie in different enclosures.

A transient analysis was made both to determine that the time to achieve equilibrium was short and to provide good temperature estimates for the steady-state solution. The rate of change of thermal capacitance for any node is given by $\rho V c (\partial T / \partial \tau)$.

For a shield it was assumed that there is no temperature gradient across the thickness of the sheet. Also, it was assumed that there is no circumferential gradient in the sheet. In reality, radiant energy from the struts was not distributed uniformly around the shield. However, if the effect of a strut on the shield is not large, the assumption of no circumferential gradient is valid. Also, if there are many struts around the shield, the circumferential gradient will be small. The volume of a sheet node becomes

$$V_{sh} = 2\pi t_{sh} \int r_{sh} dr_{sh} \quad (B1)$$

For a strut it was assumed that there is no gradient across the thickness of the strut. The volume for the strut node is

$$V_{st} = t_{st} R_{st} \iint d\psi_{st} dx_{st} \quad (B2)$$

The assumption was made that the ring is at a uniform temperature. The volume element becomes the entire volume of the ring

$$V_r = 2\pi R_r t_r l_r \quad (B3)$$

Heat is transferred into the shield sheet element by both radiation and conduction. Some of the radiant energy absorbed by the sheet element comes from the two adjacent sheets. Also, all the elements of the sheet emit energy, some of which is absorbed by the element under consideration. In addition, the elements of the strut transfer energy to the sheet element. Finally, if the surroundings are not at zero temperature, they also transfer energy to the sheet element.

In this analysis it was assumed that the surfaces are gray. This means that the absorptivity and emissivity are equal on the surface of each element. It was also assumed that the surfaces emit and reflect energy diffusely. Reference 5 compares the effect of assuming diffuse surfaces on the heat-transfer rate for shield surfaces that are truly specular. At certain spacing ratios and with low emissivity, there may be a significant difference in the results. However, few surfaces are truly specular or diffuse. Reference 17 indicates that the relatively simple diffuse model is a reasonably

accurate model for most real surfaces. However, the effects of directional properties can be significant for the sheet temperatures of the shields. But, to make the analysis using directional properties for the sheets was impractical because of the excessive amount of computer time required. The effects of directional properties were approximated by determining the temperature change in a sheet with a single node and applying this temperature change to all the nodes of the sheet calculated by the diffuse assumption. Appendix C gives details to the directional calculations.

Radiant energy is absorbed by both sides of the shield node. Let the subscripts i and j designate each surface element on either side of the sheet. The radiant heat-transfer rate into the node is given by

$$q_{sh}^r = \int [\epsilon_i H_i + \epsilon_j H_j - (\epsilon_i + \epsilon_j) \sigma T^4] dA_{sh} \quad (B4)$$

where H_i is the radiant energy incident on the i^{th} surface per unit time and area. The radiosity of the i^{th} element is the rate at which energy leaves the i^{th} surface. This quantity is given by the equation

$$B_i = \epsilon_i \sigma T^4 + (1 - \epsilon_i) H_i \quad (B5)$$

The incident radiant energy is expressed in terms of the radiosities by the equation

$$H_i = \sum_{k=1}^m \int B_k dF_{dA_i-dA_k} \quad (B6)$$

The quantity $dF_{dA_i-dA_k}$ is the differential view factor from the differential area dA_i to the differential area dA_k . The view factor is a differential because the receiving area dA_k is a differential.

The radiosity B remains inside the integral because it is a function of both the surface involved and the position on the surface. The term $dF_{dA_i-dA_k}$ comes from the reciprocity equation

$$dF_{dA_i-dA_k} = \frac{dF_{dA_k-dA_i} dA_k}{dA_i} \quad (B7)$$

The integration in equation (B6) is done over the entire surface. The summation sign is needed because there is more than one surface in the enclosure. The equation for the incident energy on the j^{th} surface is

$$H_j = \sum_{\ell=1}^m \int B_{\ell} dF_{dA_j-dA_{\ell}} \quad (B8)$$

The number of surfaces seen from each side of the sheet element is generally not the same. One surface of the sheet is in an enclosure shown in figure 43(a). The other is in the enclosure shown in figure 43(b). Let the i^{th} surface be the one seeing the source. Then H_i is given by

$$H_i = \left(\int^B dF_{dA_i-dA} \right)_s + \left(\int^B dF_{dA_i-dA} \right)_{sh} + \left(N \int^B dF_{dA_i-dA} \right)_{st} + \left(\int^B dF_{dA_i-dA} \right)_{sr} \quad (B9)$$

If the element of the sheet is inside the ring, H_j is given by

$$H_j = \left(\int^B dF_{dA_j-dA} \right)_{sh2} + \left(\int^B dF_{dA_j-dA} \right)_{sh1} + \left(\int^B dF_{dA_j-dA} \right)_r \quad (B10a)$$

If the element is outside the ring, H_j is given by

$$H_j = \left(\int_{\text{sh2}}^{\text{B}} dF_{dA_j-dA} \right) + \left(\int_{\text{sh1}}^{\text{B}} dF_{dA_j-dA} \right) + \left(\int_{\text{r}}^{\text{B}} dF_{dA_j-dA} \right) + \left(\int_{\text{sr}}^{\text{B}} dF_{dA_j-dA} \right) \quad (\text{B10b})$$

It was assumed that the shields are flat. Therefore, the surface area of the shield element is given by $dA_{\text{sh}} = 2\pi r_{\text{sh}} dr_{\text{sh}}$. The equation for the heat gained by the element per unit time due to radiation is

$$q_{\text{sh}}^{\text{r}} = 2\pi \int \left[\epsilon_i \sum_{k=1}^m \int^{\text{B}_k} dF_{dA_i-dA_k} + \epsilon_j \sum_{\ell=1}^m \int^{\text{B}_\ell} dF_{dA_j-dA_\ell} - (\epsilon_i + \epsilon_j)\sigma T^4 \right] r_{\text{sh}} dr_{\text{sh}} \quad (\text{B11})$$

The number of surfaces m is not the same for each summation, since one side of the sheet does not receive strut radiation.

The heat transferred to the node by conduction occurs at the inner and outer radius of the node. The rate of heat gained by the node due to conduction is

$$q_{\text{sh}}^{\text{c}} = 2\pi t_{\text{sh}} k_{\text{sh}} \left(r_{\text{sh}}^{\text{o}} \frac{\partial T}{\partial r} \Big|_{r=r_{\text{sh}}^{\text{o}}} - r_{\text{sh}}^{\text{i}} \frac{\partial T}{\partial r} \Big|_{r=r_{\text{sh}}^{\text{i}}} \right) \quad (\text{B12})$$

Equating the rate of increase in the capacitance of the shield to the net heat rate from radiation and conduction gives

$$\rho_{sh} V_{sh} c_{sh} \frac{\partial T}{\partial \tau} = q_{sh}^r + q_{sh}^c$$

Expanding terms gives

$$\begin{aligned} & 2\pi\rho_{sh} c_{sh} t_{sh} \frac{\partial T}{\partial \tau} \int_{r_{sh}} dr_{sh} \\ &= 2\pi \int \left[\epsilon_i \sum_{k=1}^m \int_{B_k} dF_{dA_i-dA_k} + \epsilon_j \sum_{l=1}^m \int_{B_l} dR_{dA_j-dA_l} - (\epsilon_i + \epsilon_j) \sigma T^4 \right] r_{sh} dr_{sh} \\ &+ 2\pi t_{sh} k_{sh} \left(r_{sh}^o \frac{\partial T}{\partial r} \Big|_{r=r_{sh}^o} - r_{sh}^i \frac{\partial T}{\partial r} \Big|_{r=r_{sh}^i} \right) \end{aligned} \quad (B13)$$

The temperature distribution for the strut was found in a similar fashion. Heat is transferred both circumferentially and axially by conduction:

$$\begin{aligned} q_{st}^c = k_{st} t_{st} \left[\left(\frac{\partial T}{\partial x} \Big|_{x=x_1} - \frac{\partial T}{\partial x} \Big|_{x=x_2} \right) R_{st} \int_{\psi_1}^{\psi_2} d\psi_{st} \right. \\ \left. + \frac{1}{R_{st}} \left(\frac{\partial T}{\partial \psi} \Big|_{\psi=\psi_1} - \frac{\partial T}{\partial \psi} \Big|_{\psi=\psi_2} \right) \int_{x_1}^{x_2} dx \right] \end{aligned} \quad (B14)$$

where x_1 and x_2 give the distance along the strut for the element and ψ_1 and ψ_2 give the angular distance around the strut.

It was assumed that radiant heat is transferred basically only to the outward surface

of the strut. This assumption would be true if the inside of the strut were filled with an opaque and nonconducting material. Modifications were made to the final set of finite difference equations to allow for internal radiation between circumferential nodes at the same axial position. The equation for the heat-transfer rate to the outside strut element by radiation is

$$q_{st}^r = R_{st} \iint \epsilon_i (H_i - \sigma T^4) d\psi dx \quad (B15)$$

The subscript i is used to designate the element. The incident radiant energy is given by

$$H_i = \sum_{k=1}^m \int B_k dF_{dA_i-dA_k} \quad (B16)$$

If there are many struts, there will be a large number of surfaces. Each of these struts will influence the strut under consideration differently. In reality a strut diagonally opposite has smaller view factors to the element than an adjacent strut. The two shields or sources see the strut. Also the surroundings see the strut. The components of the right side of equation (B16) are

$$\begin{aligned} \sum_{k=1}^m \int B_k dF_{dA_i-dA_k} &= \left(\sum_{k=1}^N \int B_k dF_{dA_i-dA_k} \right)_{st} + \left(\int^B dF_{dA_i-dA} \right)_s \\ &+ \left(\int^B dF_{dA_i-dA} \right)_{sh} + \left(\int^B dF_{dA_i-dA} \right)_{sr} \end{aligned} \quad (B17)$$

The view factor between struts was assumed to be zero so that the first term on the right side in the preceding equation was neglected. Equating the net heat-transfer rate to the strut element by conduction and radiation to the increase in the capacitance of the element gives

$$\begin{aligned}
& \rho_{st} c_{st} t_{st} R_{st} \frac{\partial T}{\partial \tau} \int_{x_1}^{x_2} \int_{\psi_1}^{\psi_2} d\psi_{st} dx_{st} \\
& = k_{st} t_{st} \left[R_{st} \left(\frac{\partial T}{\partial x} \Big|_{x=x_2} - \frac{\partial T}{\partial x} \Big|_{x=x_1} \right) \int_{\psi_1}^{\psi_2} d\psi_{st} + \frac{1}{R_{st}} \left(\frac{\partial T}{\partial \psi} \Big|_{\psi=\psi_1} - \frac{\partial T}{\partial \psi} \Big|_{\psi=\psi_2} \right) \int_{x_1}^{x_2} dx \right] \\
& \quad + R_{st} \int_{x_1}^{x_2} \int_{\psi_1}^{\psi_2} \epsilon_i \left(\sum_{k=1}^m \int B_k dF_{dA_i-dA_k} - \sigma T^4 \right) d\psi dx
\end{aligned} \tag{B18}$$

On calculating the conduction heat-transfer rate to the ring, it can be assumed that the struts are attached to the ring. The conduction heat-transfer rate into the ring is given by

$$q_r^c = 2\pi R_r t_r k_r \left(\frac{\partial T}{\partial x} \Big|_{x=\ell} - \frac{\partial T}{\partial x} \Big|_{x=0} \right) \tag{B19}$$

This value can also be expressed in terms of the heat-transfer rate from the struts as

$$q_r^c = N k_{st} t_{st} R_{st} \int \left(\frac{\partial T}{\partial x} \Big|_{x=\ell} - \frac{\partial T}{\partial x} \Big|_{x=0} \right) d\psi_{st} \tag{B20}$$

The boundaries $x = \ell$ and $x = 0$ are measured in the enclosure containing the ring. The gradients used in equation (B20) are measured on the struts. Since the ring was assumed to have a uniform temperature, equation (B20) is used for the heat-transfer rate to the ring by conduction.

The ring can absorb radiant energy on either its inner or outer surface. Let i and j denote the inner and outer surfaces, respectively. The heat-transfer rate to the ring is given by

$$q_r^r = 2\pi R_r \ell_r \left[\epsilon_i H_i + \epsilon_j H_j - (\epsilon_i + \epsilon_j) \sigma T^4 \right] \tag{B21}$$

This equation neglects the difference in the surface area between the inner and outer surfaces of the ring because $t_r \ll R_r$. The incident radiant energy is given by

$$H_i = \sum_{k=1}^m \int B_k dF_{dA_i-dA_k} \quad (B22)$$

Expanding the right side of this equation for the inside surface of the ring gives

$$\begin{aligned} \sum_{k=1}^m \int B_k dF_{dA_i-dA_k} &= \left(\int_0^{R_r} B dF_{dA_i-dA} \right)_{sh1} + \left(\int_0^{R_r} B dF_{dA_i-dA} \right)_{sh2} \\ &\quad + \left(\int B dF_{dA_i-dA} \right)_r \end{aligned} \quad (B23)$$

The upper limit of integration for the sheets is R_r . The reason for this is that the inner surface of the ring receives no radiation from portions of the shield outside of it. The j^{th} side of the ring sees the outer portion of both sheets and the edge of the baffle which acts as the surrounding. The equation for the incident energy on this surface is

$$\begin{aligned} H_j &= \sum_{k=1}^m \int B_k dF_{dA_j-dA_k} = \left(\int_{R_r}^{R_{sh}} B dF_{dA_j-dA} \right)_{sh1} \\ &\quad + \left(\int_{R_r}^{R_{sh}} B dF_{dA_j-dA} \right)_{sh2} + \left(\int B dF_{dA_j-dA} \right)_{sr} + \left(\int B dF_{dA_j-dA} \right)_r \end{aligned} \quad (B24)$$

If the vehicle were in space, so that the baffle was replaced by the nonreflective surrounding of space, the term for the surrounding in this equation would be zero.

Equating the increase in the capacitance of the ring to the net amount of energy absorbed by conduction and radiation gives

$$2\pi R_r t_r \rho_r c_r \ell_r \frac{\partial T}{\partial x} = N k_{st} t_{st} R_{st} \left(\left. \frac{\partial T}{\partial x} \right|_{x=\ell} - \left. \frac{\partial T}{\partial x} \right|_{x=0} \right) d\psi_{st}$$

$$+ 2\pi R_r \ell_r \left[\epsilon_i \sum_{k=1}^m \int_{B_k} dF_{dA_i-dA_k} + \epsilon_j \sum_{k=1}^m \int_{B_k} dF_{dA_j-dA_k} - (\epsilon_i + \epsilon_j) \sigma T^4 \right]$$

(B25)

Solution of Equations

The preceding equations were solved by using the CINDA-3G computer program. This program is described in reference 10. It is a finite-element computer program. First, the struts and shields were divided into a series of nodes. The surfaces of the heater and tank were similarly divided into a series of nodes. The surrounding for each enclosure was one node. Part of the necessary input to the thermal analyzer program was script \mathcal{F} radiation interchange factors. It was also necessary to obtain the geometric view factors over finite surface areas between pairs of nodes. The view factors could not be determined a priori, since it was desirable to be able to vary the number of nodes used. As the number of nodes increased, the solution approached that for the differential equations. But unfortunately the computer time needed to solve the equations also increased rapidly. Having the capability to vary the number of nodes permitted a trade-off between computer time and solution accuracy. The effect of varying the number of nodes is shown in a subsequent section of this appendix.

Determination of script \mathcal{F} 's. - The script \mathcal{F} interchange factors are convenient to use because of their definition. The net radiation heat-transfer rate to the whole surface of the node is expressed in terms of the script \mathcal{F} 's between this node and all other nodes as

$$A_i q_i^R = \sigma \sum_{j=1}^n A_i \mathcal{F}_{ij} (T_j^4 - T_i^4) = \sigma \sum_{j=1}^n A_i \mathcal{F}_{ij} (T_j^2 + T_i^2)(T_j + T_i)(T_j - T_i)$$

(B26)

where n is the total number of nodes which influence the i^{th} node by radiation.

Energy transferred between two nodes by conduction is proportional to the temperature difference between the nodes. By using $A_i F_{ij} (T_j^2 + T_i^2) (T_j + T_i)$ as the proportionality value, radiation components are treated analogously to conduction components.

The derivation of script \mathcal{F} equations is given in reference 8. It is repeated here for convenience. There are a total of n nodes in the enclosure. The radiant energy interchange between each of these nodes and the i^{th} node is found by considering each of the nodes in turn to have a temperature other than zero. Let $G_{i\ell}$ be the incident radiant energy on surface i caused by a thermal potential only on surface ℓ . By summation

$$H_i = \sum_{\ell=1}^n G_{i\ell} \quad (\text{B27})$$

Also, let $J_{k\ell}$ be the component of $G_{k\ell}$ which is reflected off the k^{th} surface:

$$J_{k\ell} = (1 - \epsilon_k) G_{k\ell} \quad (\text{B28})$$

Then

$$B_i = \sigma \epsilon_i T_i^4 + \sum_{\ell=1}^n J_{i\ell} \quad (\text{B29})$$

The radiant heat-transfer rate is linear in T^4 and is found by summing the components found by considering each source in turn. The equation giving the incident energy for the k^{th} surface caused by a potential only on surface l ($\ell = 1$) is

$$G_{k1} A_1 = (\sigma \epsilon_1 T_1^4 + J_{11}) A_1 F_{1k} + J_{21} A_2 F_{2k} + J_{31} A_3 F_{3k} + \dots + J_{n1} A_n F_{nk} \quad \text{for } 1 \leq k \leq n \quad (\text{B30})$$

The simplified notation F_{ij} has been used in place of $F_{A_i-A_j}$.

Since $J_{k1} = (1 - \epsilon_k) G_{k1}$ equation (B30) can be rearranged to eliminate the J 's. This yields

$$\begin{aligned}
& A_1 \left[(1 - \epsilon_1) F_{1k} - \delta_{1k} \right] G_{11} + A_2 \left[(1 - \epsilon_2) F_{2k} - \delta_{2k} \right] G_{21} \\
& + A_3 \left[(1 - \epsilon_3) F_{3k} - \delta_{3k} \right] G_{31} + \dots + A_n \left[(1 - \epsilon_n) F_{nk} - \delta_{nk} \right] G_{n1} \\
& = -\sigma \epsilon_1 T_1^4 A_1 F_{1k} \quad (B31)
\end{aligned}$$

In matrix notation, this is

$$\bar{C} \bar{g} = \sigma \epsilon_1 T_1^4 A_1 \bar{f} \quad (B32)$$

Using view factor reciprocity gives

$$\begin{aligned}
[\bar{C}]_{ik} &= A_k \left[(1 - \epsilon_k) F_{ki} - \delta_{ik} \right] \\
[\bar{g}]_k &= G_{k1} \\
[\bar{f}]_i &= -F_{1i}
\end{aligned}$$

The solution to the matrix equation is

$$\bar{g} = \sigma \epsilon_1 T_1^4 A_1 \bar{C}^{-1} \bar{f} \quad (B33)$$

The net radiant heat-transfer rate to the entire k^{th} surface caused by a potential solely on surface 1 is the difference between the incident and reflected energies:

$$A_k q_{k1}^r = A_k (G_{k1} - J_{k1}) = A_k \left[G_{k1} - (1 - \epsilon_k) G_{k1} \right] = A_k \epsilon_k G_{k1} \quad (B34)$$

Substituting equation (B33) into (B34) gives

$$A_k q_{k1}^r = A_k \epsilon_k \sigma \epsilon_1 T_1^4 A_1 [\bar{C}^{-1} \bar{f}]_k \quad (B35)$$

The net radiant heat-transfer rate to the k^{th} surface caused solely by a potential on surface 1 is expressed in terms of the script \mathcal{F} 's as

$$A_k q_{k1}^r = \sigma A_1 \mathcal{F}_{1k} (T_1^4 - T_k^4) \quad (\text{B36})$$

If $k = 1$, $T_1^4 - T_k^4 = 0$; otherwise T_k^4 is zero.

Equating equation (B35) to (B36) yields

$$\mathcal{F}_{1k} = \epsilon_1 A_k \epsilon_k [\bar{C}^{-1} \bar{F}]_k \quad (\text{B37})$$

The coefficient matrix \bar{C} is independent of the surface having a thermal potential. To find the interchange factors for surfaces other than surface 1, the following equation is used

$$[\bar{C}\bar{G}]_{i\ell} = \sigma \epsilon_\ell T_\ell^4 A_\ell [\bar{F}]_{i\ell} \quad (\text{B38})$$

where

$$[\bar{G}]_{k\ell} = G_{k\ell}$$

$$[\bar{F}]_{i\ell} = -F_{\ell i}$$

Since the right side has each column multiplied by the constant $\sigma \epsilon_\ell T_\ell^4 A_\ell$, the multiplication by the inverse \bar{C}^{-1} results in answers multiplied by the same constant. Therefore

$$[\bar{G}]_{k\ell} = \sigma \epsilon_\ell T_\ell^4 A_\ell [\bar{C}^{-1} \bar{F}]_{k\ell} \quad (\text{B39})$$

Because all the surfaces are diffuse, the intensity of the radiant energy on surface k from the emissive power of surface ℓ is equal to the intensity on surface ℓ from the same emissive power on surface k . Therefore

$$\left[\bar{C}^{-1}\bar{F}\right]_{k\ell} = \left[\bar{C}^{-1}\bar{F}\right]_{\ell k} \quad (\text{B40})$$

The net radiant energy absorbed by the k^{th} surface due to potentials on surfaces ℓ and k is the difference between the amount due to a potential on ℓ and the amount due to a potential on k . Then

$$\begin{aligned} A_k q_{k\ell}^r &= \sigma A_k \epsilon_k \epsilon_\ell T_\ell^4 A_\ell \left[\bar{C}^{-1}\bar{F}\right]_{k\ell} - \sigma A_\ell \epsilon_\ell \epsilon_k T_k^4 A_k \left[\bar{C}^{-1}\bar{F}\right]_{\ell k} \\ &= \sigma A_k \epsilon_k \epsilon_\ell A_\ell \left[\bar{C}^{-1}\bar{F}\right]_{k\ell} (T_\ell^4 - T_k^4) \end{aligned} \quad (\text{B41})$$

In terms of the script \mathcal{F} , this is

$$A_k q_{k\ell}^r = \sigma A_\ell \mathcal{F}_{\ell k} (T_\ell^4 - T_k^4) \quad (\text{B42})$$

Then

$$\mathcal{F}_{\ell k} = \epsilon_\ell A_k \epsilon_k \left[\bar{C}^{-1}\bar{F}\right]_{k\ell} \quad (\text{B43})$$

Also

$$A_\ell \mathcal{F}_{\ell k} = A_k \mathcal{F}_{k\ell} \quad (\text{B44})$$

Determination of view factors. - The view factors between nodes in the enclosure were found either by solving analytic expressions or by numerical integration. Reference 18 gives an extensive list of references for finding analytic expressions for view factors. When numerical integration was required, the view factors were obtained by using the computer program described in reference 9.

The desired number of nodes for the shields and struts was not known a priori. Therefore, it was necessary to maintain flexibility in the calculation of view factors. This was done by initial integration only over those variables which were not dependent on the node size. The view factor between i^{th} and j^{th} nodes is given by

$$F_{A_i-A_j} = \frac{1}{A_i} \int_{A_i} \int_{A_j} dF_{dA_i-dA_j} dA_i dA_j \quad (\text{B45})$$

The view factor between differential areas is given by

$$dF_{dA_i-dA_j} = \frac{\cos \beta_i \cos \beta_j}{\pi S^2} \quad (\text{B46})$$

where S is the length of a line connecting the two differential areas and β is the angle between this line and the normal to the surface. For illustrative purposes, let i denote a node on a structural member and let j denote a shield node. Then

$$dA_i = R_{st} d\psi dx \quad (\text{B47})$$

and

$$dA_j = r_{sh} d\theta dr \quad (\text{B48})$$

After the order of integration is rearranged, the view factor equation becomes

$$F_{A_i-A_j} = \frac{R_{st}}{A_i} \int_{x_1}^{x_2} \int_{r_1}^{r_2} \left(r \int_{\psi_1}^{\psi_2} \int_0^{2\pi} \frac{\cos \beta_i \cos \beta_j}{\pi S^2} d\theta d\psi \right) dr dx \quad (B49)$$

The circumferential angle for a structural member node was arbitrarily restricted to multiples of $\pi/2$. The double integration inside the parentheses was solved by using the aforementioned computer program. The variables integrated at this time were not a function of the node size. The resulting expression was then curve fit as a function of the remaining variables of integration, r and x . Each time the node size is chosen, the remaining double integration is performed by using Simpson's Rule.

A similar procedure is used to determine the view factors between annuli on the tank and the planar surfaces. These view factors were initially curve fit as a function of three independent variables. These were the radial position on each surface and the distance between them.

Radial sheet conduction. - In the thermal analysis the radial sheet conduction term, equation (B12), is approximated by considering conduction between adjacent sheet nodes. The radial conduction heat-transfer rate to the i^{th} sheet node is given by

$$q_{sh} = 2\pi t_{sh} \left[\frac{k_{sh} (T_{i+1} - T_i)}{\ln \frac{r_{i+1}}{r_i}} + \frac{k_{sh} (T_{i-1} - T_i)}{\ln \frac{r_i}{r_{i-1}}} \right] \quad (B50)$$

where r is the radius to the center of each node. The thermal conductivity k_{sh} is inside the brackets to indicate that it is evaluated at the average temperature for each pair of nodes.

Effect of the Number of Nodes

The following two figures present temperature profiles as a function of the number of nodes used in the analysis. Figure 44 gives the analytic normalized temperature profile for an all-black fiberglass structural member with no cross radiation. This

profile is for the largest heater-to-tank temperature difference encountered in the testing. Figure 44 gives profiles for different numbers of nodes on each surface. The accuracy of the view factors used was not affected by the number of nodes used. More steps were used in the integration as the number of nodes decreased. These curves show the number of nodes needed to approach nonuniform radiosity in the radiation balance and a differential size for the elements of the structural member. Only a few nodes are needed on the heater, while more are needed on the tank. If the heater had a low instead of high emissivity, more nodes would be needed on the surface of the heater. For the analytic comparisons in this report, each strut was divided into 20 axial segments with one or two nodes per segment.

Figure 45 gives the normalized temperature profiles for two shields as a function of the number of nodes used on the sheet surfaces. The shields were evenly spaced between the heater and the tank. The figure shows that the temperature profile was strongly dependent on the number of shield nodes. The profiles for a single node were significantly different from the profiles when several shield nodes were used. The profiles approached the nonuniform radiosity results as the number of nodes increased. Generally, 12 nodes were used per sheet for the analytic results.

Appropriateness of a Planar Tank Surface

It is desirable to know if the surface of the tank can be replaced analytically by one of a simpler geometry without affecting the temperature profiles for the shields or struts. A simpler geometry would ease the burden of calculating the necessary view factors. Also the curve fits for the differential view factors were difficult to obtain in the area of increasing curvature near the outer edge of the test tank.

Figure 46 gives temperature profiles for both a fiberglass and a titanium strut for two different tank geometries. For each material, there is a curve giving the temperature profile for the tank configuration used in the test. The other profile is for a flat tank surface similar to that of the heater. As expected the effect of tank geometry was confined to the cold end of the strut. However, since the heat-transfer rate to the tank is of prime importance, it was necessary to use the more complicated geometry of the actual tank test.

APPENDIX C

SHIELD ANALYSIS BASED ON DIRECTIONAL PROPERTIES

This analysis describes the corrections for the shield temperatures based on directionally dependent emissivities. These corrections were applied to the analysis presented in appendix B. To apply the corrections, the change in sheet temperature due to directional properties was found for a simpler configuration. Applying the directional analysis to the actual configuration was prohibitive from the standpoint of computer time. This same percentage change was then applied to the sheet temperatures found by using the analysis of appendix B. This simpler model uses emissivities found from electromagnetic theory.

Description of Analysis

A detailed description of the analysis leading to expressions for emissivity as a function of the angle to the normal is given in reference 19. The directional emissivity for an unpolarized beam is given by

$$\epsilon(\beta) = 2\eta \cos \beta \left[\frac{1}{(\eta^2 + \kappa^2) \cos^2 \beta + 2\eta \cos \beta + 1} + \frac{1}{\cos^2 \beta + 2\eta \cos \beta + \eta^2 + \kappa^2} \right] \quad (C1)$$

The two optical constants in this equation, η and κ , are both functions of the wavelength of the energy in the beam. Reference 20 gives the relationship of both η and κ as a function of wavelength for aluminum, silver, and gold. This relationship is based on Drude's single-electron theory. This reference also discusses the wavelength range of applicability for this theory. Reference 11 gives the value of the optical constants of evaporated aluminum measured in a vacuum at a wavelength of 12 micrometers.

The model used to investigate the effects of directional properties is a cylinder with closed ends. The ends of the cylinder represent either two shield sheets or a sheet and the heater. The wall of the cylinder represents either the ring between the sheets of a shield or the surrounding between shields. When the end is used to simulate the heater or the wall is used to simulate the surrounding, these surfaces have an emissivity of unity.

Figure 47 shows the geometry of the cylinder. The ends are surfaces 1 and 2. And the wall is surface 3. These numbers are used as subscripts in the following equations. The interchange factors for surface 1 are found by a ray-tracing technique and a Monte Carlo procedure. All rays originate on surface 1. Reference 21 describes the procedure used in the Monte Carlo analysis. The initial position of the ray is determined by a random number

$$r = R \sqrt{\mathcal{R}(r)} \quad (\text{C2})$$

where $\mathcal{R}(r)$ is a random number with a range of 0 to 1. The square root of $\mathcal{R}(r)$ is used so that there is uniform distribution with respect to the surface area of the disk. Because of symmetry, the coordinates are arranged so that the ray originates at a point on the x-coordinate axis. Two angles, θ and β , must be specified to determine the direction of the outgoing ray. In the circumferential direction the probability of a ray leaving at a given angle is the same for all angles. Then

$$\theta = 2\pi \mathcal{R}(\theta) \quad (\text{C3})$$

It can be assumed that each ray transports the same amount of energy. Then the distribution function for the angle to the normal must be weighted in favor of the angles corresponding to higher emissivities. Alternately, it can be assumed that the rays are uniformly distributed through each solid angle. Then each ray must be weighted to account for the emissivity at each angle. Both approaches were taken to see that each resulted in the same answers with similar confidence levels.

To obtain the distribution function for the rays at constant wavelength, it is necessary to integrate the emissivity over the range of solid angles:

$$\epsilon^*(\beta_1) = \frac{1}{\pi} \int \epsilon(\beta) \cos \beta \, d\omega \quad (\text{C4})$$

where

$$d\omega = \sin \beta \, d\beta \, d\theta \quad (C5)$$

This substitution, along with the integration for θ , yields

$$\epsilon^*(\beta_1) = 2 \int_0^{\beta_1} \epsilon(\beta) \cos \beta \sin \beta \, d\beta \quad (C6)$$

If all the rays carry the same amount of energy, the integration for ϵ^* is found by substituting equation (C1) into (C6). Carrying out the integration results in

$$\begin{aligned} \epsilon^*(\beta_1) = & \left\{ \frac{4\eta}{\eta^2 + \kappa^2} - \frac{4\eta^2}{\eta^2 + \kappa^2} \ln(1 + 2\eta + \eta^2 + \kappa^2) \right. \\ & - \frac{4\eta(\kappa^2 - \eta^2)}{\kappa(\eta^2 + \kappa^2)^2} \left[\tan^{-1} \left(\frac{\eta^2 + \kappa^2 + \eta}{\kappa} \right) - \tan^{-1} \left(\frac{\eta}{\kappa} \right) \right] \\ & + 4\eta - 4\eta^2 \ln \left(\frac{\eta^2 + \kappa^2 + 2\eta + 1}{\eta^2 + \kappa^2} \right) \\ & \left. + \frac{4\eta(\eta^2 - \kappa^2)}{\kappa} \left[\tan^{-1} \left(\frac{1 + \eta}{\kappa} \right) - \tan^{-1} \left(\frac{\eta}{\kappa} \right) \right] \right\}_0^{\beta_1} \quad (C7) \end{aligned}$$

Let $f[\epsilon^*(\beta_1)/\epsilon^*(\pi/2)]$ denote the functional relationship for the cumulative probability distribution. Typically, this would be a polynomial fit to points found by solving equation (C7). The angle with the normal for the ray is found by choosing a random number

$$\beta = f[\mathcal{R}(\beta)] \quad (C8)$$

If each ray is weighted to account for the emissivity at the angle to the normal, the distribution is that for a diffuse blackbody. Then

$$\mathcal{R}(\beta) = \frac{\int_0^\beta \cos \beta \sin \beta d\beta}{\int_0^{\pi/2} \cos \beta \sin \beta d\beta} \quad (C9)$$

or

$$\beta = \sin^{-1} [\sqrt{\mathcal{R}(\beta)}] \quad (C10)$$

Once the position and direction of a ray have been determined, it is necessary to determine where it intercepts the wall or edge of the cylinder. Because of symmetry, the coordinate system is adjusted for each ray so that it has no initial component along the y-axis. Then

$$P_1 [P_1(x), P_1(y), P_1(z)] = P_1(r, 0, 0) \quad (C11)$$

The ray leaving surface 1 will strike either the other end (surface 2) or the wall (surface 3). Taking each case separately clarifies the explanation.

Case I - ray strikes wall. - Point 3 lies on the wall. Therefore,

$$R^2 = P_3(x)^2 + P_3(y)^2 \quad (C12)$$

and

$$P_3(x) = P_1(x) + h \tan \beta \cos \theta \quad (\text{C13})$$

$$P_3(y) = P_1(y) + h \tan \beta \sin \theta \quad (\text{C14})$$

The term $P_1(y)$ is included because only initially does the ray have no component along this axis. After it has been reflected off the other surfaces, it can have a nonzero y-component when it is reflected off surface 1. The height at which the ray strikes the wall is found by substituting equations (C13) and (C14) into equation (C12) and solving for h . The normal to surface 3 is given by

$$\bar{N}_3 = [-P_3(x), -P_3(y), 0] \quad (\text{C15})$$

Let \bar{V} be the vector connecting points 1 and 3. Then

$$\bar{V}_1 = P_1(x) - P_3(x), P_1(y) - P_3(y), P_1(z) - P_3(z) \quad (\text{C16})$$

where

$$P_3(z) = h$$

Let \bar{W}_3 be the vector perpendicular to \bar{N}_3 and \bar{V}_1 . Then

$$\bar{W}_3 = \bar{V}_1 \times \bar{N}_3 \quad (\text{C17})$$

Also, let \bar{U}_3 be a vector perpendicular to \bar{N}_3 and \bar{W}_3 . Then

$$\bar{U}_3 = \bar{W}_3 \times \bar{N}_3 \quad (C18)$$

The angle between \bar{V}_1 and \bar{N}_3 is the angle to the normal of surface 3. Then

$$\cos \beta_3 = \frac{\bar{V}_1 \cdot \bar{N}_3}{|\bar{V}_1| |\bar{N}_3|} \quad (C19)$$

To determine if the ray is absorbed on surface 3, a random number \mathcal{R} is chosen. If \mathcal{R} is greater than $\epsilon^*(\beta_3)$, the ray is reflected. If, instead, the ray is absorbed, the counter for surface 3 is incremented and a new ray is chosen on surface 1.

The electromagnetic theory assumes specular reflections. Therefore, the direction of the reflected ray is determined by the direction of the incident ray. Let \bar{V}_3 be the outgoing ray. Both \bar{V}_3 and \bar{V}_1 have the same components in the normal direction. The components of \bar{V}_3 are the negative of \bar{V}_1 in the other direction:

$$\bar{V}_3 = \left[\frac{\bar{V}_1 \cdot \bar{N}_3}{|\bar{N}_3|}, \frac{-\bar{V}_1 \cdot \bar{U}_3}{|\bar{U}_3|}, 0 \right] \quad (C20)$$

where \bar{V}_3 has no component in the \bar{W}_3 direction because \bar{W}_3 is perpendicular to \bar{V}_1 .

If the ray with direction \bar{V}_3 strikes the wall of the cylinder, the governing equations are similar to those for a ray which has just left surface 1 striking the wall.

If the ray strikes surface 2, it is similar to a ray leaving surface 1 and striking surface 2.

Case II - ray strikes other end. - The point of impact for the ray is a distance ℓ from surface 1. Then

$$P_2(x) = P_1(x) + \ell \tan \beta \cos \theta \quad (\text{C21})$$

$$P_2(y) = P_1(y) + \ell \tan \beta \sin \theta \quad (\text{C22})$$

$$P_2(z) = \ell \quad (\text{C23})$$

and

$$\bar{V}_1 = [P_1(x) - P_2(x), P_1(y) - P_2(y), P_1(z) - P_2(z)] \quad (\text{C24})$$

Since the normal to surface 2 is in the minus z-direction,

$$\cos \beta_2 = \frac{\bar{V}_1(z)}{|\bar{V}_1|} \quad (\text{C25})$$

To determine if the ray is absorbed on surface 2, a random number \mathcal{R} is chosen. If \mathcal{R} is greater than $\epsilon^*(\beta_2)$, the ray is reflected. If, instead, the ray is absorbed, the counter for surface 2 is incremented. Then a new ray is chosen on surface 1.

If the ray is reflected, the components of the reflected ray \bar{V}_3 are

$$\bar{V}_3 = [-\bar{V}_1(x), -\bar{V}_1(y), -\bar{V}_1(z)] \quad (\text{C26})$$

If the ray from surface 2 strikes the wall, it is similar to a ray from surface 1 striking the wall. If a ray from either surface 2 or surface 3 strikes surface 1, the equations used are similar to those for a ray striking surface 2.

This procedure was carried out for a large number of rays. The interchange factors were found by dividing the summation counters for each surface by the total number of rays. When each ray was weighted by the emissivity corresponding to its initial direction, the script \mathcal{F} interchange factors were calculated directly. Otherwise, the results had to be multiplied by the hemispherical emissivity of surface 1. Most interchange factors were calculated to have a maximum error of 5 percent. This was done at a 95 percent confidence level. The confidence level was found by measuring the variance for a series of trials.

Application of Equations

The equations presented in the preceding section are for a single wavelength. Thermal energy is transported over a band of wavelengths. For each temperature there is a wavelength which corresponds to the maximum amount of energy per wavelength. Figure 48 gives the effect of directional properties on the radiation connectors between surfaces. The results are plotted as a function of wavelength. Also shown on the abscissa is the temperature for which the emissive power at the corresponding wavelength is a maximum. The ordinate axis is the ratio of the connector when directional properties are assumed to the connector when the hemispherical emissivities are used. Both the numerator and denominator are for specularly reflecting surfaces. The effect of directional properties is shown to be relatively independent of wavelength. This does not mean that the radiation connectors are independent of wavelength. Both the numerator and denominator are strong functions of wavelength. The curves on this figure are for the connectors needed in the analysis of the shields.

Figure 49 is a comparison of the shield temperatures for different surface assumptions. These results are for uniform-temperature shields. Part (a) is for evenly spaced shields, and part (b) is for closely spaced shields. Because properties have been taken independent of temperature, the ordinate scale can be normalized with respect to the heater temperature. In each case the profiles are for uniform-temperature sheets. The directional property results were found by using the analysis given in this appendix. In the specular analysis, equation (C1) for the emissivity of the surface was replaced by the hemispherical value. The diffuse analysis used the same hemispherical emissivity as the analysis presented in appendix B. The uniform radiosity results used only a single node per shield. Both the diffuse sheet temperatures and the specular sheet temperatures were in close agreement. The primary cause of the change in sheet

temperatures was the use of directional properties.

The corrections applied to the sheet temperatures were found by ratioing the directional sheet temperatures to the diffuse sheet temperatures. This same ratio was applied to the temperatures calculated by the equations given in appendix B for the test configuration. This procedure yielded the analytic shield profiles. These temperatures were calculated in the absence of structural members. Including 12 titanium structural members did not significantly change the results.

APPENDIX D

ANALYSIS FOR GASEOUS CONDUCTION

The shield tests with liquid hydrogen in the test tank unfortunately were conducted with a relatively high pressure inside the shroud. This pressure was of the order of 10^{-5} torr and resulted in significant heat transfer to the test tank by gaseous conduction. The pressure inside the shroud was such that the flow was in the transition regime between free molecular and continuum flow. This appendix contains a discussion of the equations used to predict the effects of gaseous conduction. The results of this analysis showed that pressures of the order of 10^{-7} torr are needed to ensure that gaseous conduction does not significantly influence either the sheet temperatures for the colder shield or the heat-transfer rate.

Free molecular flow occurs when the molecules leaving one surface are very likely to reach a second surface before interacting with other molecules. The mean free path in terms of viscosity, density, and mean velocity is given by Kennard in reference 22 as

$$L = \frac{\mu}{0.499 \rho \bar{v}} \quad (D1)$$

The mean velocity is given by the equation

$$\bar{v} = 2 \left(\frac{2R_u T}{\pi M} \right)^{1/2} \quad (D2)$$

The density for an ideal gas is given by

$$\rho = \frac{pM}{R_u T} \quad (D3)$$

Combining equations yields

$$L = \frac{\mu}{0.998 \rho} \sqrt{\frac{\pi R_u T}{2M}} \quad (D4)$$

Perlmutter in reference 23 investigated the heat transfer between infinite parallel plates. The analysis in this reference covered the transition regime between free molecular and continuum flow. The analysis showed that when the Knudson number L/d was greater than 10, the heat-transfer rate approached that for free molecular flow. Also, when the Knudson number was less than 0.01, the heat-transfer rate approached that for continuum flow.

Free Molecular Flow

The following analysis for free molecular flow is taken from the work of Corruccini in reference 24. Consider two surfaces numbered 1 and 2. The energy of the molecules leaving surface 1 is E_1 , and the energy of those leaving surface 2 is E_2 . The accommodation coefficient a is the fraction of molecules which leave a surface with energy corresponding to the temperature of the surface. If a is zero, there is no change in the energy of the molecules as they rebound from the surface. If a is 1, all the molecules rebound from the surface with an energy corresponding to the temperature of the surface. It is assumed that molecules reflect from the surfaces in a diffuse fashion so that their distribution follows Lambert's cosine law.

There are two cases of interest which are considered herein. The first case is for two concentric surfaces. This case could correspond to an isolated object inside the cryoshroud. In the second case there are more than two surfaces. In the test configuration the heater is one surface, the test tank is another, and the cryoshroud is a third.

Case I - two surfaces. - Let surface 1 be the smaller of two concentric surfaces. This surface could correspond to an isolated structural member inside the chamber. Then $F_{1-2} = 1$ and $F_{2-1} = A_1/A_2$. The view factor symbol is used because molecules originating on a diffuse surface have the same distribution as diffuse radiant energy.

The incident stream of molecules on surface 1 arrive with a temperature corresponding to surface 2. The energy of the rebounding molecules is a function of the accommodation coefficient:

$$E'_2 - E'_1 = a_1(E'_2 - E_1) \quad (D5)$$

The prime symbols refer to the actual energy of the molecules. The unprimed symbols refer to the energy of the molecules corresponding to the temperature of the surface. The incident stream of molecules on surface 2 comes from both surface 1 and surface 2. Some molecules from surface 2 bypass surface 1. The equation for the total energy per unit time out of surface 2 is

$$\left[E_1' A_1 + E_2' \left(1 - \frac{A_1}{A_2} \right) A_2 - E_2' A_2 \right] = a_2 \left[E_1' A_1 + E_2' \left(1 - \frac{A_1}{A_2} \right) A_2 - E_2' A_2 \right] \quad (D6)$$

The energy transferred by gaseous conduction is the difference in the energy of the actual incoming stream and the energy of the actual outgoing stream. On surface 1 this is

$$q_1^c = E_2' - E_1' = a(E_2 - E_1) \quad (D7)$$

where

$$a = \frac{a_1 a_2}{a_2 + a_1 \left(1 - \frac{A_1}{A_2} \right)} \quad (D8)$$

Corruccini in reference 24 gives suggested values of the accommodation coefficients for hydrogen, helium, and air as a function of surface temperature. For hydrogen at room temperature the value is 0.3. And for the same gas at liquid-hydrogen temperature the value is 1.0.

The difference in the ideal energy of the two streams is proportional to the temperature difference between the surfaces:

$$E_2 - E_1 = s \left(c_v + \frac{R_u}{2M} \right) (T_2 - T_1) \quad (D9)$$

The term $\frac{1}{2} R_u$ arises because the average translational energy of the molecules striking the walls is $\frac{4}{3}$ that of the average for all the molecules between the surfaces. Also, the specific heat of gases due to translational energy is $3R_u/2M$.

Kennard in reference 22 derives the value of the mass of molecules passing a unit area per unit time s as

$$s = \frac{1}{4} \rho' \bar{v}' \quad (D10)$$

The primed symbols are used because s is determined by the actual energy of the molecules crossing the area. The density is the sum of the individual densities

$$\rho' = \rho'_1 + \rho'_2 \quad (D11)$$

If the areas of the surfaces were equal, the mass rates would be the same for each stream. As the ratio of A_2 to A_1 increases, there will be more molecules corresponding to the temperature of surface 2 in the space between surfaces. Then

$$s = \frac{1}{4} \rho'_1 \bar{v}'_1 \left(\frac{A_2}{A_1} + 1 \right) \quad (D12)$$

or

$$s = \frac{1}{4} \rho'_2 \bar{v}'_2 \left(\frac{A_1}{A_2} + 1 \right) \quad (D13)$$

The velocity is related to the temperature by equation (D2). Combining equations results in the equation for the gas temperature as

$$\frac{1}{\sqrt{T'}} = \left(\frac{A_1}{A_1 + A_2} \right) \frac{1}{\sqrt{T'_1}} + \left(\frac{A_2}{A_1 + A_2} \right) \frac{1}{\sqrt{T'_2}} \quad (D14)$$

The energies in equations (D5) and (D6) are proportional to the temperatures. These equations are solved to give the actual temperatures for each stream in terms of the surface temperatures:

$$T'_1 = \frac{a_1 T_1 \left[(1 - a_2) \frac{A_1}{A_2} + a_2 \right] + a_2 (1 - a_1) T_2}{a_2 + a_1 (1 - a_2) \frac{A_1}{A_2}} \quad (D15)$$

$$T'_2 = \frac{a_1 T_1 (1 - a_2) \frac{A_1}{A_2} + a_2 T_2}{a_2 + a_1 (1 - a_2) \frac{A_1}{A_2}} \quad (D16)$$

Substituting pressure and temperature for density and velocity in equation (D10) results in

$$s = \rho \sqrt{\frac{M}{2 \pi R_u T'}} \quad (D17)$$

Also

$$c_v = \frac{R_u}{M(\gamma - 1)} \quad (D18)$$

Then the heat-transfer equation can be expressed as

$$q_1^c = \frac{ap}{2} \sqrt{\frac{R_u}{2 \pi M T'}} \left[\left(\frac{\gamma + 1}{\gamma - 1} \right) (T_2 - T_2) \right] \quad (D19)$$

Case II - three or more surfaces. - The analysis for gaseous conduction for several surfaces at different temperatures is begun by writing the equations for the energies as a function of the accommodation coefficient. The equations for the surfaces are

$$\left. \begin{aligned}
 E_1' F_{1-1} A_1 + E_2' F_{2-1} A_2 + \dots + E_m' F_{m-1} A_m - E_1' A_1 &= a_1 (E_1' F_{1-1} A_1 + E_2' F_{2-1} A_2 + \dots + E_m' F_{m-1} A_m - E_1' A_1) \\
 E_1' F_{1-2} A_1 + E_2' F_{2-2} A_2 + \dots + E_m' F_{m-2} A_m - E_2' A_2 &= a_2 (E_1' F_{1-2} A_1 + E_2' F_{2-2} A_2 + \dots + E_m' F_{m-2} A_m - E_2' A_2) \\
 \vdots & \\
 E_1' F_{1-m} A_1 + E_2' F_{2-m} A_2 + \dots + E_m' F_{m-m} A_m - E_m' A_m &= a_m (E_1' F_{1-m} A_1 + E_2' F_{2-m} A_2 + \dots + E_m' F_{m-m} A_m - E_m' A_m)
 \end{aligned} \right\}$$

(D20)

The energies are proportional to the temperatures. Therefore, T is substituted for E in the preceding equation. Then the stream temperatures are found. The matrix equation uses the reciprocity relationship for view factors, and both sides of the equation are divided by the area. The equation is

$$\bar{C} \bar{T}' = \bar{T} \tag{D21}$$

where

$$[\bar{C}]_{ij} = \frac{\delta_{ij} - F_{i-j}(1 - a_i)}{a_i}$$

$$[\bar{T}']_j = T'_j$$

and

$$[\bar{T}]_i = T_i$$

The inverse equation is solved to determine the stream temperatures

$$\overline{T}' = \overline{C}^{-1} \overline{T} \quad (D22)$$

The energy difference is found by using equations (D7) and (D19) to give

$$E'_2 - E'_1 = \frac{p}{2} \sqrt{\frac{R_u}{2\pi M T'}} \left(\frac{\gamma + 1}{\gamma - 1} \right) (T'_2 - T'_1) \quad (D23)$$

For more than two surfaces the expression for the stream temperature T' would be very complicated. Corruccini in reference 24 suggests using the temperature at the same location as the pressure transducer for T' .

The heat-transfer rate to the i^{th} surface by gaseous conduction is then

$$q_i^c = \frac{p}{2} \sqrt{\frac{R_u}{2\pi M T'}} \left(\frac{\gamma + 1}{\gamma - 1} \right) \sum_j^m F_{i-j} (T'_j - T'_i) \quad (D24)$$

Heat Transfer in Transition Region

Unfortunately, the flow regime in the test configuration was in the transition region between free molecular and continuum flow. Perlmutter in reference 23 analyzes a similar problem in which he shows that applying the equations for free molecular flow near the continuum region overpredicts the heat-transfer rate by an order of magnitude.

The heat transfer between two infinite plates for the transition region is analyzed by Kennard in reference 22. The heat-transfer rate at the wall per unit area and time is

$$E'_2 - E'_1 = k \frac{\partial T}{\partial N} \quad (D25)$$

Half of this conduction energy E'_2 is carried in the incident stream and half of it E'_1 is carried in the reflected stream. This energy is in excess of the molecular energy. The energy of the molecules which would rebound from the wall at a temperature corresponding to the wall temperature is

$$E_1 = s \left(c_v + \frac{1}{2} \frac{R_u}{M} \right) T_1 \quad (D26)$$

Substitution into equation (D5) yields

$$k \frac{\partial T}{\partial N} = a_1 \left[\frac{k}{2} \frac{\partial T}{\partial N} + s \left(c_v + \frac{1}{2} \frac{R_u}{M} \right) (T'_2 - T_1) \right] \quad (D27)$$

Even if both accommodation coefficients are unity, T'_2 is not necessarily equal to T_2 . The temperature T'_2 is that of the gas. Near the continuum region T'_2 approaches T_1 , and near the free molecular flow region T'_2 approaches T_2 .

In the transition region there is a discontinuity in the temperature profile near the wall. The distance over which the discontinuity persists is the jump distance and is denoted by ξ . It is defined by the equation

$$T'_2 - T_1 = \xi_1 \frac{\partial T}{\partial N} \quad (D28)$$

Combining equations (D17), (D18), (D27), and (D28) yields

$$\xi_1 = \frac{k(2 - a_1)(\gamma - 1)}{pa_1(\gamma + 1)} \sqrt{\frac{2\pi MT}{R_u}} \quad (D29)$$

At the other surface the equation for the jump distance is

$$\xi_2 = \frac{k(2 - a_2)(\gamma - 1)}{pa_2(\gamma + 1)} \sqrt{\frac{2\pi MT}{R_u}} \quad (D30)$$

The temperature used under the radical should be measured at the same location as the pressure. The equivalent distance between surfaces is the actual distance d plus the sum of both distances caused by temperature discontinuities. Therefore, the heat-transfer rate is expressed as

$$q_1^c = \frac{k(T_2 - T_1)}{d + \xi_1 + \xi_2} \quad (D31)$$

When there were only two surfaces at different temperatures, equation (D31) was used. In the continuum region $d \gg \xi$, and equation (D31) becomes the ordinary conduction equation. In the free molecular flow region, $\xi \gg d$ and the results of equation (D31) approach those of equation (D19) with $A_1 = A_2$. When there were more than two surfaces at different temperatures, the procedure was more complicated. First, the heat-transfer terms were calculated for all the pairs of surfaces by using equation (D24) which assumes free molecular flow. Next these terms were modified by a ratio to account for the fact that flow was in the transition region. This ratio was formed by taking the results of equation (D31) and dividing them by the results of equation (D19) for each pair of surfaces.

REFERENCES

1. Hall, C. F.; Nothwang, G. J.; and Hornby, H.: Solar Probes - A Feasibility Study. Aerospace Eng., vol. 21, no. 5, May 1962, pp. 23-30.
2. Lundholm, J. G., Jr.; Prohaska, E. S.; Hoyer, S.; and Averell, J.: A Close Approach Solar Probe Design Feasibility and Mission Study. Paper 64-496, AIAA, June 1964.
3. Smolak, George R.; Knoll, Richard H.; and Wallner, Lewis E.: Analysis of Thermal-Protection Systems for Space-Vehicle Cryogenic-Propellant Tanks. NASA TR R-130, 1962.
4. Knoll, Richard H.; and Bartoo, Edward R.: Experimental Studies on Shadow Shields for Thermal Protection of Cryogenic Tanks in Space. NASA TN D-4887, 1968.
5. Boyle, Robert J.; and Knoll, Richard H.: Thermal Analysis of Shadow Shields and Structural Members in a Vacuum. NASA TN D-4876, 1968.
6. Stochl, R. J.; and Boyle, R. J.: An Analytical and Experimental Evaluation of Shadow Shields and Their Support Members. Presented at the Cryogenic Engineering Conference, Boulder, Colo., Aug. 9-11, 1972, paper C-2.
7. Anon.: Design and Fabrication of Shadow Shield Systems for Thermal Protection of Cryogenic Propellants. Rep. ADL-C-69507, Arthur D. Little, Inc. (NASA CR-72595), Nov. 27, 1969.
8. Wiebelt, John A.: Engineering Radiation Heat Transfer. Holt Rinehart & Winston, Inc., 1966.
9. Dummer, R. S.; and Breckenridge, W. T., Jr.: Radiation Configuration Factors Program. Rep. ERR-AN-224, General Dynamics/Astronautics, Feb. 1963.
10. Lewis, D. R.; Gaski, J. D.; and Thompson, L. R.: Chrysler Improved Numerical Differencing Analyzer for Third Generation Computers. Rep. TN AP-67-287, Chrysler Corp. (NASA CR-99595), Oct. 20, 1967.
11. Garbuny, Max: Optical Physics. Academic Press, 1965.
12. Hertz, J.; and Knowles, D.: Survey of Thermal Properties of Selected Materials. Rep. ZZL-65-008, AR-504-1-553, General Dynamics/Convair, Feb. 15, 1965.
13. Touloukian, Y. S.: Recommended Values of the Thermophysical Properties of Eight Alloys, Their Major Constituents and Oxides. AEC-NASA Tech. Brief 67-10062, Mar. 1967.

14. Haskins, James F.; Campbell, Malcolm D.; Hertz, Julius; and Percy, Joseph L.: Thermophysical Properties of Plastic Materials and Composites to Liquid Hydrogen Temperature (-423° F). General Dynamics/Astronautics, (ML-TDR-64-33, AD-601337), June 1964.
15. Clark, A. F.; Childs, G. E.; and Wallace, G. H.: Electrical Resistivity of Some Engineering Alloys at Low Temperatures. *Cryogenics*, vol. 10, no. 4, Aug. 1970, pp. 295-305.
16. Cunnington, G. R.; Keller, C. W.; and Bell, G. A.: Thermal Performance of Multilayer Insulations. Rep. LMSC-A903316, Lockheed Missiles & Space Co. (NASA CR-72605), Apr. 20, 1971.
17. Viskanta, Raymond; Schornhorst, James R.; and Toor, Jaswant S.: Analysis and Experiment of Radiant Heat Exchange Between Simply Arranged Surfaces. Purdue Univ. (AFFDL-TR-67-94, AD-655335), June 1967.
18. Howell, John R.; and Siegel, Robert: Thermal Radiation Heat Transfer. Vol. 2. NASA SP-164, 1969.
19. Siegel, Robert; and Howell, John R.: Thermal Radiation Heat Transfer. Vol. 1. NASA SP-164, 1968.
20. Bennett, H. E.; and Bennett, J. M.: Validity of the Drude Theory for Silver, Gold, and Aluminum in the Infrared. Optical Properties and Electronic Structure of Metals and Alloys. F. Abeles, ed., John Wiley & Sons, Inc., 1966, pp. 175-188.
21. Howell, John R.: Calculation of Radiant Heat Exchange by the Monte Carlo Method. Presented at the ASME Winter Annual Meeting, Chicago, Ill., Nov. 7-11, 1965.
22. Kennard, Earle H.: Kinetic Theory of Gases, with an Introduction to Statistical Mechanics. McGraw-Hill Book Co., Inc., 1938.
23. Perlmutter, Morris: Analysis of Couette Flow and Heat Transfer Between Parallel Plates Enclosing Rarefied Gas by Monte Carlo. *Rarefied Gas Dynamics*, Vol. 1, C. L. Brundin, ed., Academic Press, 1967, pp. 455-480.
24. Corruccini, R. J.: Gaseous Heat Conduction at Low Pressures and Temperatures. *Vacuum*, vols. 7 & 8, Apr. 1959, pp. 19-29.

TABLE I. - INDEPENDENT VARIABLES FOR ANALYISS

Radius, cm (in.):	
Heater	67.3 (26.5)
Tank	
Major	61.0 (24)
Minor	22.4 (8.8)
Shield	
Sheet	67.3 (26.5)
Ring	63.5 (25)
Strut	2.22 (0.875)
Inside of cryoshroud	122 (48)
Baffle edge	67.3 (26.5)
Spacing (along centerline), cm (in.):	
Overall	31.8 (12.5)
Heater to shield	
Even spacing	9.21 (3.625)
Close spacing	1.27 (0.5)
Between shields	9.21 (3.625)
Between sheets of a shield	1.91 (0.75)
Shield to tank	
Even spacing	9.53 (3.75)
Close spacing	17.46 (6.875)
Thickness, cm (in.):	
Strut	0.038 (0.015)
Strut insulation	0.318 (0.125)
Sheet material	0.003 (0.001)
Aluminized coating	8.0×10^{-6} (3.16×10^{-6})
Baffle	1.91 (0.75)
Strut length, cm (in.)	56.0 (22.05)
Area, cm ² (in. ²):	
Tank	
Bottom	1.423×10^4 (2.206×10^3)
Total	3.722×10^4 (5.769×10^3)
Shroud (total effective)	1.067×10^5 (1.655×10^4)

TABLE I. - Concluded. INDEPENDENT VARIABLES FOR ANALYSIS

Emissivity:	
Aluminized surfaces	0 (0)
	$1.019 \times 10^{-4} T$ ($5.660 \times 10^{-5} T$)
Painted surfaces	0.8561 (0.8561)
	$3.107 \times 10^{-4} T$ ($1.726 \times 10^{-4} T$)
	$1.659 \times 10^{-7} T^2$ ($5.119 \times 10^{-8} T^2$)
	$-4.860 \times 10^{-10} T^3$ ($-8.333 \times 10^{-11} T^3$)
Inside of ring	0 (0)
	$2.380 \times 10^{-4} T$ ($1.322 \times 10^{-4} T$)
Thermal conductivity, W/cm-K (Btu/hr-in. -°R):	
Fiberglass	4.687×10^{-4} (2.257×10^{-3})
	$3.136 \times 10^{-5} T$ ($8.391 \times 10^{-5} T$)
	$-9.870 \times 10^{-8} T^2$ ($-1.476 \times 10^{-7} T^2$)
	$1.116 \times 10^{-10} T^3$ ($9.218 \times 10^{-11} T^3$)
Titanium	1.896×10^{-3} (9.133×10^{-3})
	$4.326 \times 10^{-4} T$ ($1.158 \times 10^{-3} T$)
	$-9.970 \times 10^{-7} T^2$ ($-1.482 \times 10^{-6} T^2$)
	$1.025 \times 10^{-9} T^3$ ($8.462 \times 10^{-10} T^3$)
Aluminum	1.229×10^{-2} (5.917×10^{-2})
	$9.386 \times 10^{-3} T$ ($2.511 \times 10^{-2} T$)
	$-2.900 \times 10^{-5} T^2$ ($-4.311 \times 10^{-5} T^2$)
	$3.677 \times 10^{-8} T^3$ ($3.037 \times 10^{-8} T^3$)
Strut insulation	-2.790×10^{-8} (-1.344×10^{-7})
	$7.540 \times 10^{-9} T$ ($2.017 \times 10^{-8} T$)
	$-5.117 \times 10^{-11} T^2$ ($-7.606 \times 10^{-11} T^2$)
	$2.152 \times 10^{-13} T^3$ ($1.770 \times 10^{-13} T^3$)
Temperature, K (°R):	
Heater (nominal)	
High	389 (700)
Room	294 (530)
Tank	
Hydrogen	20.8 (37.5)
Nitrogen	77.8 (140)
Shroud and baffles	27.8 (50)

TABLE II. - DESCRIPTION OF TEST CONFIGURATION

Test	Primary purpose	Strut configuration	Shield spacing	Heater temperature, T_H , K($^{\circ}$ R)	Tank fluid	Pressure, torr
1a 1b 7a 7b	Strut temperatures and heat-transfer rates without shields	Six titanium and six fiberglass struts (one of each kind insulated)	None	^a 289(520) ^b 389(700) ^a 296(533) ^a 388(698)	Liquid nitrogen Liquid nitrogen Liquid hydrogen Liquid hydrogen	1.0×10^{-6} 4.0×10^{-7} 4.0×10^{-8} 8.0×10^{-9}
2 3a 3b	Strut and shield temperatures with two shields present	Eleven titanium and one fiberglass strut	Even	^a 297(534) ^a 297(535) ^b 388(699)	Liquid hydrogen Liquid nitrogen Liquid nitrogen	6.4×10^{-6} 2.2×10^{-7} 2.2×10^{-7}
4	Shield spacing and thermocouple covering	Eleven titanium and one fiberglass strut	Close	^b 389(700)	Liquid nitrogen	6.0×10^{-9}
5a 5b	Effect of strut - shield ring insert material	Eleven titanium and one fiberglass strut	Close	^a 296(533) ^b 388(699)	Liquid nitrogen Liquid nitrogen	2.0×10^{-7} 2.5×10^{-7}
6a 6b 6c 6d	Fiberglass strut profiles with shields and low heat-transfer rates	Twelve fiberglass struts	Even	^a 296(533) ^b 387(697) ^a 296(533) ^b 388(698)	Liquid hydrogen Liquid hydrogen Liquid nitrogen Liquid nitrogen	2.0×10^{-5} 1.2×10^{-6} 2.5×10^{-7} 3.3×10^{-7}

^aRoom-temperature heater.

^bHigh-temperature heater.

TABLE III. - AVERAGE EXPERIMENTAL STRUT TEMPERATURE RATIOS FOR NO-SHIELD TESTS

(a) Body of strut

Thermo-couple location from tank end of strut		Strut type											
		Half black				All black				Insulated			
		Test											
		1a	1b	7a	7b	1a	1b	7a	7b	1a	1b	7a	7b
		Heater temperature, T_H , K ($^{\circ}$ R)											
		289 (520)	389 (700)	296 (533)	388 (698)	289 (520)	389 (700)	296 (533)	388 (698)	289 (520)	389 (700)	296 (533)	388 (698)
		Tank temperature, T_T , K ($^{\circ}$ R)											
cm	in.	78 (141)	78 (141)	21 (37)	21 (37)	78 (141)	78 (141)	21 (37)	21 (37)	78 (141)	78 (141)	21 (37)	21 (37)
Average experimental strut temperature ratio, $(T - T_T)/(T_H - T_T)$													
Strut material, titanium													
1.3	0.5	0.079	0.159	0.177	0.238	----	----	----	----	----	----	----	----
3.8	1.5	.132	.225	.225	.277	0.246	0.342	0.361	0.412	----	----	----	----
6.4	2.5	.173	.272	.288	.355	----	----	----	----	0.183	0.227	0.261	0.273
8.9	3.5	.202	.301	.345	.401	----	----	----	----	----	----	----	----
11.4	4.5	.231	.326	----	----	----	----	----	----	----	----	----	----
22.4	8.8	.300	.364	.455	.461	.509	.543	.625	.612	----	----	----	----
28.7	11.3	----	----	----	----	----	----	----	----	.598	.594	.621	.610
36.3	14.3	----	----	----	----	----	----	----	----	----	----	----	----
38.4	15.1	.443	.459	.555	.542	.556	.573	.665	.651	----	----	----	----
40.1	15.8	.453	.453	.566	.535	----	----	----	----	----	----	----	----
46.5	18.3	.629	.620	.663	.626	----	----	----	----	----	----	----	----
49.0	19.3	.668	.627	.688	.636	----	----	----	----	----	----	----	----
51.6	20.3	.776	.731	.758	.709	.721	.702	.737	.694	.950	.907	.900	.868
52.8	20.8	.837	.789	.786	.726	----	----	----	----	----	----	----	----
Strut material, fiberglass													
1.3	0.5	0.050	0.111	0.115	0.154	----	----	----	----	----	----	----	----
3.8	1.5	.134	.230	.249	.306	0.247	0.338	0.339	0.388	----	----	----	----
6.4	2.5	.267	.354	.404	.441	----	----	----	----	0.194	0.240	0.280	0.287
8.9	3.5	.237	.315	.415	.425	----	----	----	----	----	----	----	----
11.4	4.5	.278	.350	.449	.449	----	----	----	----	----	----	----	----
22.4	8.8	.304	.375	.478	.485	.463	.496	.597	.586	----	----	----	----
28.7	11.3	.367	.442	.529	.551	----	----	----	----	.580	.579	.632	.619
36.3	14.3	.354	.401	.508	.506	----	----	----	----	----	----	----	----
38.4	15.1	.401	.446	.533	.540	.531	.561	.637	.629	----	----	----	----
40.1	15.8	.419	.464	.546	.541	----	----	----	----	----	----	----	----
46.5	18.3	.503	.531	.598	.584	----	----	----	----	----	----	----	----
49.0	19.3	.553	.551	.614	.579	----	----	----	----	----	----	----	----
51.6	20.3	.663	.657	.688	.665	.647	.661	.714	.696	.915	.873	.863	.804
52.8	20.8	.762	.733	.728	.681	----	----	----	----	----	----	----	----

TABLE III. - Concluded. AVERAGE EXPERIMENTAL STRUT
TEMPERATURE RATIOS FOR NO-SHIELD TESTS

(b) For outward side of outer insulation layer

Thermo- couple location from tank end of strut		Strut material							
		Titanium				Fiberglass			
		Test							
		1a	1b	7a	7b	1a	1b	7a	7b
		Heater temperature, T_H , K ($^{\circ}$ R)							
		289 (520)	389 (700)	296 (533)	388 (698)	289 (520)	389 (700)	296 (533)	388 (698)
		Tank temperature, T_T , K ($^{\circ}$ R)							
cm	in.	78 (141)	78 (141)	21 (37)	21 (37)	78 (141)	78 (141)	21 (37)	21 (37)
		Average experimental strut temperature ratio, T/T_H							
3.8	1.5	0.549	0.553	0.504	0.539	0.517	0.531	0.485	0.502
22.4	8.8	.616	.589	.602	.593	.617	.585	.601	.583
38.4	15.1	.674	.623	.680	.662	.678	.633	.651	.600
49.0	19.3	.785	.735	.773	.743	.774	.717	.730	.659

TABLE IV. - HEAT-TRANSFER RATES FOR NO-SHIELD TESTS

(a) SI units

Test	Heater	Tank	Experimental			Analytic, gray			Analytic, nongray		
			Total	Conductive	Radiative	Total	Conductive	Radiative	Total	Conductive	Radiative
			Heat-transfer rate, W								
7a	296	21	12.4	1.1	11.3	4.8	0.8	4.0	12.8	0.8	12.0
7b	388	21	43.9	2.5	41.4	13.9	1.6	12.3	45.5	1.6	43.9
1a	289	78	2.3	0.7	1.6	5.7	0.6	5.1	11.3	0.6	10.7
1b	389	78	45.6	2.1	43.5	19.3	1.4	17.9	46.4	1.4	45.0

(b) U.S. customary units

Test	Heater	Tank	Experimental			Analytic, gray			Analytic, nongray		
			Total	Conductive	Radiative	Total	Conductive	Radiative	Total	Conductive	Radiative
			Heat-transfer rate, Btu/hr								
7a	533	37	42.4	3.8	38.6	16.2	2.7	13.5	43.6	2.7	40.9
7b	698	37	150.0	8.5	141.5	47.6	5.5	42.1	155.3	5.5	149.8
1a	520	141	7.9	2.4	5.4	19.5	1.9	17.6	38.3	1.9	36.4
1b	700	141	155.6	7.2	148.4	65.9	4.8	61.1	158.4	4.8	153.6

TABLE V. - AVERAGE EXPERIMENTAL STRUT TEMPERATURE RATIOS FOR SHIELD TESTS

(a) Strut material, titanium

Thermo- couple location from tank end of strut	Strut type																		
	Half black					All black													
	Shield spacing					Shield spacing													
Even					Close					Even					Close				
Test																			
Heater temperature, T_H , K ($^{\circ}$ R)																			
2		3a	3b	4	5a	5b	5a	2	3a	3b	4	5b	5a						
297 (534)	297 (535)	388 (699)	389 (700)	388 (699)	296 (533)	297 (534)	297 (535)	297 (535)	388 (699)	389 (700)	388 (699)	296 (533)	296 (533)						
Tank temperature, T_T , K ($^{\circ}$ R)																			
21 (37)		78 (141)	78 (141)	78 (141)	78 (141)	78 (141)	21 (37)	78 (141)	78 (141)	78 (141)	78 (141)	78 (141)	78 (141)						
1.3	0.5	-0.002	-0.027	-0.017	-0.019	-0.021	-0.032	-0.002	-0.032	-0.020	-0.023	-0.026	-0.040						
3.8	1.5	.025	.032	.018	.022	.022	.036	.002	.036	.020	.023	.026	.040						
6.4	2.5	.068	.024	.010	.016	.017	.031	.002	.031	.020	.023	.026	.040						
8.9	3.5	.082	.028	.011	.020	.020	.038	.002	.038	.020	.023	.026	.040						
11.4	4.5	.113	.023	.005	.014	.012	.028	.002	.028	.012	.016	.016	.043						
22.4	8.8	.177	.008	.030	.005	.012	.005	.163	.013	.012	.016	.016	.043						
28.7	11.3	.261	.104	.106	.066	.079	.088	.002	.088	.012	.016	.016	.043						
36.3	14.3	.336	---	---	---	---	---	.002	.088	.012	.016	.016	.043						
38.4	15.1	.381	.233	.241	.136	.165	.184	.363	.207	.218	.116	.114	.107						
40.1	15.8	.413	.276	.284	.149	.168	.181	.002	.002	.002	.002	.002	.002						
46.5	18.3	.608	.507	.543	.312	.319	.342	.002	.002	.002	.002	.002	.002						
49.0	19.3	.690	.655	.634	.389	.376	.389	.002	.002	.002	.002	.002	.002						
51.6	20.3	.756	.692	.691	.468	.499	.539	.756	.698	.690	.440	.454	.470						
52.8	20.8	.799	.751	.744	.559	.554	.566	.002	.002	.002	.002	.002	.002						
Average experimental strut temperature ratio, $(T - T_T)/(T_H - T_T)$																			

(b) Strut material, fiberglass

Thermo-couple location from tank end of strut		Strut type															
		Half black						All black									
		Shield spacing															
		Even						Close						Even			
		Test															
		6a	6b	6c	6d	2	3a	3b	4	5a	5b	5c	6a	6b	6c	6d	
		Heater temperature, T _H , K (°R)															
		296 (533)	387 (697)	296 (533)	388 (698)	297 (534)	388 (699)	389 (700)	388 (699)	296 (533)	296 (533)	296 (533)	387 (697)	296 (533)	388 (698)		
cm	in.	21 (37)	78 (141)	78 (141)	78 (141)	21 (37)	78 (141)	78 (141)	78 (141)	78 (141)	78 (141)	21 (37)	21 (37)	78 (141)	78 (141)		
		Tank temperature, T _T , K (°R)															
		21 (37)	78 (141)	78 (141)	78 (141)	21 (37)	78 (141)	78 (141)	78 (141)	78 (141)	78 (141)	21 (37)	21 (37)	78 (141)	78 (141)		
		Average experimental strut temperature ratio, (T - T _T)/(T _H - T _T)															
1.3	0.5	0.048	0.036	0.020	0.014	-0.002	-0.046	-0.031	-0.034	-0.034	-0.034	-0.051	0.045	0.038	-0.002		
3.8	1.5	0.048	0.040	.001	.000	-0.002	-0.046	-0.031	-0.034	-0.034	-0.034	-0.051	0.045	0.038	-0.002		
6.4	2.5	.062	.055	-0.021	-0.013	-0.002	-0.046	-0.031	-0.034	-0.034	-0.034	-0.051	0.029	0.034	-0.059		
8.9	3.5	.066	.066	-.049	-.030	-0.002	-0.046	-0.031	-0.034	-0.034	-0.034	-0.051	.053	.056	-.049		
11.4	4.5	.069	.070	-.049	-.031	.020	-.110	-.071	-.080	-.071	-.071	-.109	.058	.064	-.089		
22.4	8.8	.114	.120	-.047	-.022	.107	-.089	-.044	-.080	-.074	-.074	-.125	.103	.104	-.060		
28.7	11.3	.172	.177	.013	.026	.206	.028	.050	.018	.020	.020	.057	.157	.157	-.003		
36.3	14.3	.264	.260	.100	.118	.310	.150	.160	.049	.038	.038	.004	---	---	---		
38.4	15.1	.301	.297	.137	.160	---	---	---	---	---	---	---	.290	.294	.118		
40.1	15.8	.336	.326	.174	.194	.357	.195	.214	.119	.086	.086	.054	.320	.325	.154		
46.5	18.3	.555	.578	.511	.497	.550	.436	.503	.204	.202	.202	.185	.532	.550	.423		
49.0	19.3	.675	.677	.590	.618	---	---	---	---	---	---	---	.789	.805	.730		
51.6	20.3	.741	.742	.684	.694	.716	.647	.660	.392	.401	.401	.408	.773	.761	.709		
52.8	20.8	.778	.770	.722	.726	---	---	---	---	---	---	---	.805	.795	.751		

TABLE VI. - AVERAGE EXPERIMENTAL SHIELD AND RING TEMPERATURE RATIOS

Shield	Sheet	Radius	Shield spacing																	
			Close						Even											
			Strut configuration																	
			Twelve fiberglass																	
			Test																	
			Heater temperature, T _H , K (°R)																	
			296 (533)		297 (534)		297 (535)		388 (699)		296 (533)		387 (697)		296 (533)		388 (698)			
			4	5a	5b	2	3a	3b	3c	6a	6b	6c								
			Side of sheet																	
			Average experimental shield and ring temperature ratio, T _i /T _H																	
Warm	Warm	0	Inside	Outside	Inside	Outside	Inside	Outside	Inside	Outside	Inside	Outside	Inside	Outside	Inside	Outside	Inside	Outside		
			a ₀ .924	a ₀ .920	a ₀ .926	a ₀ .927	a ₀ .923	a ₀ .927	a ₀ .934	a ₀ .899	a ₀ .899	a ₀ .911	a ₀ .908	a ₀ .898	a ₀ .911	a ₀ .896	a ₀ .902	a ₀ .915	a ₀ .898	a ₀ .907
Cold	Cold	0	Inside	Outside	Inside	Outside	Inside	Outside	Inside	Outside	Inside	Outside	Inside	Outside	Inside	Outside	Inside	Outside		
			a ₀ .923	a ₀ .930	a ₀ .948	a ₀ .947	a ₀ .920	a ₀ .946	a ₀ .886	a ₀ .886	a ₀ .906	a ₀ .889	a ₀ .916	a ₀ .882	a ₀ .882	a ₀ .887	a ₀ .900	a ₀ .887	a ₀ .896	a ₀ .890
Shield ring ^c	Shield ring ^b	0	Inside	Outside	Inside	Outside	Inside	Outside	Inside	Outside	Inside	Outside	Inside	Outside	Inside	Outside	Inside	Outside		
			a ₀ .911	a ₀ .924	a ₀ .911	a ₀ .937	a ₀ .909	a ₀ .942	a ₀ .855	a ₀ .854	a ₀ .867	a ₀ .861	a ₀ .868	a ₀ .851	a ₀ .851	a ₀ .862	a ₀ .866	a ₀ .860	a ₀ .864	a ₀ .864
Shield ring ^c	Shield ring ^b	66.0 26	Inside	Outside	Inside	Outside	Inside	Outside	Inside	Outside	Inside	Outside	Inside	Outside	Inside	Outside	Inside	Outside		
			a ₀ .621	a ₀ .621	a ₀ .666	a ₀ .666	a ₀ .677	a ₀ .666	a ₀ .655	a ₀ .655	a ₀ .644	a ₀ .644	a ₀ .641	a ₀ .630	a ₀ .630	a ₀ .625	a ₀ .625	a ₀ .618	a ₀ .618	a ₀ .619
Shield ring ^c	Shield ring ^b	66.0 26	Inside	Outside	Inside	Outside	Inside	Outside	Inside	Outside	Inside	Outside	Inside	Outside	Inside	Outside	Inside	Outside		
			a ₀ .390	a ₀ .390	a ₀ .389	a ₀ .389	a ₀ .390	a ₀ .393	a ₀ .371	a ₀ .371	a ₀ .369	a ₀ .369	a ₀ .391	a ₀ .367	a ₀ .367	a ₀ .374	a ₀ .364	a ₀ .364	a ₀ .376	
Shield ring ^c	Shield ring ^b	25.4 10	Inside	Outside	Inside	Outside	Inside	Outside	Inside	Outside	Inside	Outside	Inside	Outside	Inside	Outside	Inside	Outside		
			a ₀ .390	a ₀ .390	a ₀ .399	a ₀ .399	a ₀ .387	a ₀ .387	a ₀ .365	a ₀ .365	a ₀ .356	a ₀ .356	a ₀ .379	a ₀ .349	a ₀ .349	a ₀ .363	a ₀ .357	a ₀ .357	a ₀ .366	
Shield ring ^c	Shield ring ^b	45.7 18	Inside	Outside	Inside	Outside	Inside	Outside	Inside	Outside	Inside	Outside	Inside	Outside	Inside	Outside	Inside	Outside		
			a ₀ .372	a ₀ .372	a ₀ .384	a ₀ .384	a ₀ .382	a ₀ .382	a ₀ .353	a ₀ .353	a ₀ .356	a ₀ .356	a ₀ .362	a ₀ .326	a ₀ .326	a ₀ .344	a ₀ .343	a ₀ .343	a ₀ .346	
Shield ring ^c	Shield ring ^b	58.4 23	Inside	Outside	Inside	Outside	Inside	Outside	Inside	Outside	Inside	Outside	Inside	Outside	Inside	Outside	Inside	Outside		
			a ₀ .268	a ₀ .268	a ₀ .265	a ₀ .269	a ₀ .282	a ₀ .274	a ₀ .261	a ₀ .264	a ₀ .269	a ₀ .266	a ₀ .263	a ₀ .198	a ₀ .205	a ₀ .255	a ₀ .249	a ₀ .274	a ₀ .282	
Shield ring ^c	Shield ring ^b	58.4 23	Inside	Outside	Inside	Outside	Inside	Outside	Inside	Outside	Inside	Outside	Inside	Outside	Inside	Outside	Inside	Outside		
			a ₀ .266	a ₀ .274	a ₀ .261	a ₀ .275	a ₀ .291	a ₀ .284	a ₀ .270	a ₀ .272	a ₀ .281	a ₀ .265	a ₀ .271	a ₀ .193	a ₀ .207	a ₀ .252	a ₀ .248	a ₀ .275	a ₀ .281	
Shield ring ^c	Shield ring ^b	66.0 26	Inside	Outside	Inside	Outside	Inside	Outside	Inside	Outside	Inside	Outside	Inside	Outside	Inside	Outside	Inside	Outside		
			a ₀ .266	a ₀ .274	a ₀ .266	a ₀ .271	a ₀ .301	a ₀ .284	a ₀ .295	a ₀ .287	a ₀ .298	a ₀ .267	a ₀ .274	a ₀ .196	a ₀ .207	a ₀ .249	a ₀ .289	a ₀ .256	a ₀ .257	
Shield ring ^c	Shield ring ^b	66.0 26	Inside	Outside	Inside	Outside	Inside	Outside	Inside	Outside	Inside	Outside	Inside	Outside	Inside	Outside	Inside	Outside		
			a ₀ .319	a ₀ .319	a ₀ .322	a ₀ .322	a ₀ .363	a ₀ .327	a ₀ .327	a ₀ .338	a ₀ .338	a ₀ .297	a ₀ .297	a ₀ .272	a ₀ .272	a ₀ .257	a ₀ .257	a ₀ .309	a ₀ .309	

^aData corrected for effect of tape covering for thermocouples.
^bFor warm shield.
^cFor cold shield.

TABLE VII. - CORRECTION FOR TAPE-
COVERED THERMOCOUPLES

Shield	Sheet	Surface	Temperature correction, $T_{\text{corrected}}/T_{\text{uncorrected}}$
Warm	Warm	Outside	0.976
		Inside	1.026
	Cold	Inside	---
		Outside	1.082
Cold	Warm	Outside	0.981
		Inside	---
	Cold	Inside	0.963
		Outside	1.049

TABLE VIII. - HEAT-TRANSFER RATES FOR SHIELD TESTS

(a) SI units

Test	Test fluid	Total measured	Calculated						Analytic - strut conduction
			Strut conduction	Gaseous conduction		Radiation	Unaccounted ^a		
				$P/\sqrt{T} = \text{Constant}$	$P = \text{Constant}$		$P/\sqrt{T} = \text{Constant}$	$P = \text{Constant}$	
Heat-transfer rate, W									
2	Liquid hydrogen	0.27	0.06	0.12	0.32	0.003	0.09	-0.11	0.13
3a	Liquid nitrogen	-1.03	- .14	- .01	---	- .13	- .75	----	- .06
3b	↓	- .99	- .11	- .01	---	↓	- .74	----	- .03
4		- .63	- .12	- .0003	---		- .38	----	- .05
5b		- .61	- .14	- .01	---		- .33	----	- .06
6a		Liquid hydrogen	.41	.01	.28		.67	.003	.12
6a'	Liquid hydrogen	.63	.01	.75	1.56	.003	- .13	- .94	.003
6b	Liquid hydrogen	.15	.01	.03	.08	.003	.11	.06	.06
6c	Liquid nitrogen	- .55	.0003	- .01	---	- .13	- .41	----	- .04
6d	Liquid nitrogen	- .50	.001	- .01	---	- .13	- .36	----	- .03

(b) U.S. customary units

Test	Test fluid	Total measured	Calculated						Analytic - strut conduction
			Strut conduction	Gaseous conduction		Radiation	Unaccounted ^a		
				$P/\sqrt{T} = \text{Constant}$	$P = \text{Constant}$		$P/\sqrt{T} = \text{Constant}$	$P = \text{Constant}$	
Heat-transfer rate, Btu/hr									
2	Liquid hydrogen	0.91	0.19	0.42	1.10	0.01	0.29	-0.39	0.45
3a	Liquid nitrogen	-3.50	- .47	- .03	---	- .44	-2.56	----	- .20
3b	↓	-3.38	- .38	- .03	---	↓	-2.53	----	- .11
4		-2.15	- .41	- .001	---		-1.30	----	- .18
5b		-2.09	- .47	- .03	---		-1.15	----	- .20
6a		Liquid hydrogen	1.41	.04	.97		2.27	.01	.39
6a'	Liquid hydrogen	2.14	.03	2.55	5.31	.01	.35	-3.21	.01
6b	Liquid hydrogen	.50	.04	.10	.28	.01	.35	.17	.19
6c	Liquid nitrogen	-1.87	.001	- .03	---	- .44	-1.40	----	- .12
6d	Liquid nitrogen	-1.71	.002	- .04	---	- .44	-1.23	----	- .10

^aUnaccounted rate is total measured minus sum of strut and gaseous conduction and radiation.

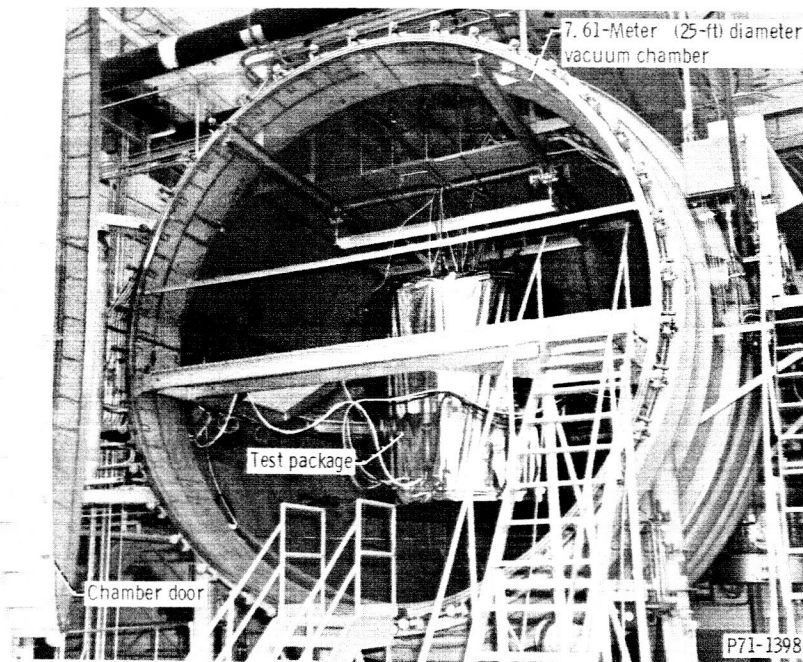


Figure 1. - Vacuum chamber.

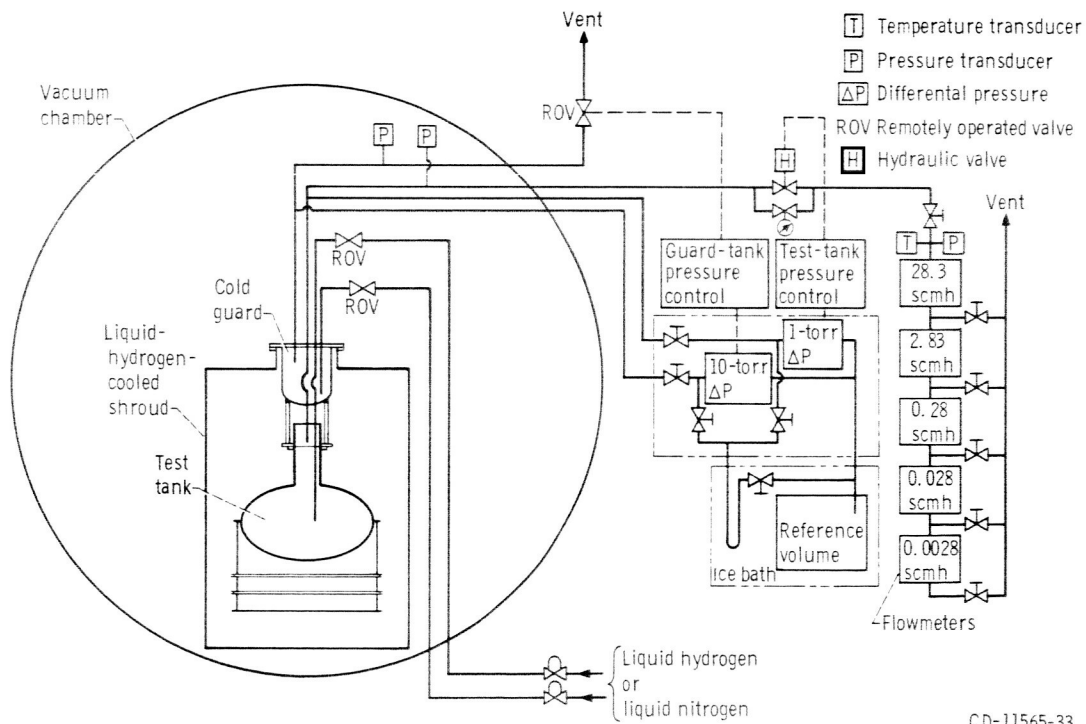
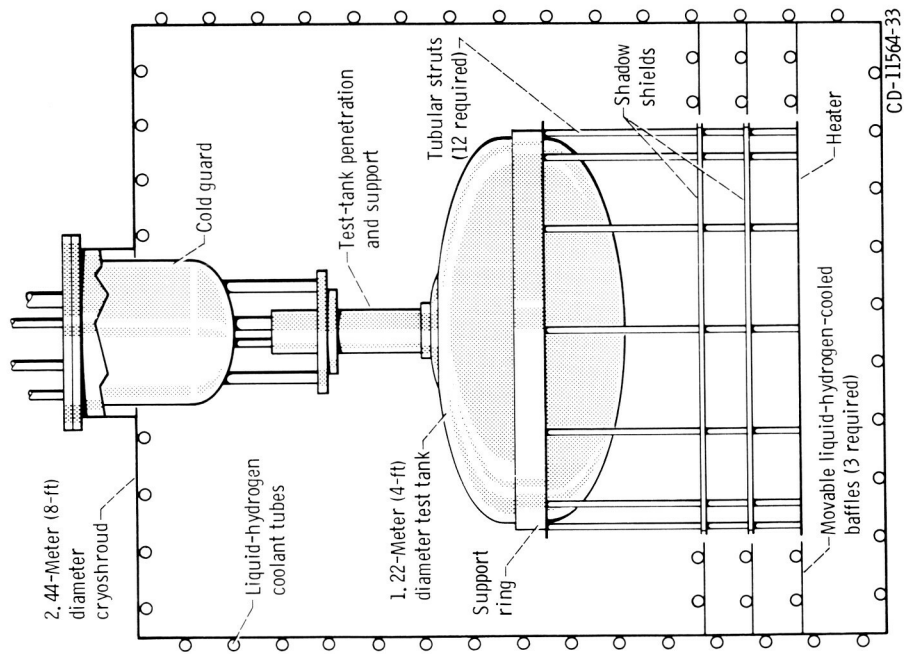
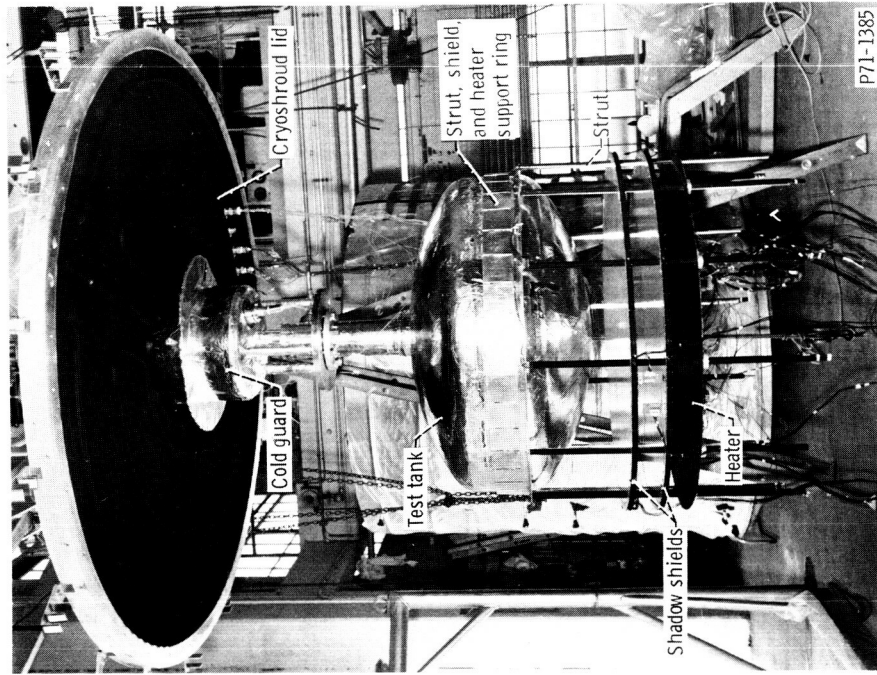


Figure 2. - General schematic of facility

CD-11565-33



(a) General test schematic.



(b) Two-shield test configuration.

Figure 3. - Experimental setup.

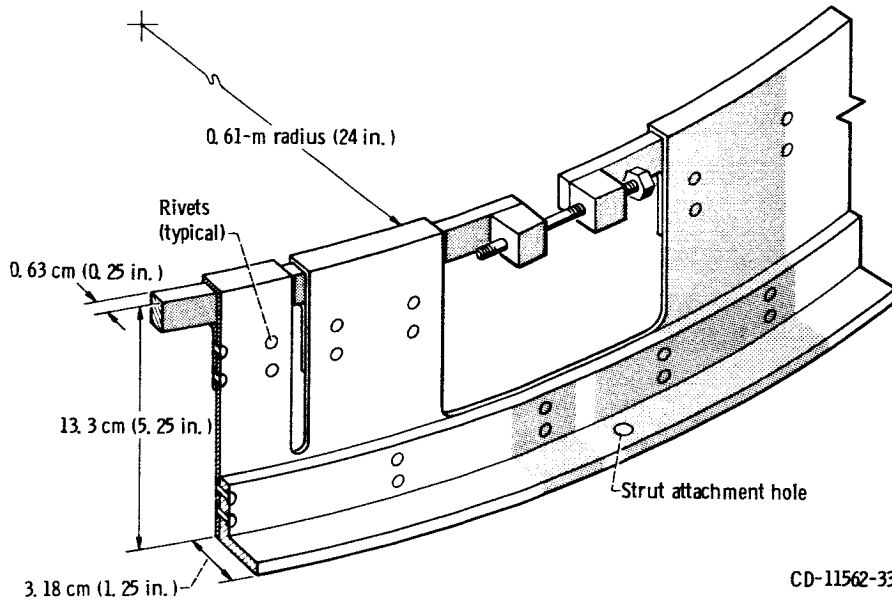
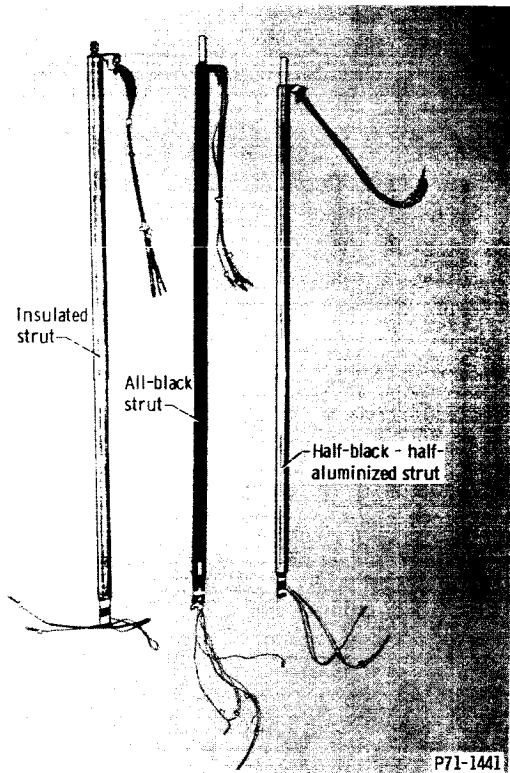
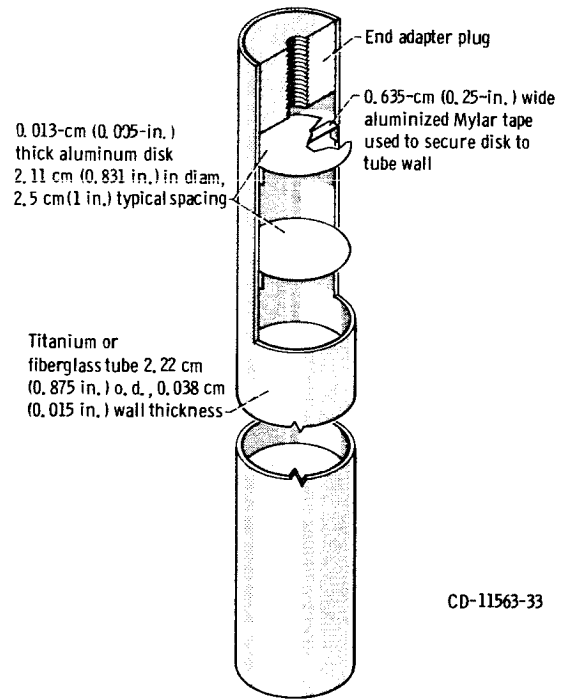


Figure 4. - Support ring detail.



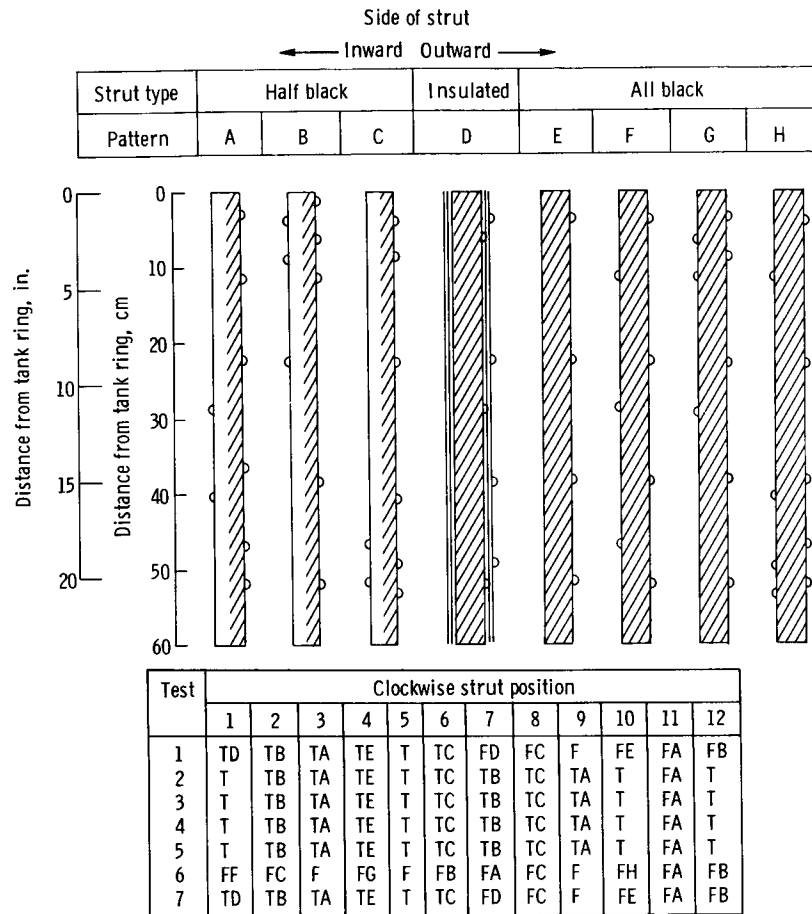
(a) Strut surface coating configurations.



(b) Internal strut details.

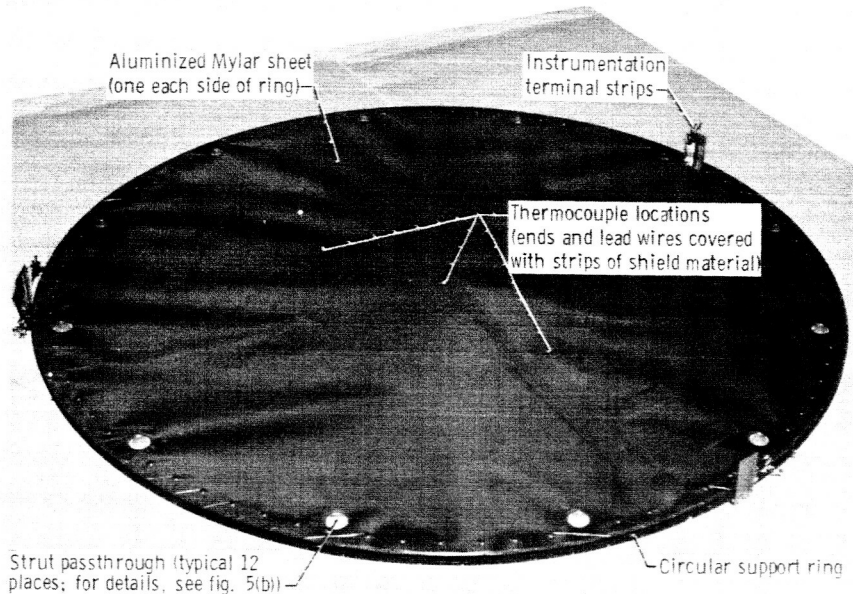
Figure 5. - Strut details.

CD-11563-33



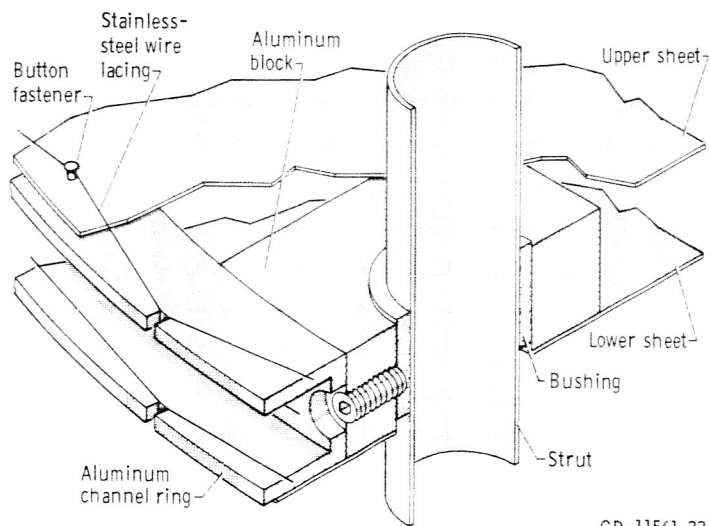
(c) Strut instrumentation and circumferential location for each test. T, titanium strut; F, fiberglass strut; A to H, instrumentation pattern; blank, no instrumentation on strut.

Figure 5. - Concluded.



P71-1410

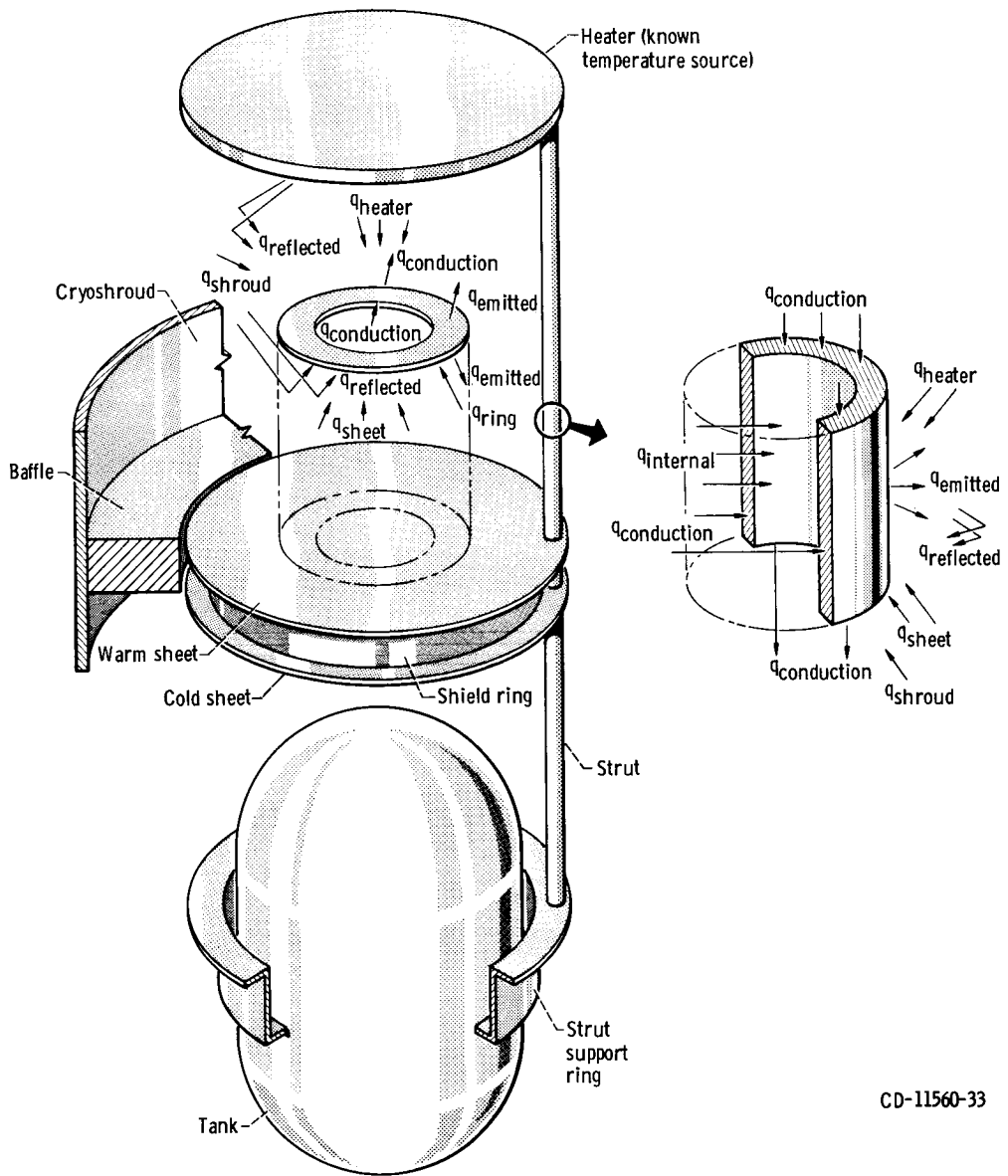
(a) Shadow shield.



CD-11561-33

(b) Strut-to-shield connection.

Figure 6. - Shield details.



CD-11560-33

Figure 7. - Schematic of analytic configuration showing heat-transfer terms to sheet and strut nodes.

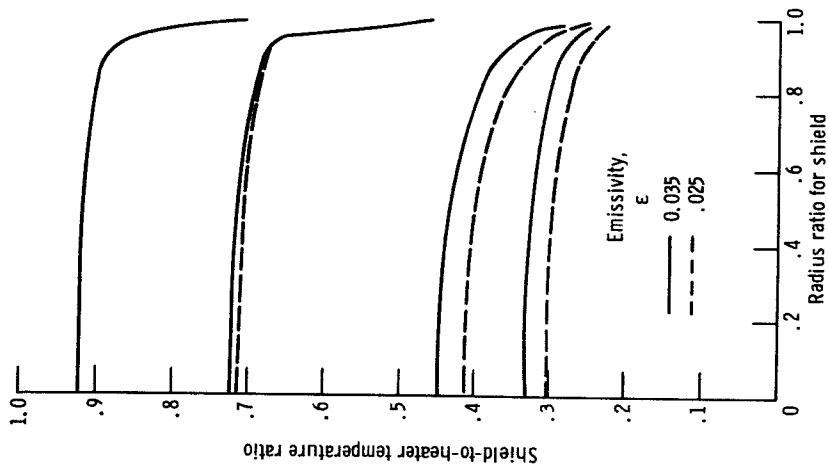


Figure 9. - Effect of emissivity level for test configuration. Evenly spaced shields; sheets disconnected from rings; tank-to-heater temperature ratio, 0.2

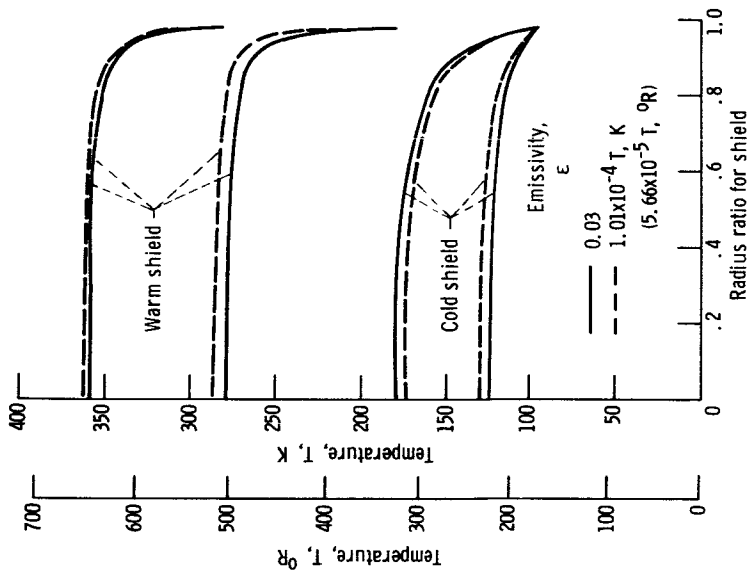


Figure 8. - Effect of emissivity assumptions on sheet temperatures. Evenly spaced shields; sheets disconnected from rings; tank-to-heater temperature ratio, 0.2

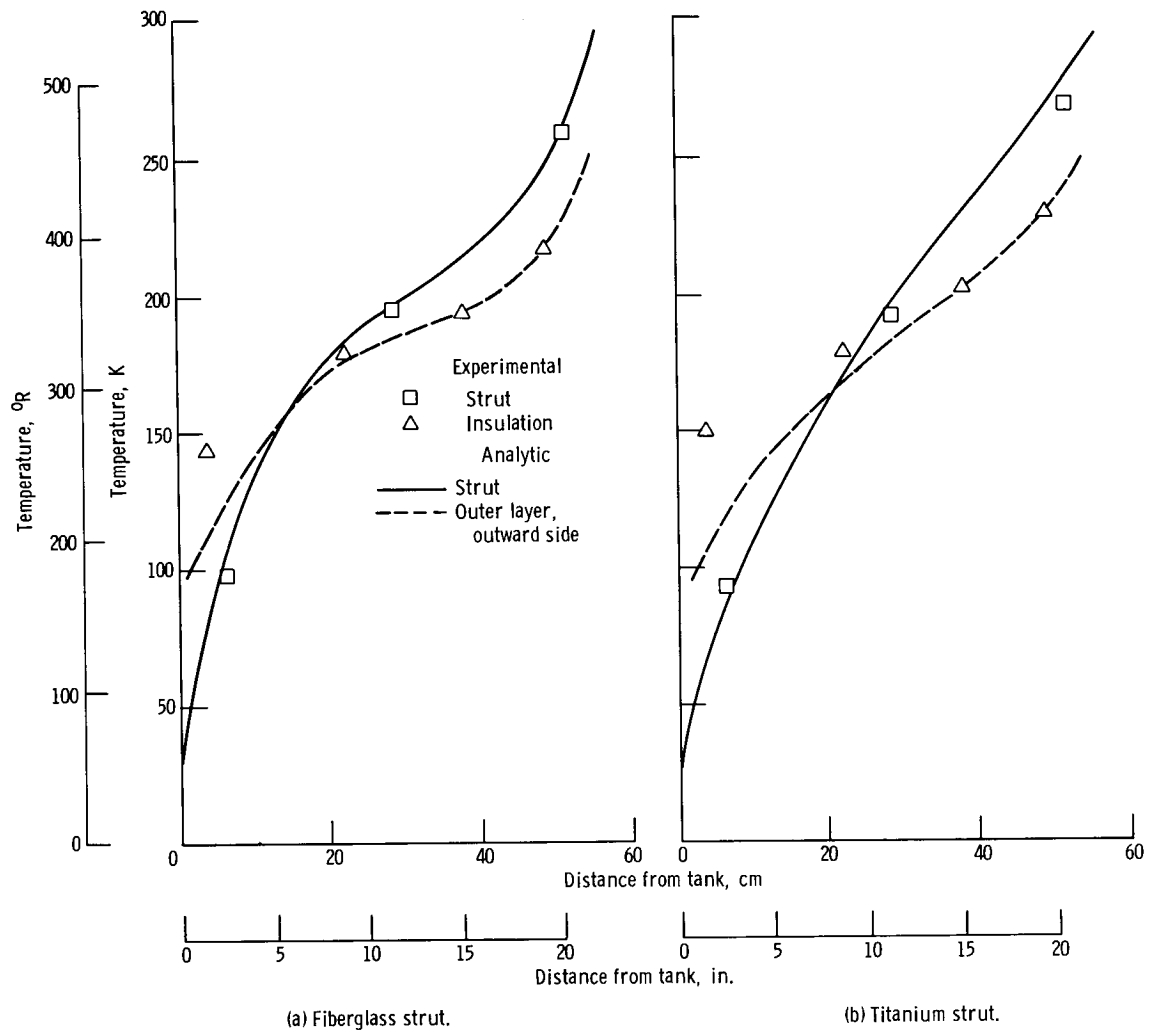
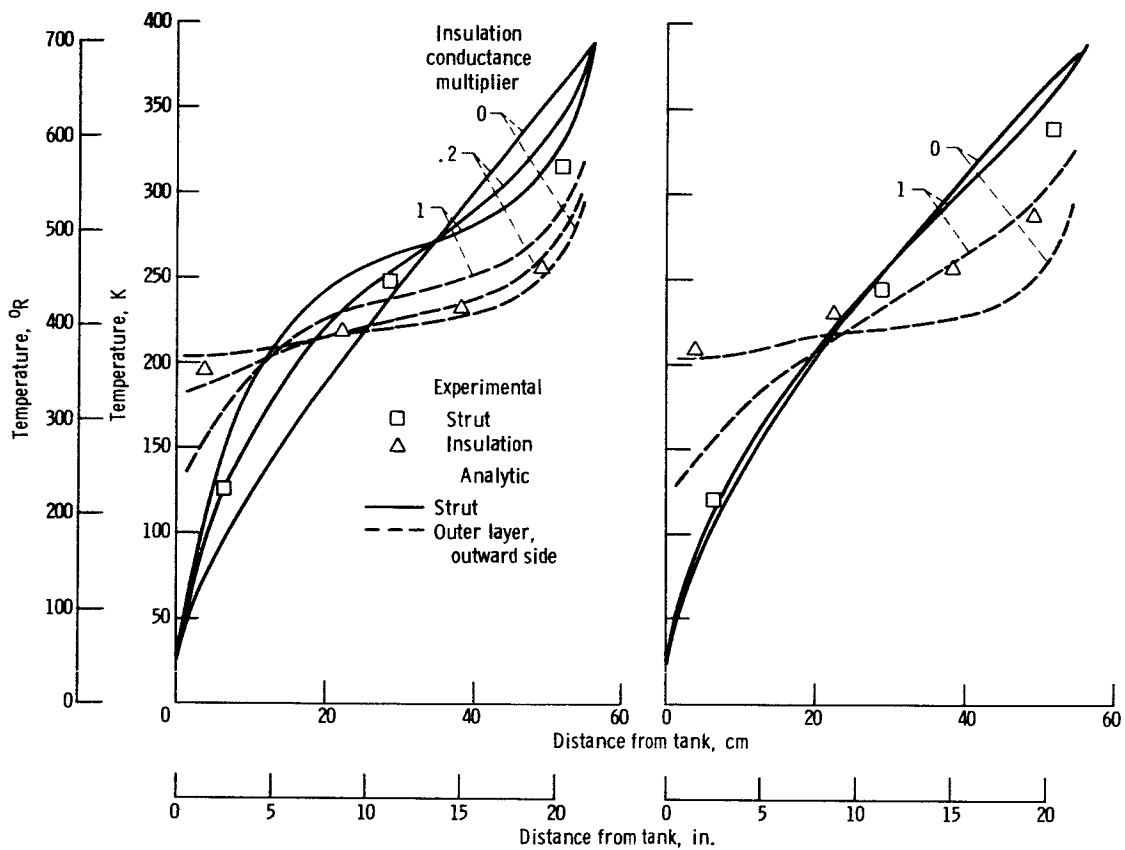


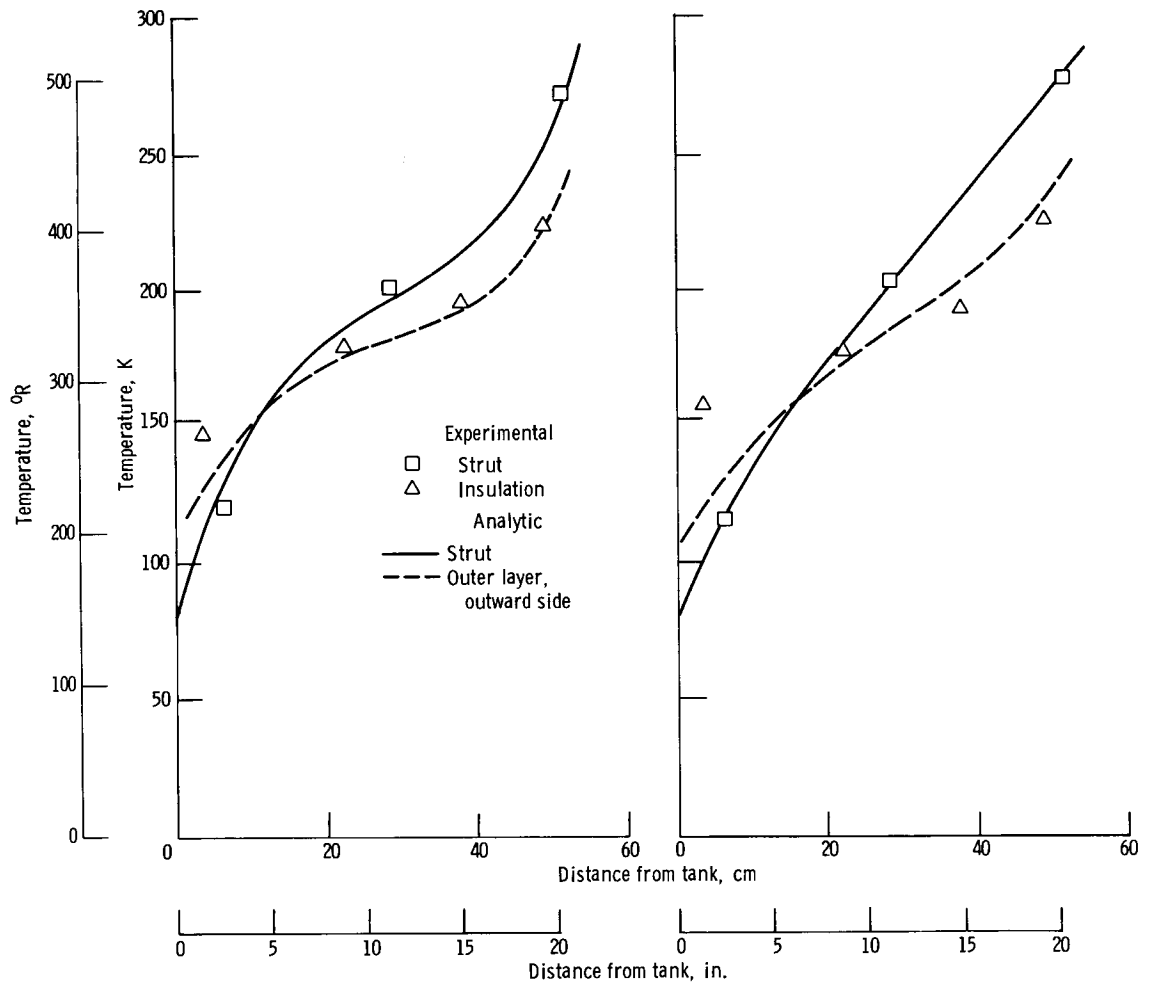
Figure 10. - Temperature profiles for insulated struts with no shields - test 7a. Heater temperature, 296 K (533° R); hydrogen in tank.



(a) Fiberglass strut.

(b) Titanium strut.

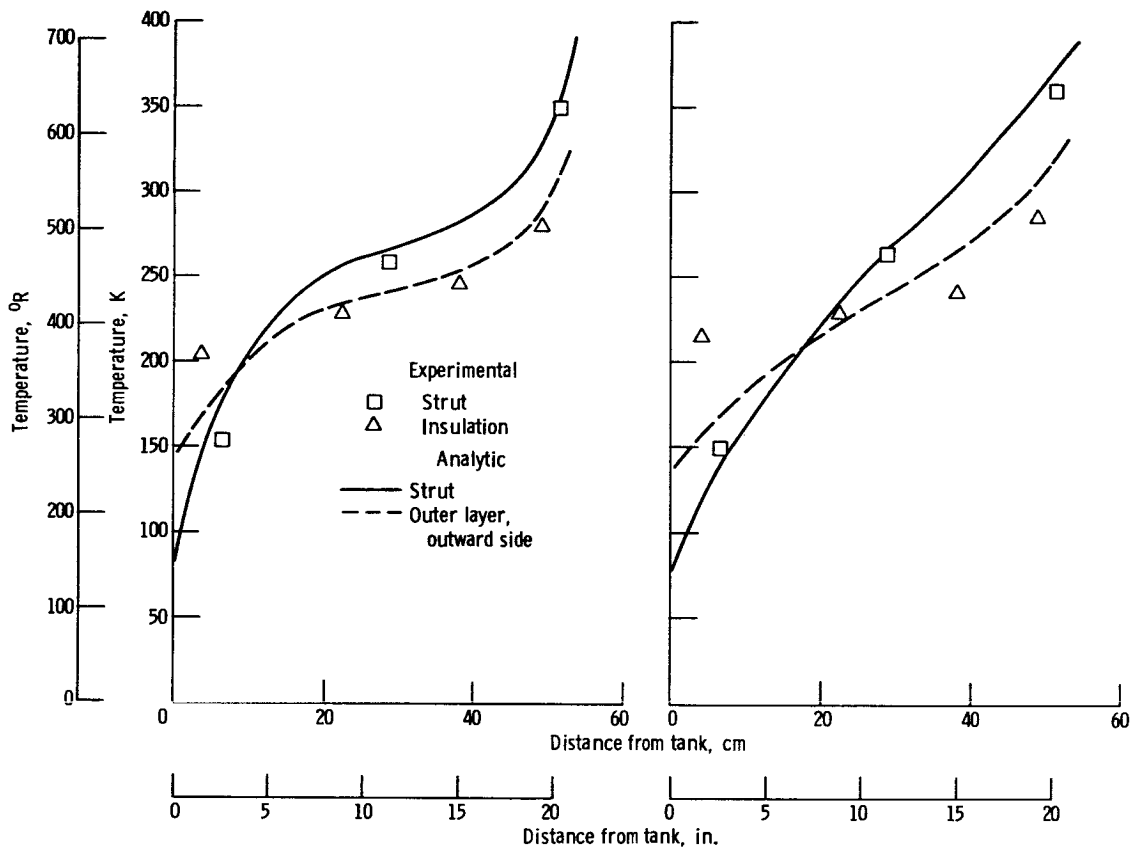
Figure 11. - Temperature profiles for insulated struts with no shields - test 7b. Heater temperature, 388 K (698° R); hydrogen in tank.



(a) Fiberglass strut.

(b) Titanium strut.

Figure 12. - Temperature profiles for insulated struts with no shields - test 1a. Strut length, 54.1 cm (21.3 in.); heater temperature, 289 K (520°R); nitrogen in tank.



(a) Fiberglass strut.

(b) Titanium strut.

Figure 13. - Temperature profiles for insulated struts with no shields - test 1b. Strut length, 54.1 cm (21.3 in.); heater temperature, 389 K (700°R); nitrogen in tank.

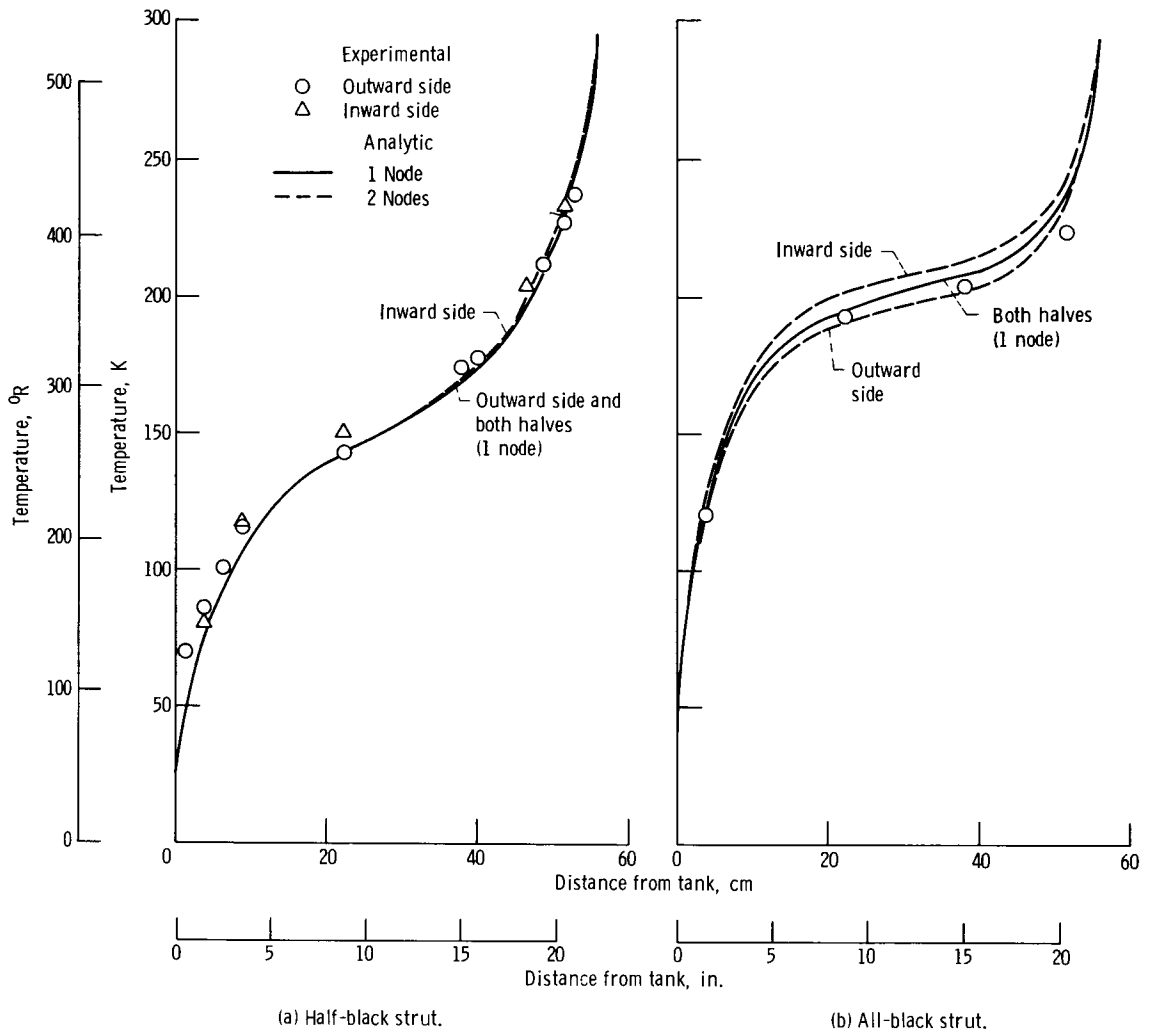
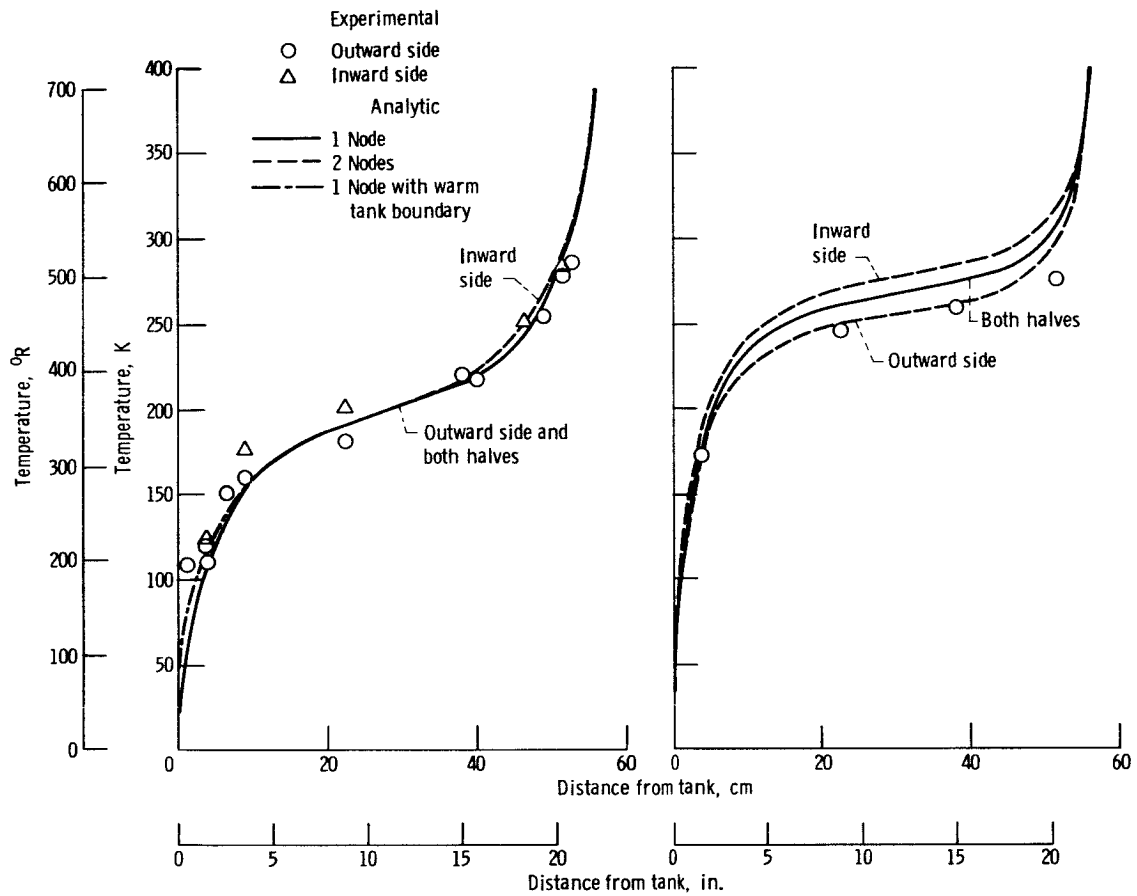


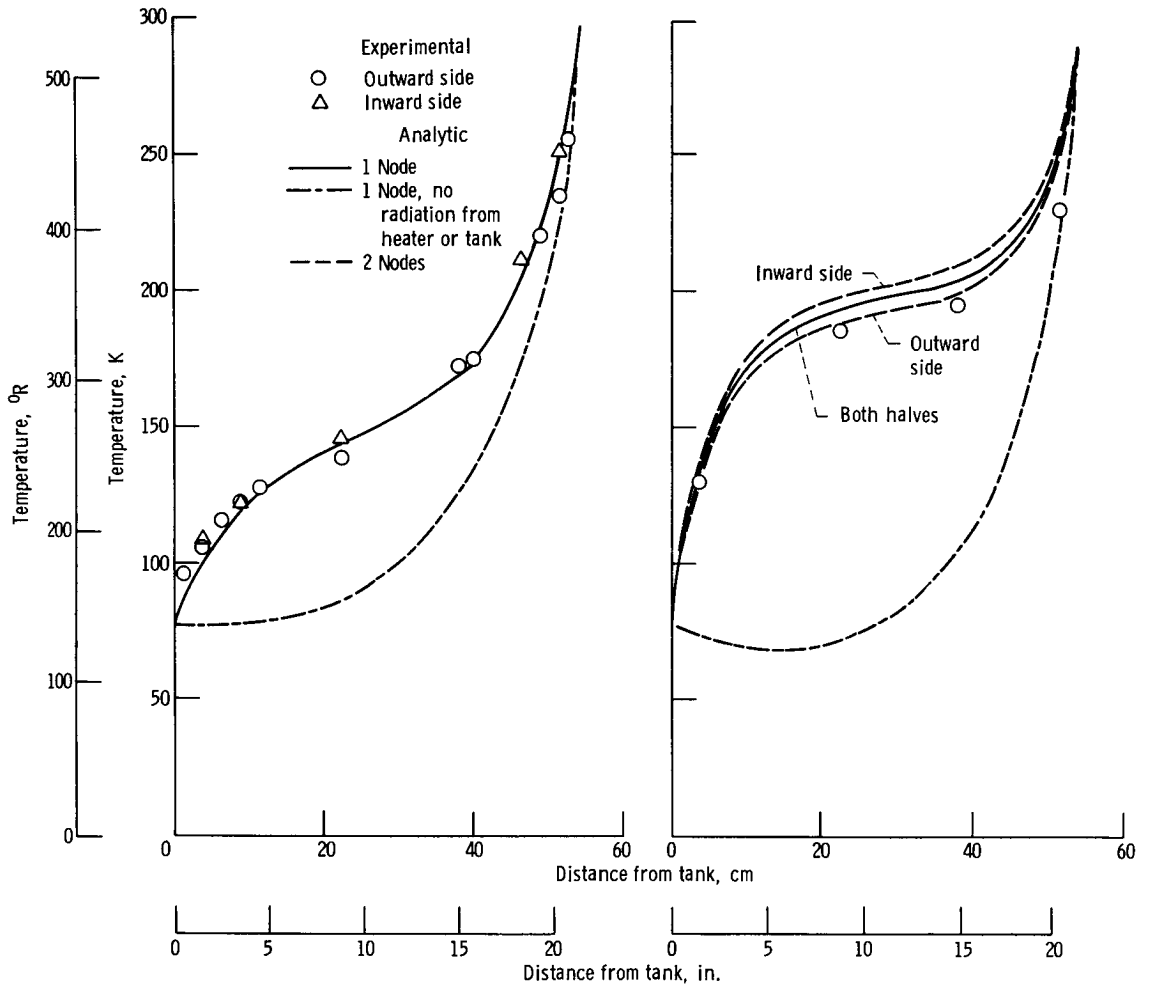
Figure 14. - Temperature profiles for titanium struts with no shields - test 7a. Heater temperature, 296 K (533° R); hydrogen in tank.



(a) Half-black strut.

(b) All-black strut.

Figure 15. - Temperature profiles for titanium struts with no shields - test 7b. Heater temperature, 388 K (698° R); hydrogen in tank.



(a) Half-black strut.

(b) All-black strut.

Figure 16. - Temperature profiles for titanium struts with no shields - test 1a. Strut length, 54.1 cm (21.3 in.); heater temperature, 289 K (520° R); nitrogen in tank.

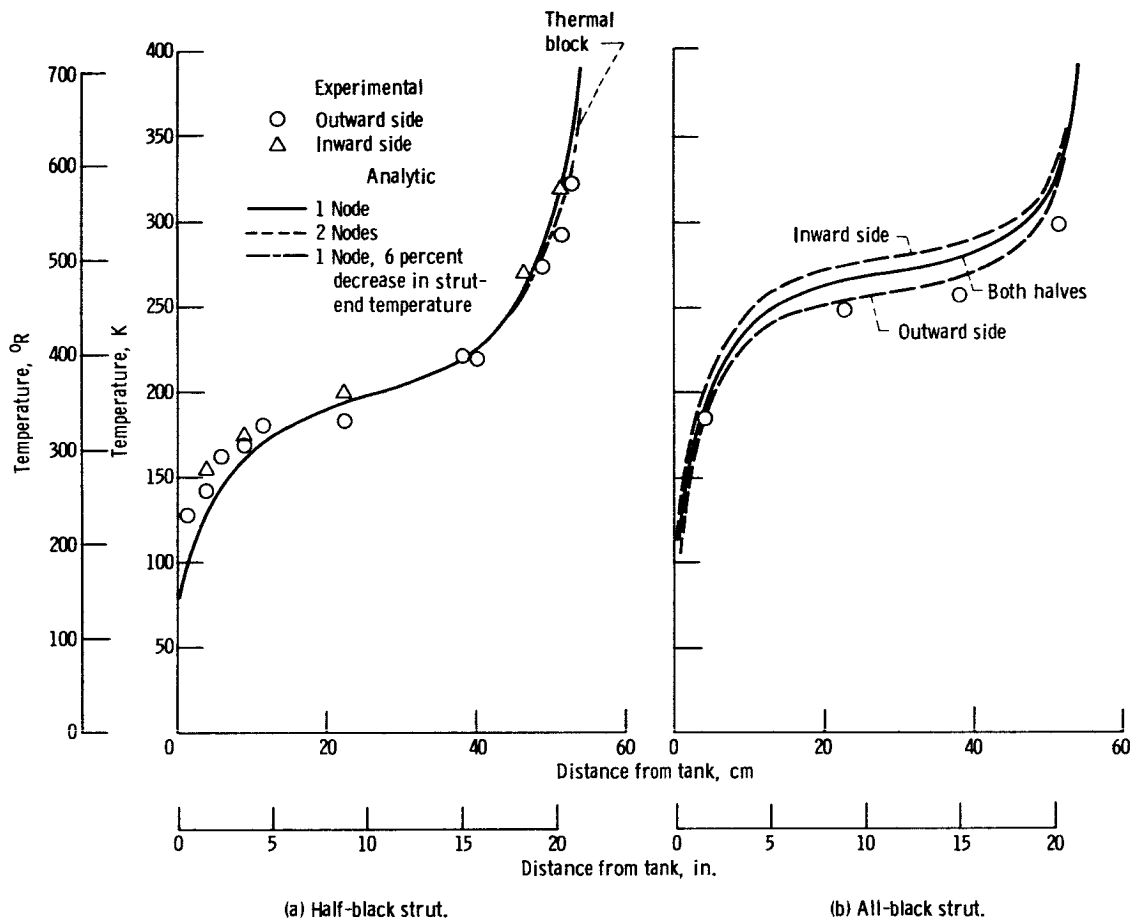
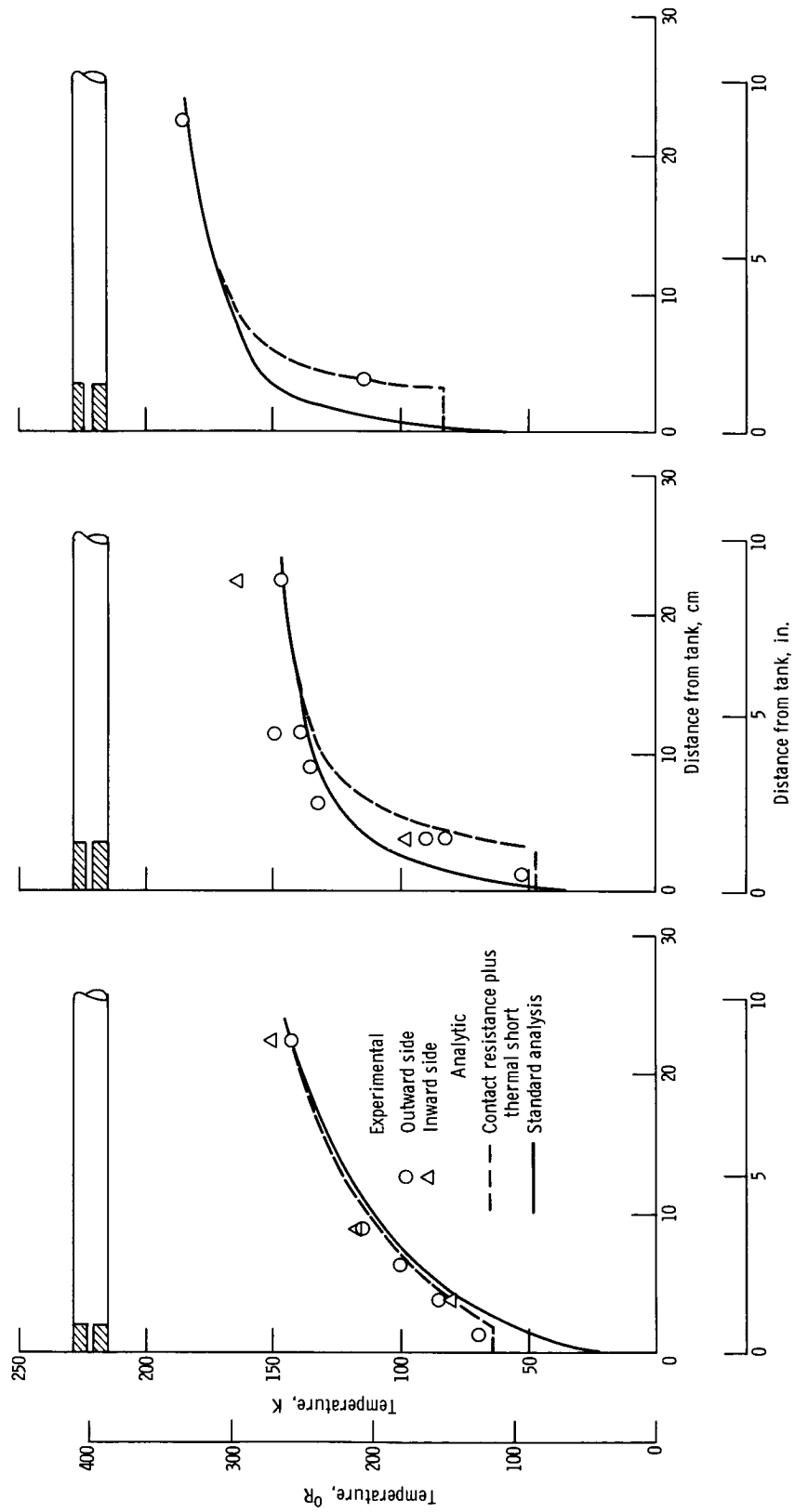


Figure 17. - Temperature profiles for titanium struts with no shields - test Ib. Strut length, 54.1 cm (21.3 in.); heater temperature, 389 K (700° R); nitrogen in tank.



(a) Half-black titanium. One-node analysis.

(b) Half-black fiberglass. One-node analysis.

(c) All-black fiberglass. Two-node analysis (outward side).

Figure 18. - Effect of contact resistance plus end plug on strut temperature profiles near tank end of strut - test 7a. Heater temperature, 296 K (533° R); hydrogen in tank.

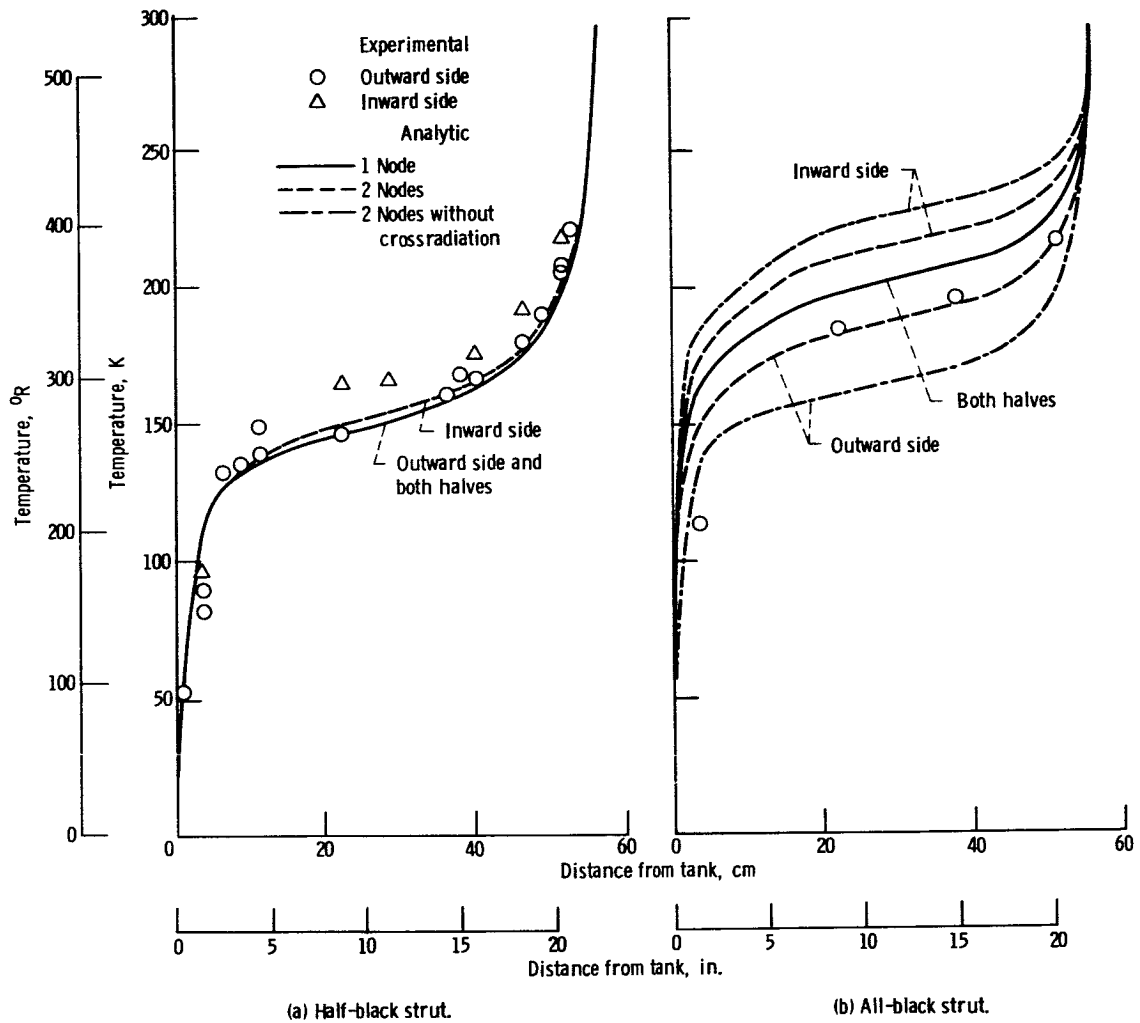


Figure 19. - Temperature profiles for fiberglass struts with no shields - test 7a. Heater temperature, 296 K (533° R); hydrogen in tank.

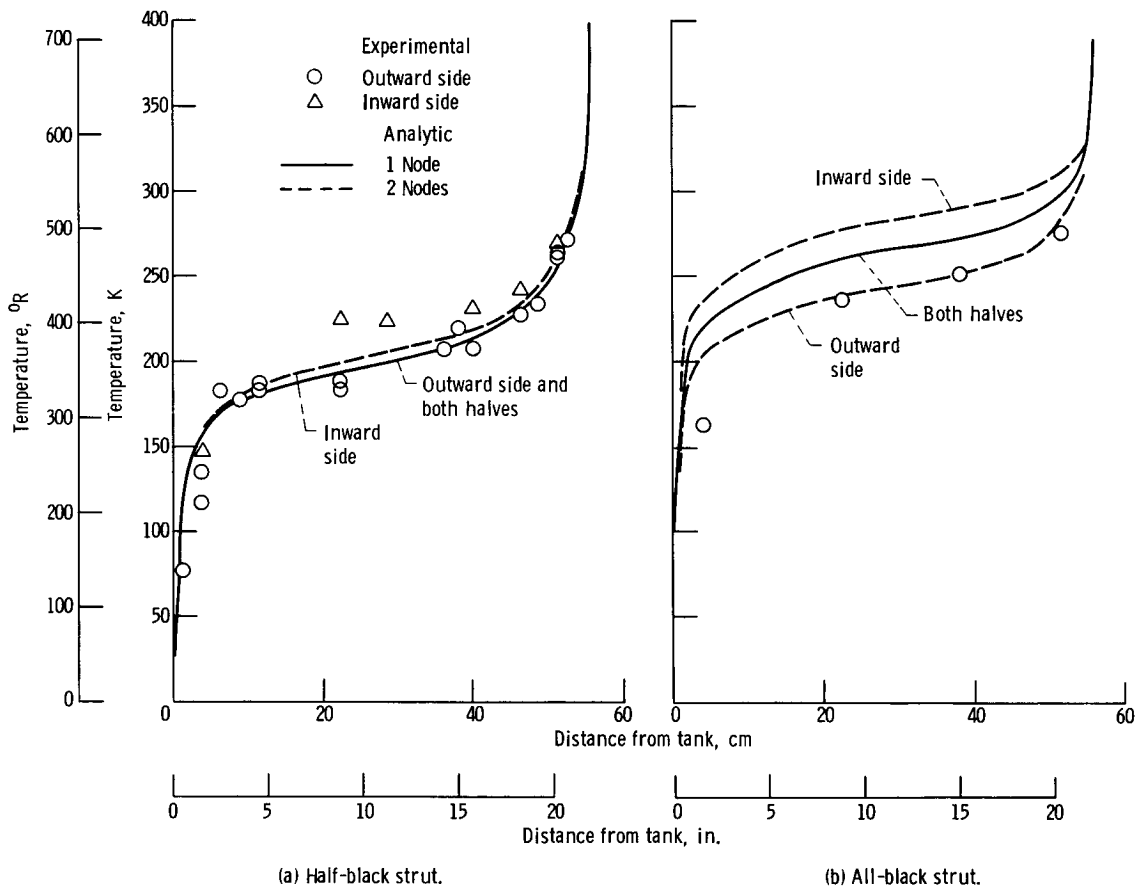


Figure 20. - Temperature profiles for fiberglass struts with no shields - test 7b. Heater temperature, 388 K (698° R); hydrogen in tank.

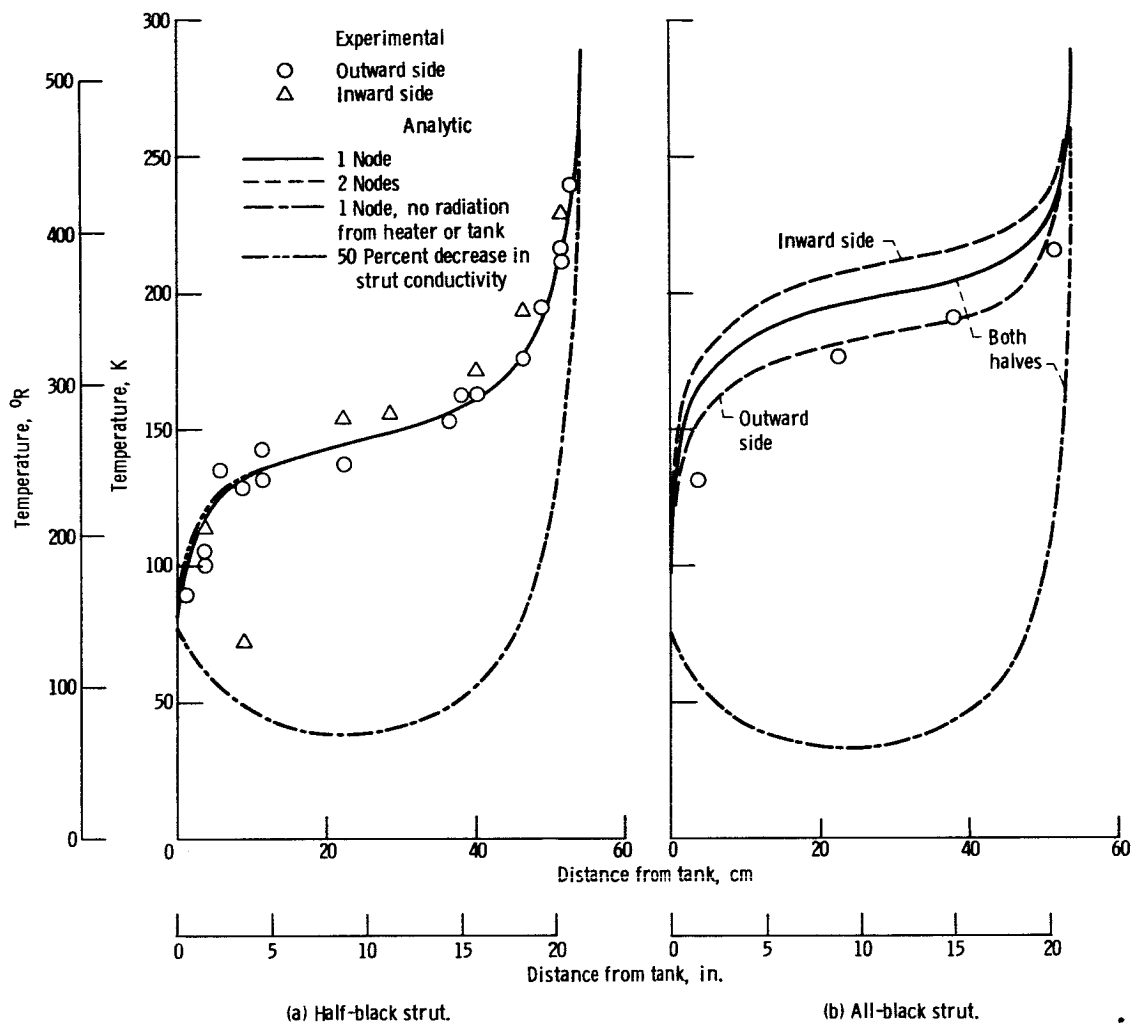
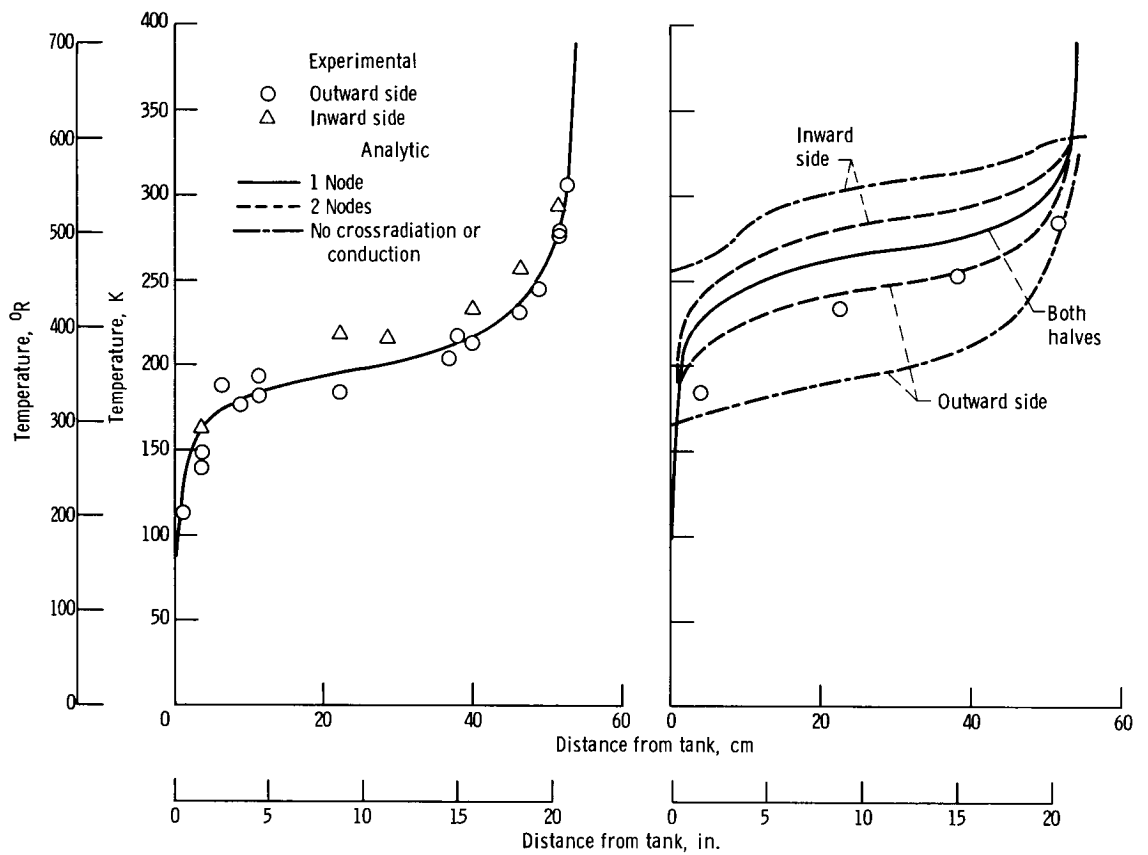


Figure 21. - Temperature profiles for fiberglass struts with no shields - test 1a. Strut length, 54.1 cm (21.3 in.); heater temperature, 289 K (520° R); nitrogen in tank.

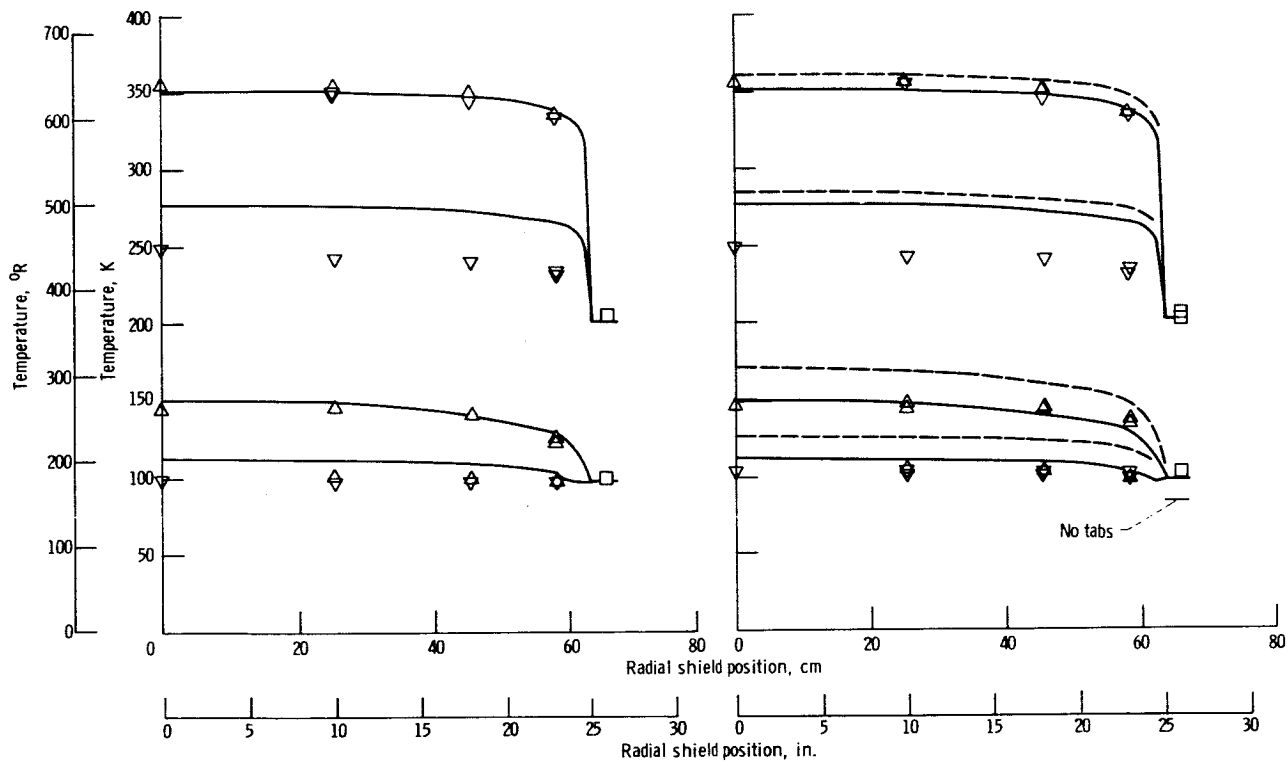


(a) Half-black strut.

(b) All-black strut.

Figure 22. - Temperature profiles for fiberglass struts with no shields - test 1b. Strut length, 54.1 cm (21.3 in.); heater temperature, 389 K (700° R); nitrogen in tank.

Experimental
 △ Side facing heater
 ▽ Side facing tank
 □ Shield ring
 Analytic
 — Standard analysis
 - - - Directional effects neglected



(a) Tank with liquid hydrogen.

(b) Tank with liquid nitrogen.

Figure 23. - Shield and ring temperature profiles with 12 fiberglass struts - tests 6b and 6d. Evenly spaced shields; high-temperature heater.

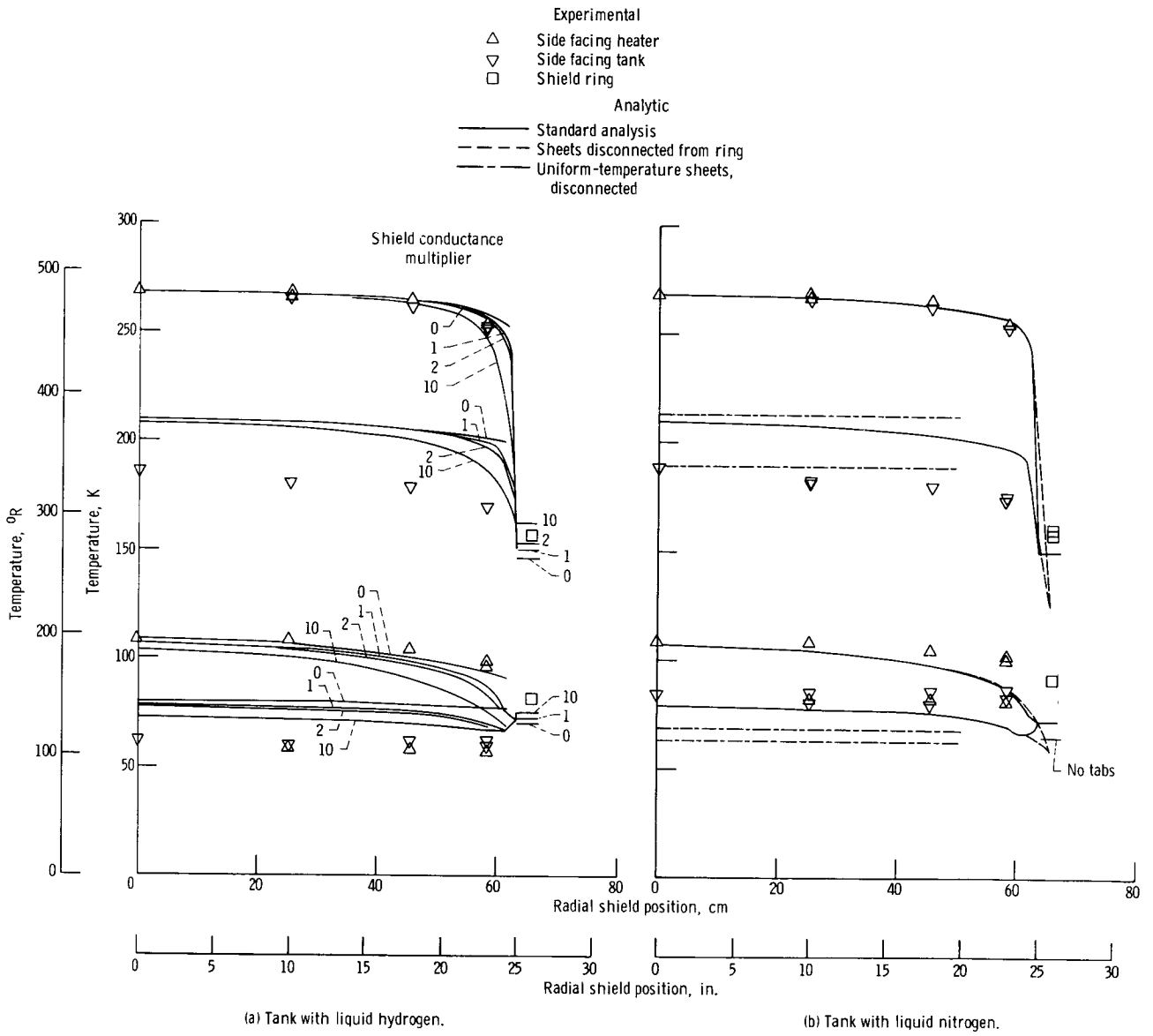
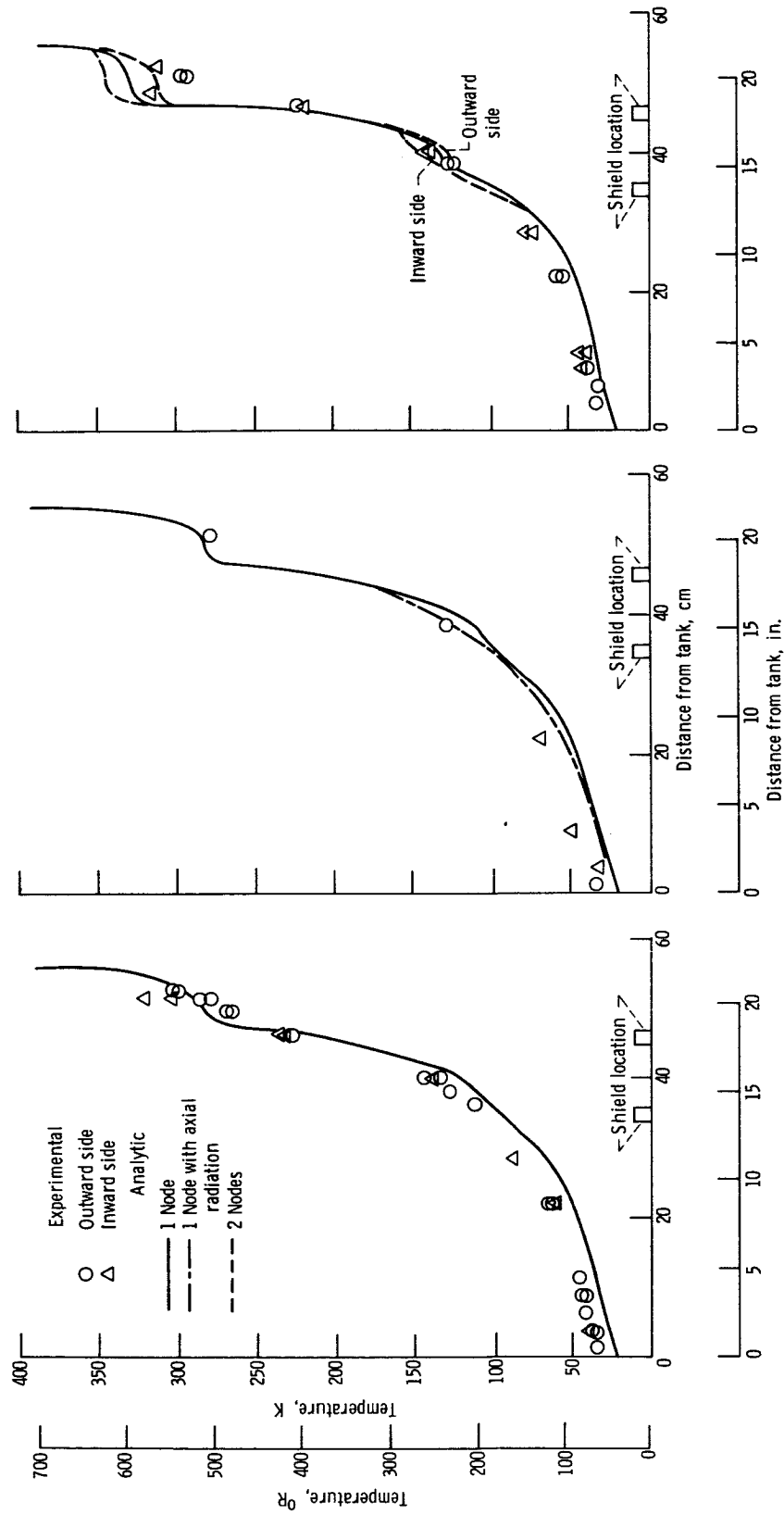


Figure 24. - Shield and ring temperature profiles with 12 fiberglass struts - tests 6a and 6c. Evenly spaced shields; room-temperature heater.

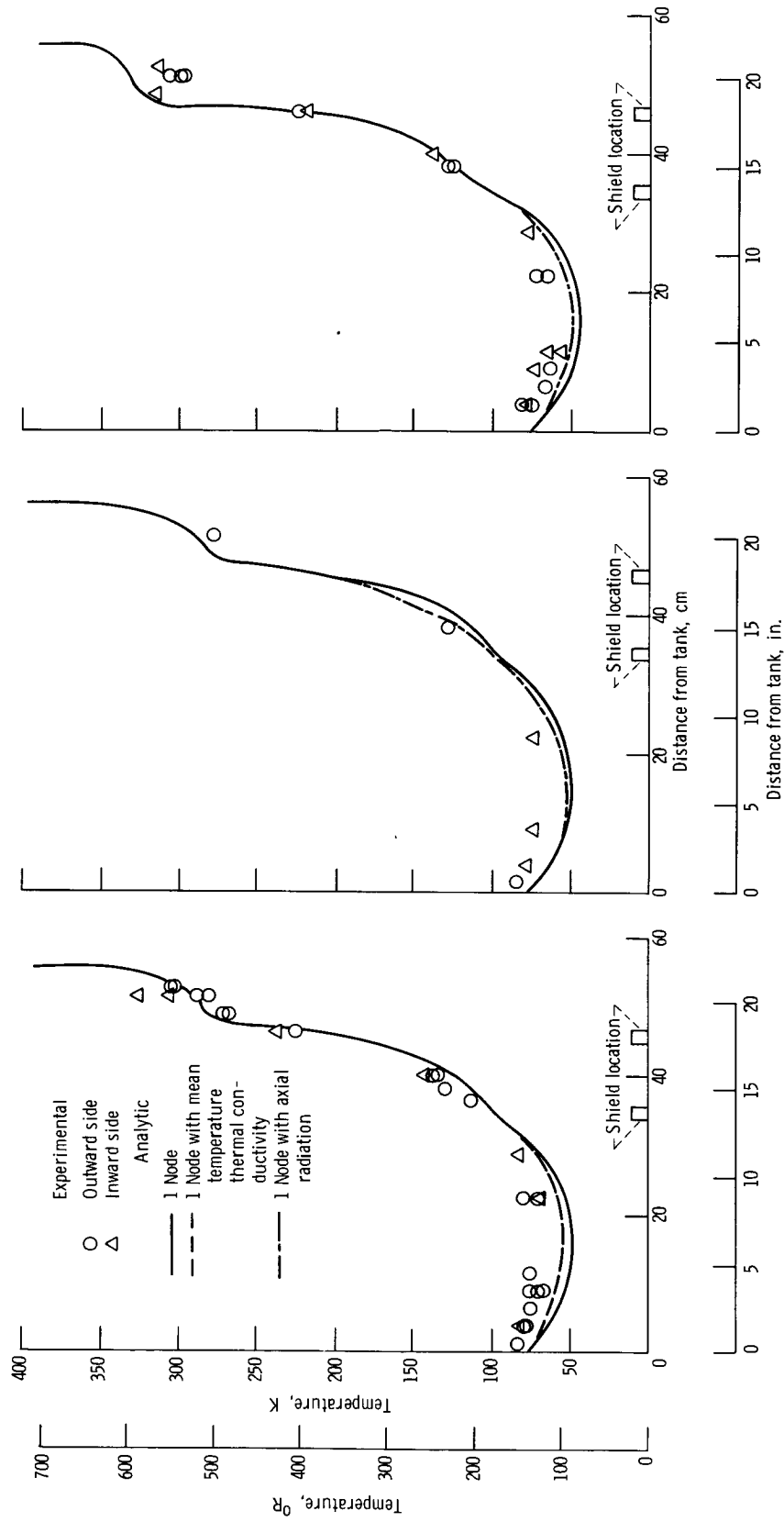


(a) Half-black strut.

(b) Half-black strut, no barriers.

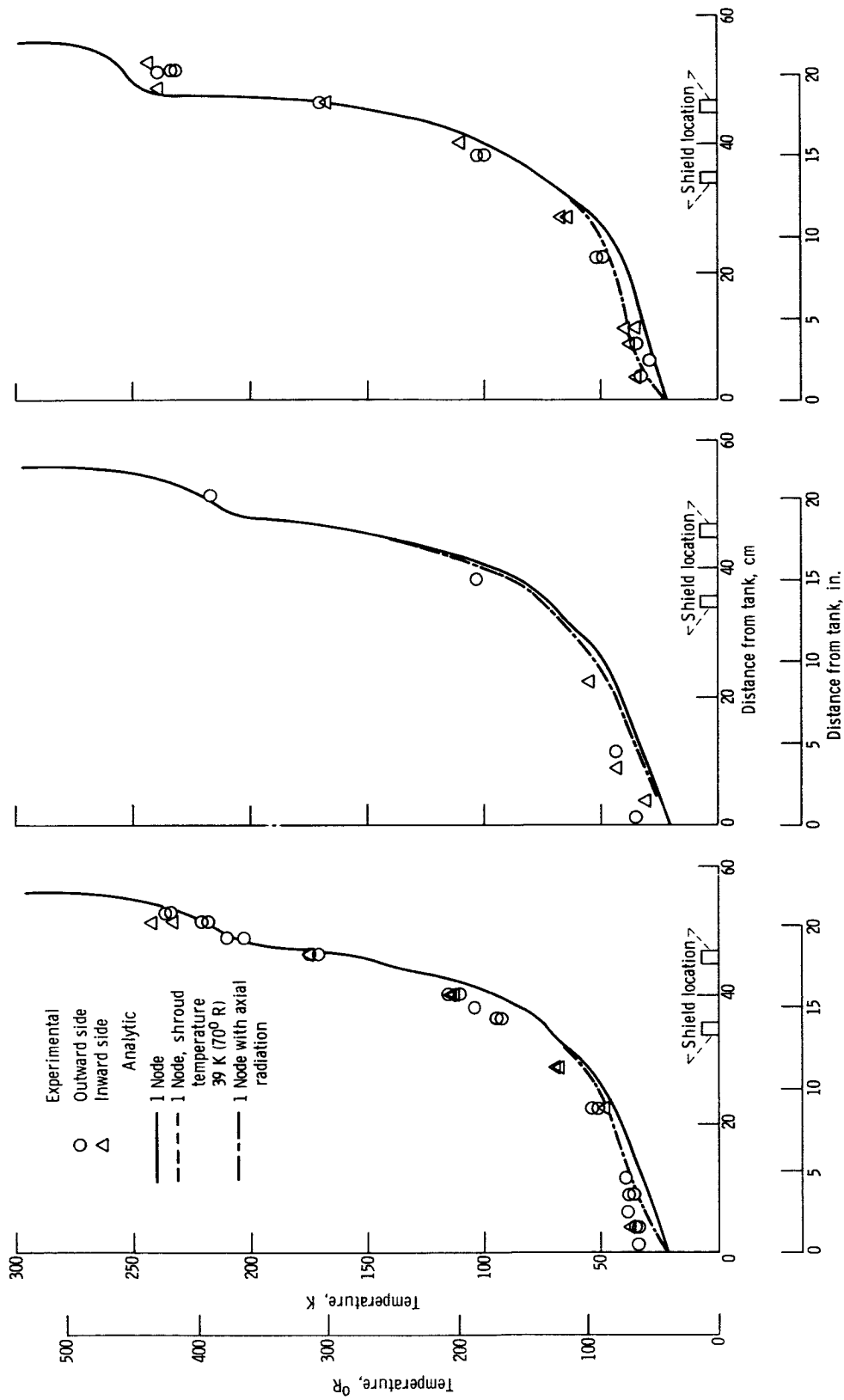
(c) All-black strut.

Figure 25. - Strut temperature profiles for 12 fiberglass struts - test 6b. Evenly spaced shields; heater temperature, 387 K (697° R); hydrogen in tank.

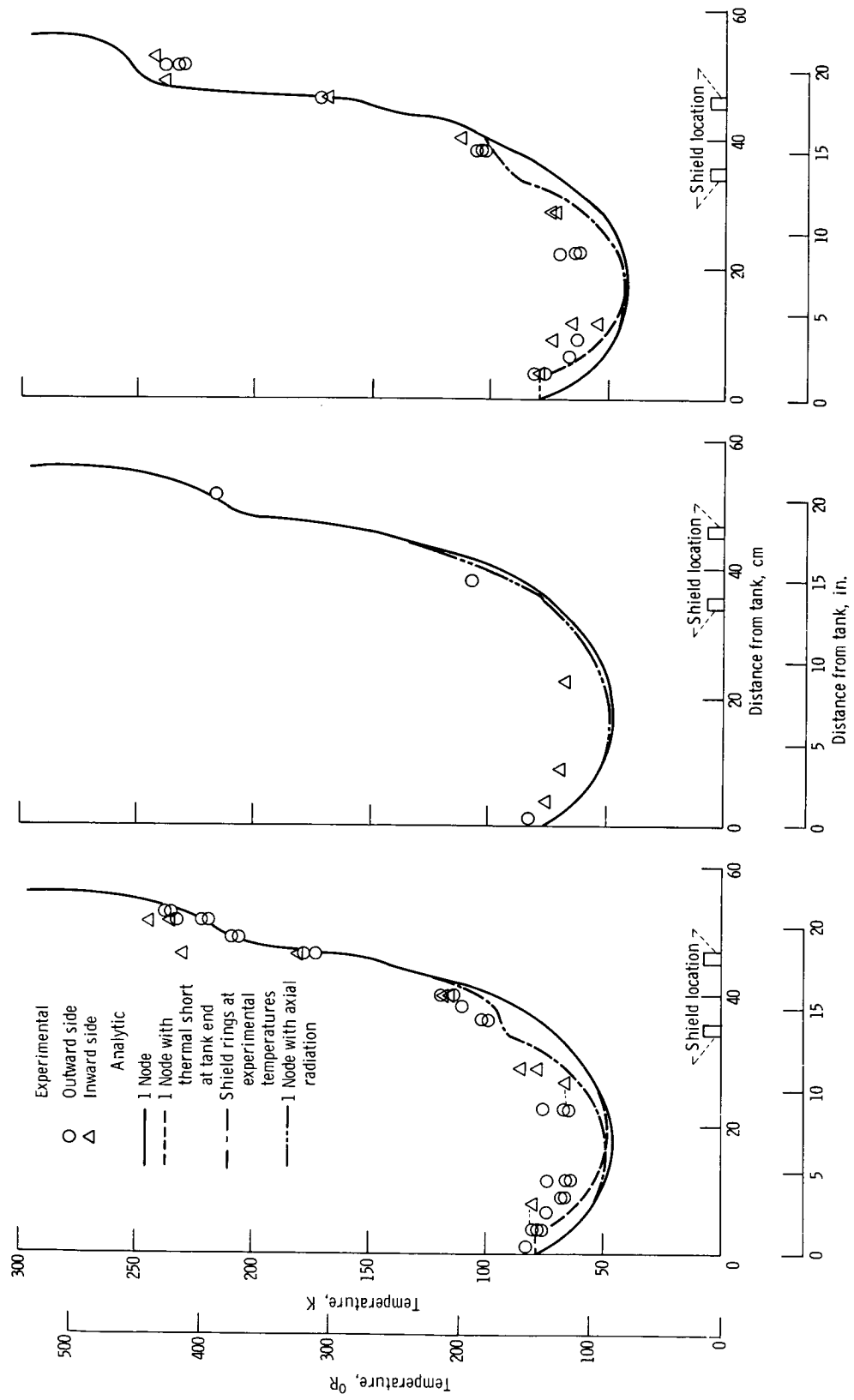


(a) Half-black strut.
 (b) Half-black strut, no barriers.
 (c) All-black strut.

Figure 26. - Strut temperature profiles for 12 fiberglass struts - test 6d. Evenly spaced shields; heater temperature, 388 K (698° R); nitrogen in tank.



(a) Half-black strut. (b) Half-black strut, no barriers. (c) All-black strut.
 Figure 27. - Strut temperature profiles for 12 fiberglass struts - test 6a. Evenly spaced shields; heater temperature, 296 K (533° R); hydrogen in tank.



(a) Half-black strut. (b) Half-black strut, no barriers. (c) All-black strut. Figure 28. - Strut temperature profiles for 12 fiberglass struts - test 6c. Evenly spaced shields; heater temperature, 296 K (533° R); nitrogen in tank.

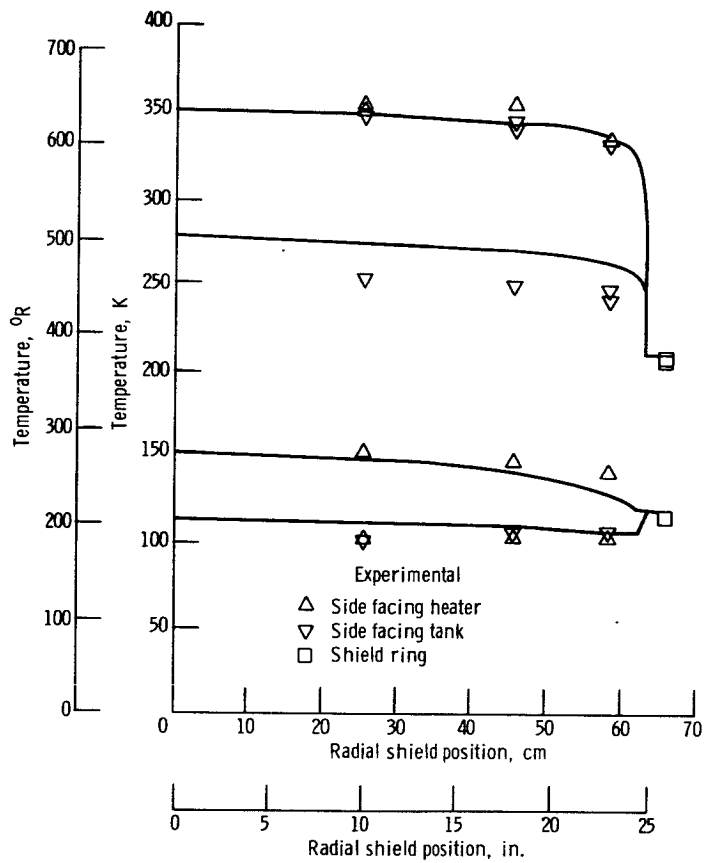


Figure 29. - Shield and ring temperature profiles with 1 fiberglass and 11 titanium struts - test 3b. Evenly spaced shields; heater temperature, 388 K (699° R); nitrogen in tank.

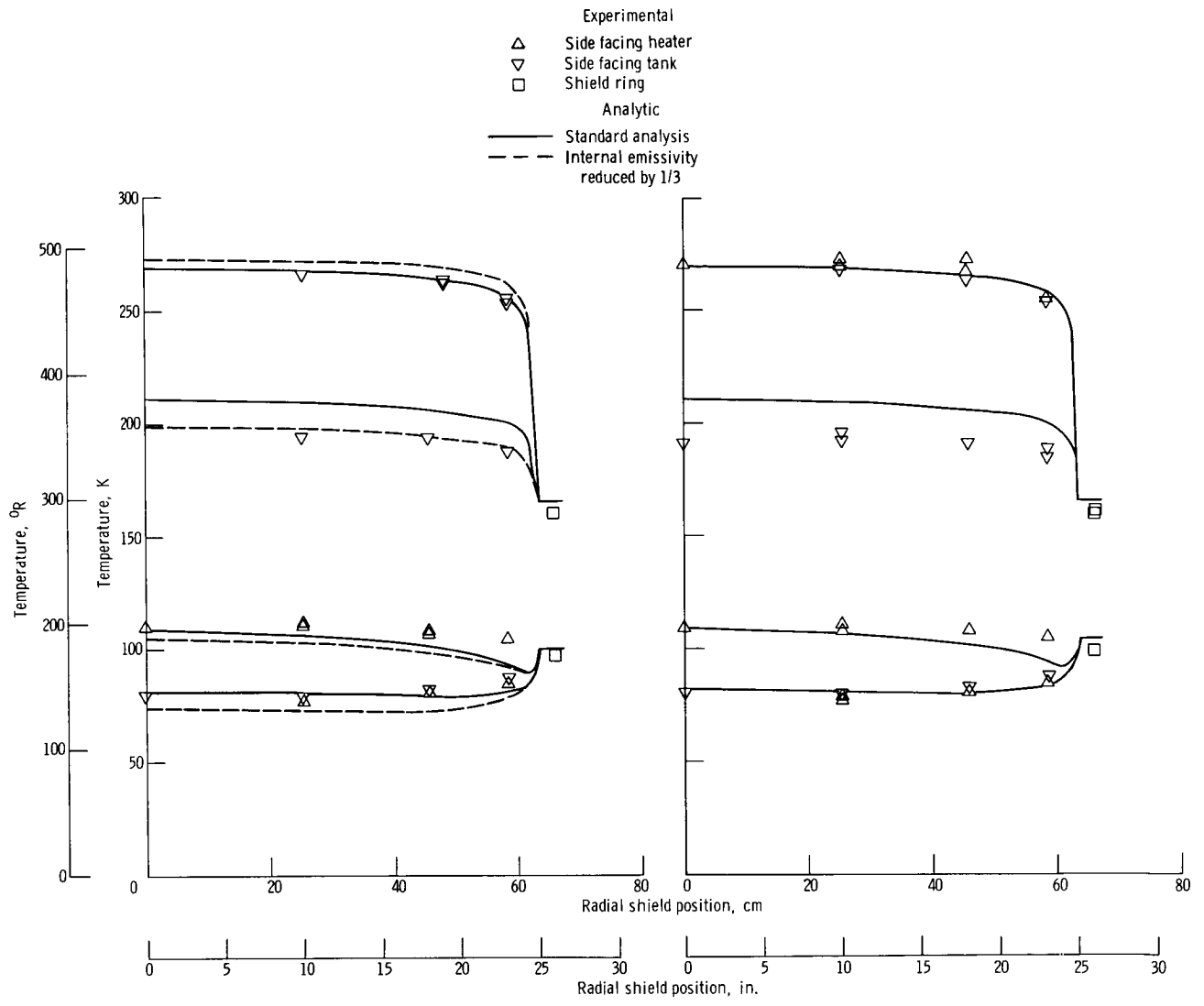
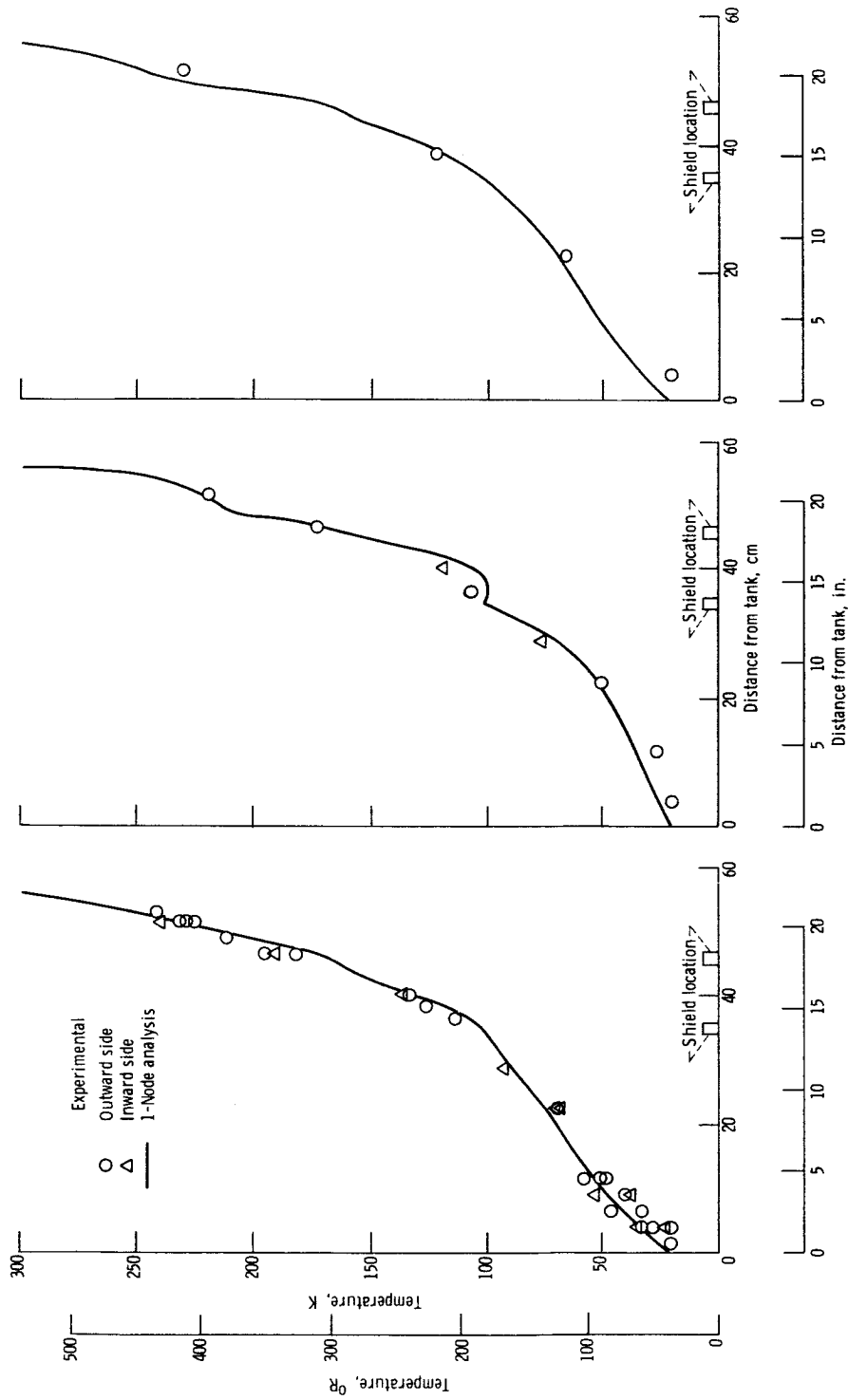
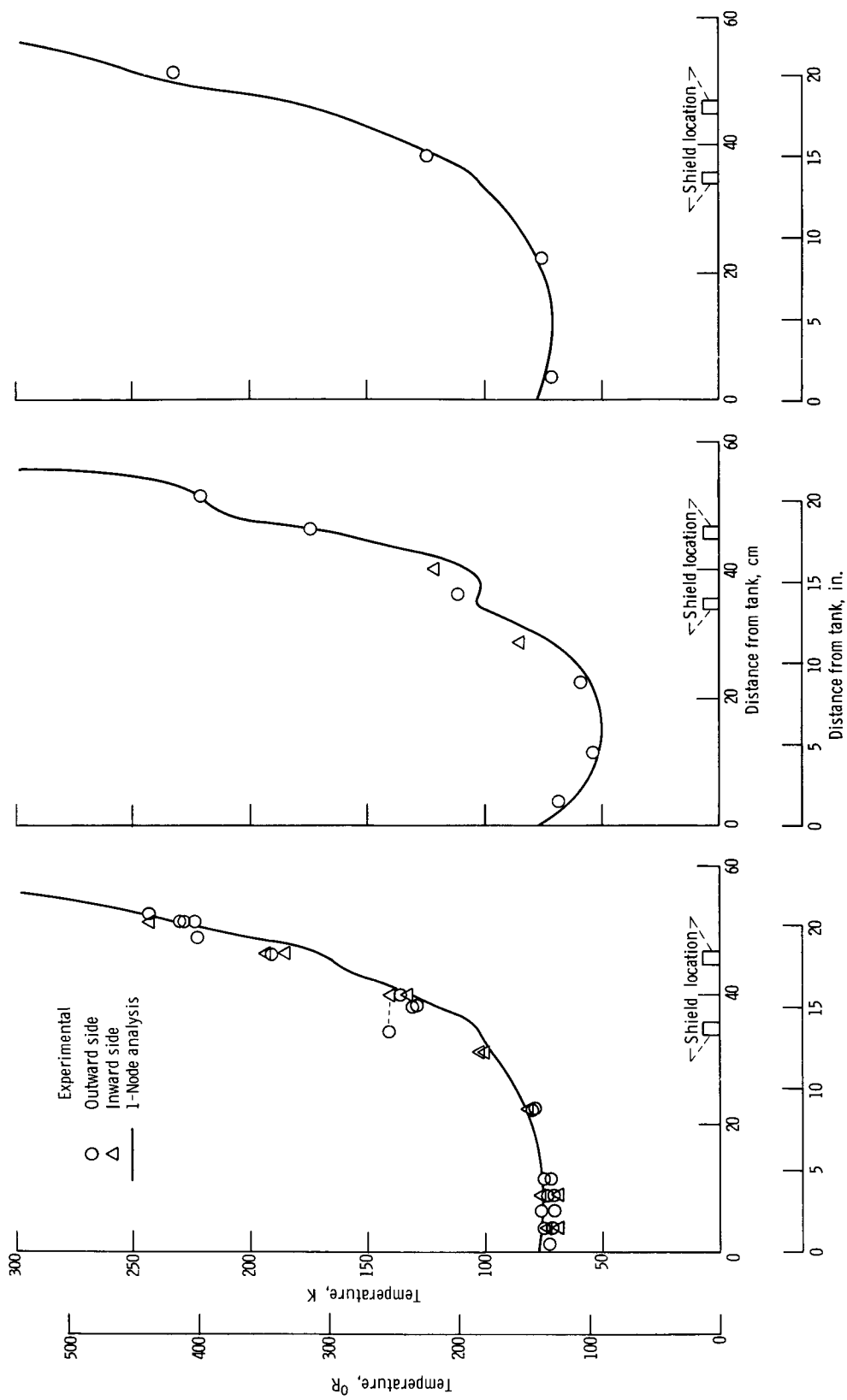


Figure 30. - Shield and ring temperature profiles with 1 fiberglass and 11 titanium struts - tests 2 and 3a. Evenly spaced shields; room-temperature heater.



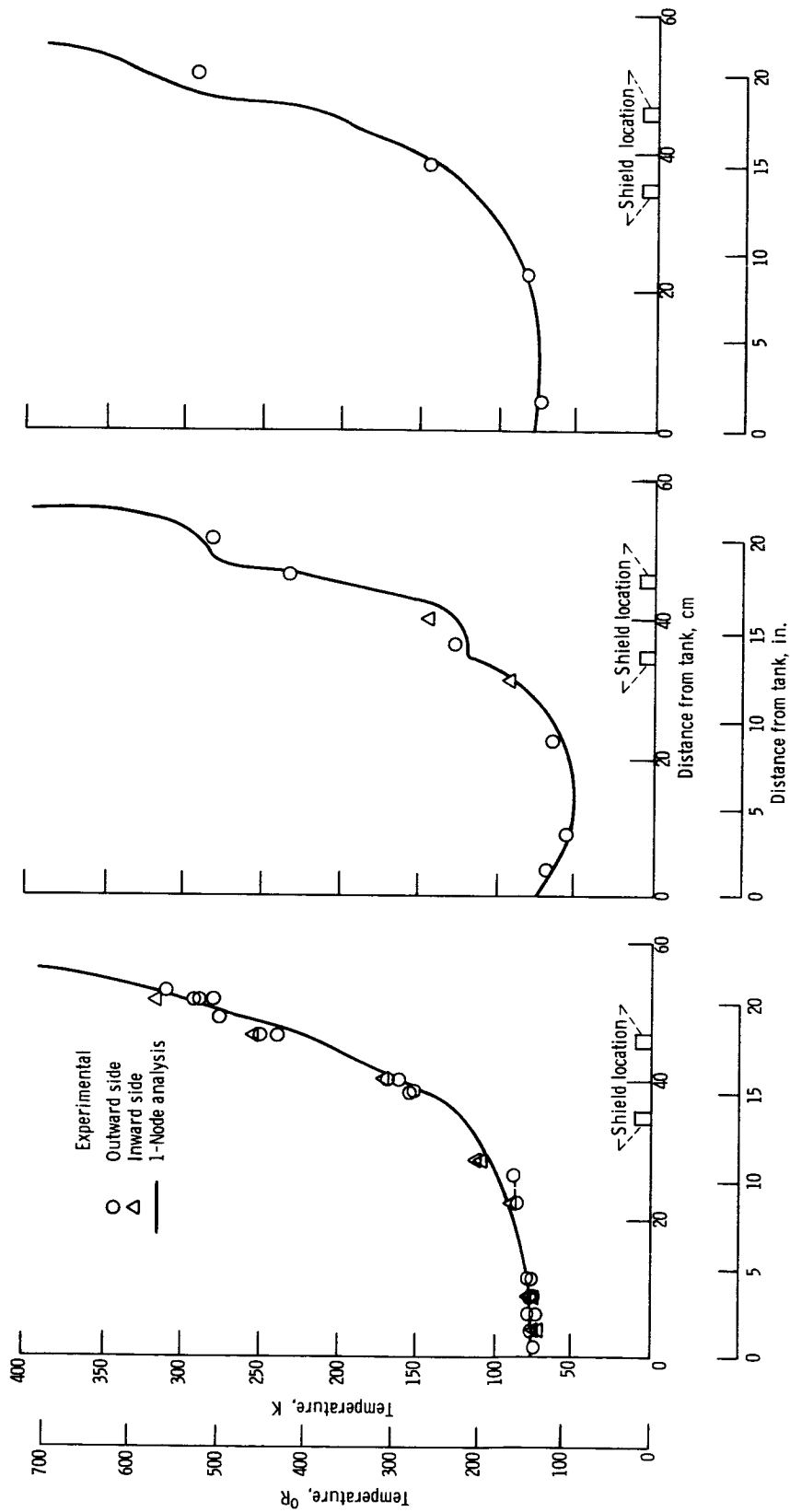
(a) Half-black titanium strut.
 (b) Half-black fiberglass strut.
 (c) All-black titanium strut.

Figure 31. - Strut temperature profiles with 1 fiberglass and 11 titanium struts - test 2. Evenly spaced shields; heater temperature, 297 K (534° R); hydrogen in tank.



(a) Half-black titanium strut.
 (b) Half-black fiberglass strut.
 (c) All-black titanium strut.

Figure 32. - Strut temperature profiles with 1 fiberglass and 11 titanium struts - test 3a. Evenly spaced shields; heater temperature, 297 K (535° R); nitrogen in tank.



(a) Half-black titanium strut.
 (b) Half-black fiberglass strut.
 (c) All-black titanium strut.

Figure 33. - Strut temperature profiles with 1 fiberglass and 11 titanium struts - test 3b. Evenly spaced shields; heater temperature, 388 K (699°R); nitrogen in tank.

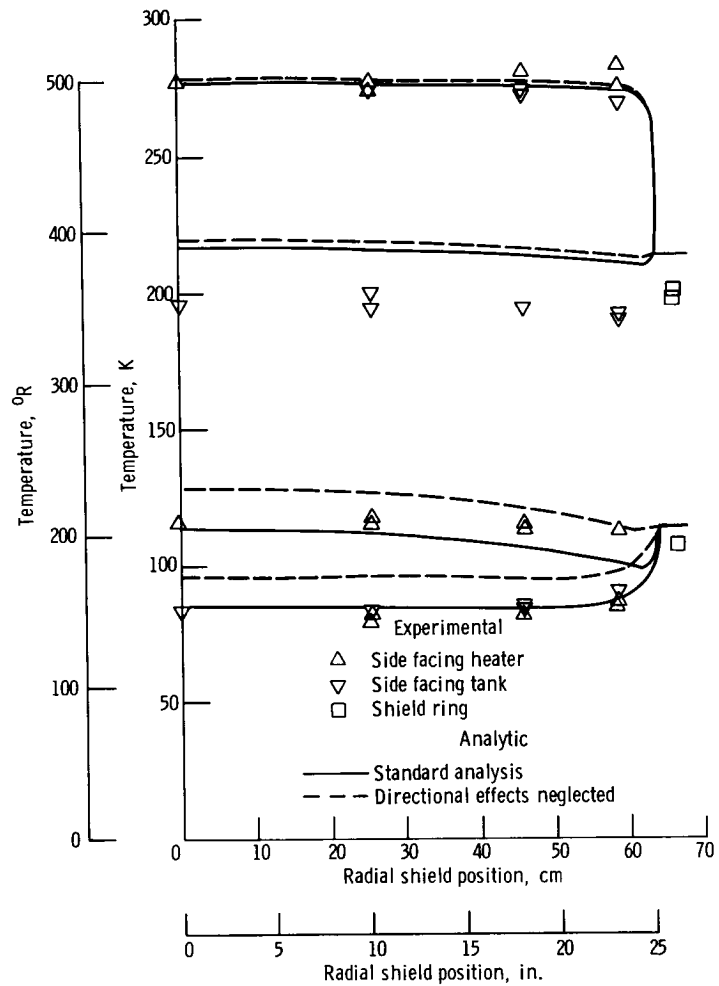
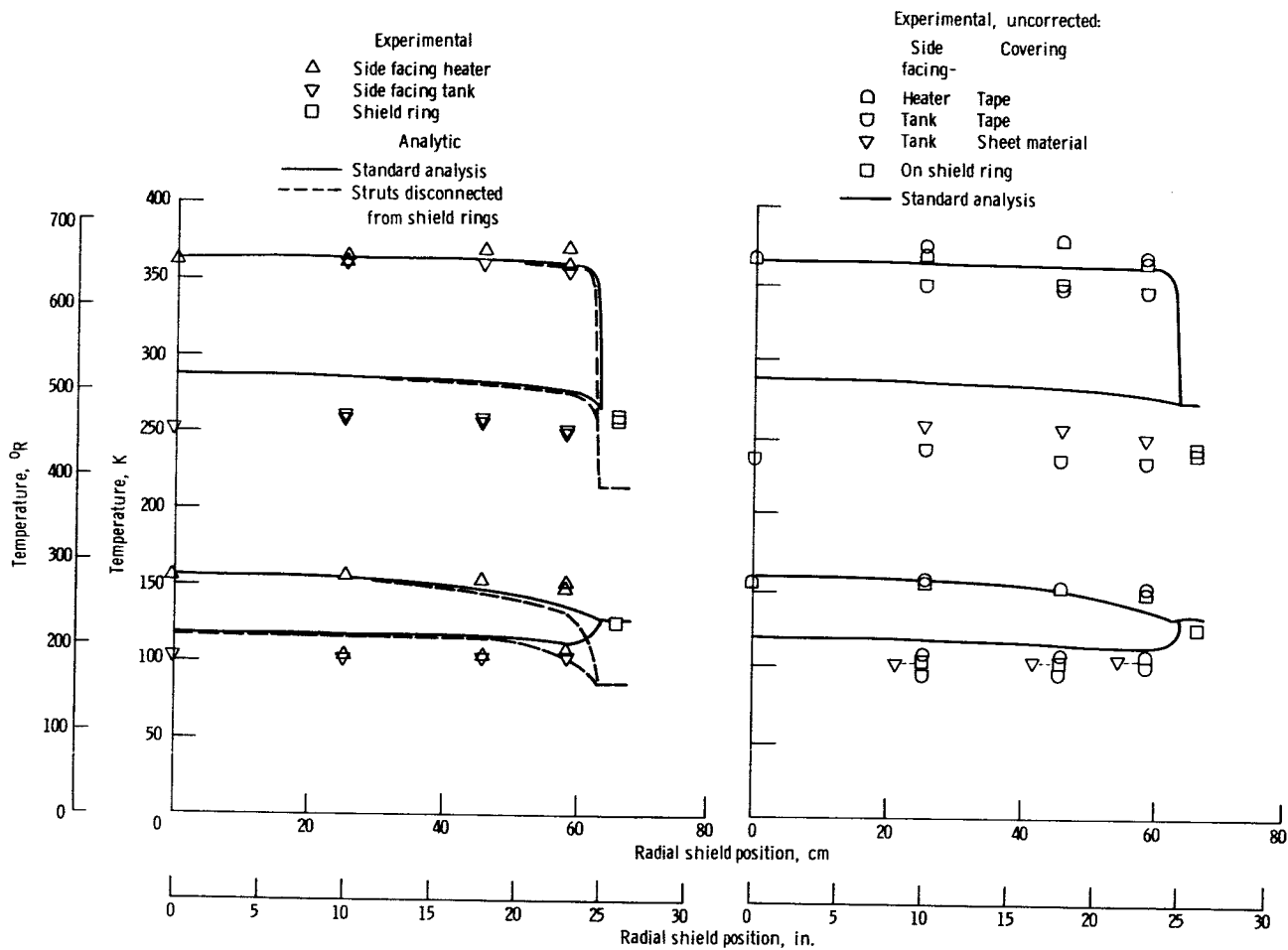


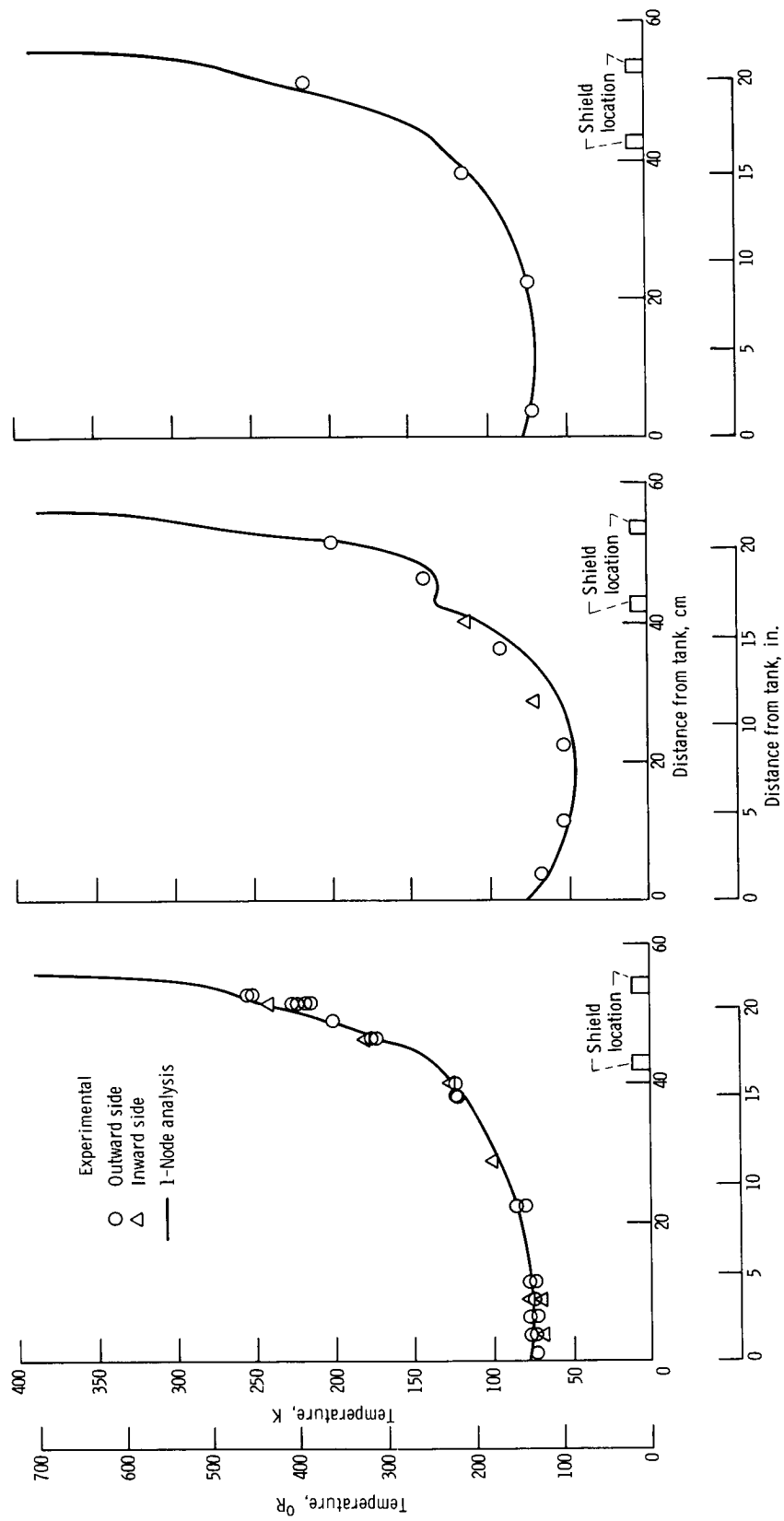
Figure 34. - Shield and ring temperature profiles with nine titanium struts connected to shield ring - test 5a. Closely spaced shields; heater temperature, 296 K (533° R); nitrogen in tank.



(a) Nine titanium struts connected to rings.

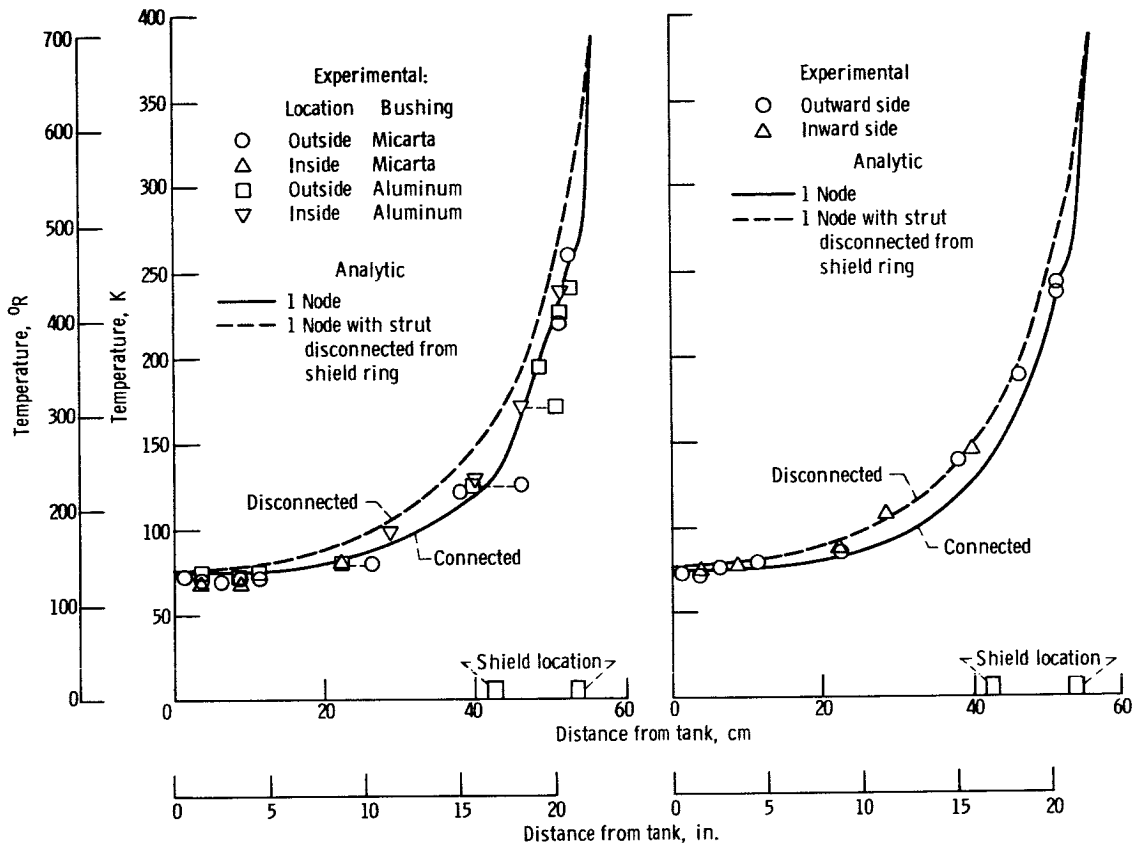
(b) Eleven titanium struts connected to rings.

Figure 35. - Effect of material used to cover thermocouple leads on sheet temperatures - tests 5a and 4. Closely spaced shields; high-temperature heater; nitrogen in tank.



(a) Half-black titanium strut.
 (b) Half-black fiberglass strut.
 (c) All-black titanium strut.

Figure 36. - Strut temperature profiles with 1 fiberglass and 11 titanium struts - test 4. Closely spaced shields, heater temperature, 389 K (700° R); nitrogen in tank.



(a) Micarta and aluminum bushings.

(b) No bushings.

Figure 37. - Effect of strut-ring bushing material on temperature profiles for half-black titanium struts - test 5b. Closely spaced shields; heater temperature, 388 K (699° R); nitrogen in tank.

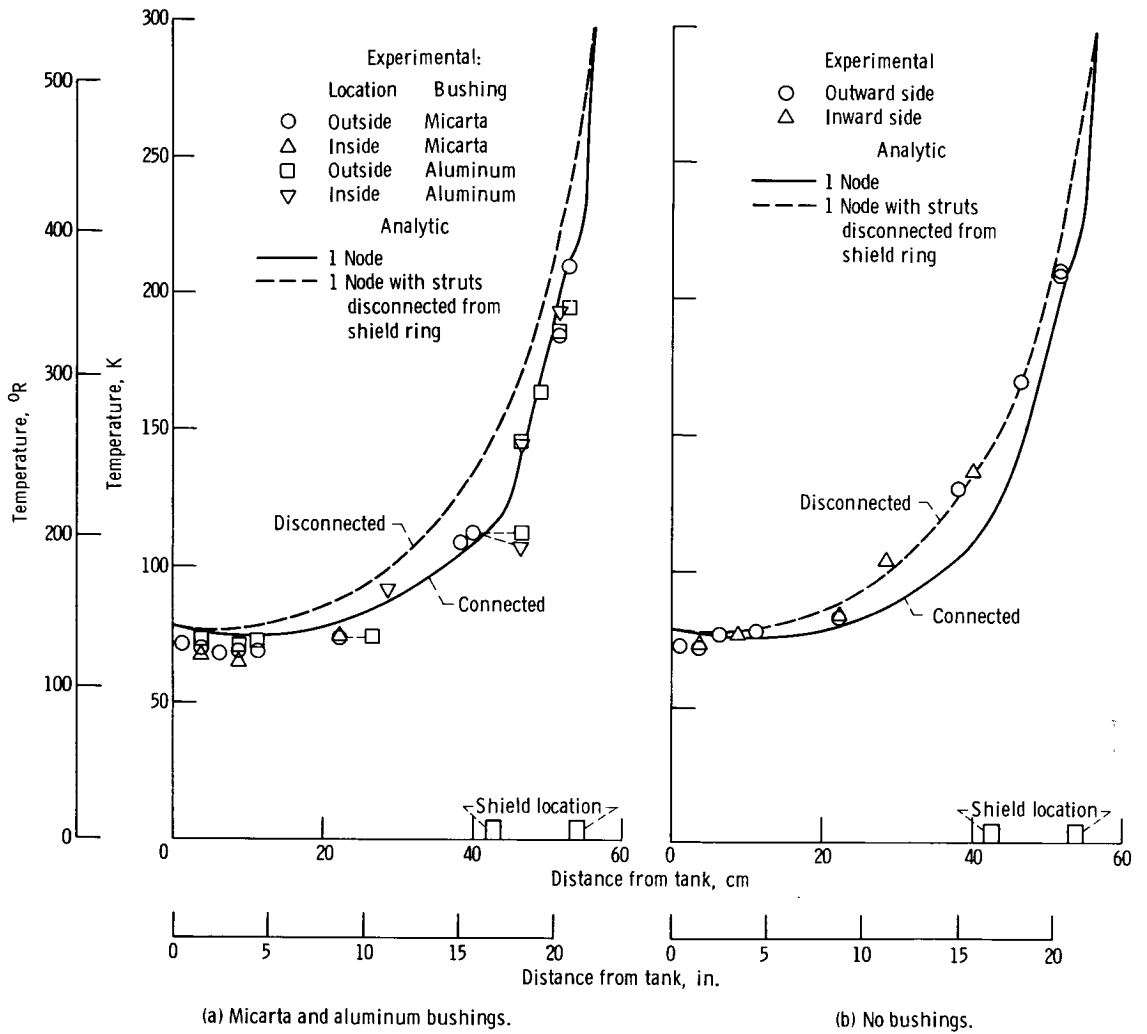
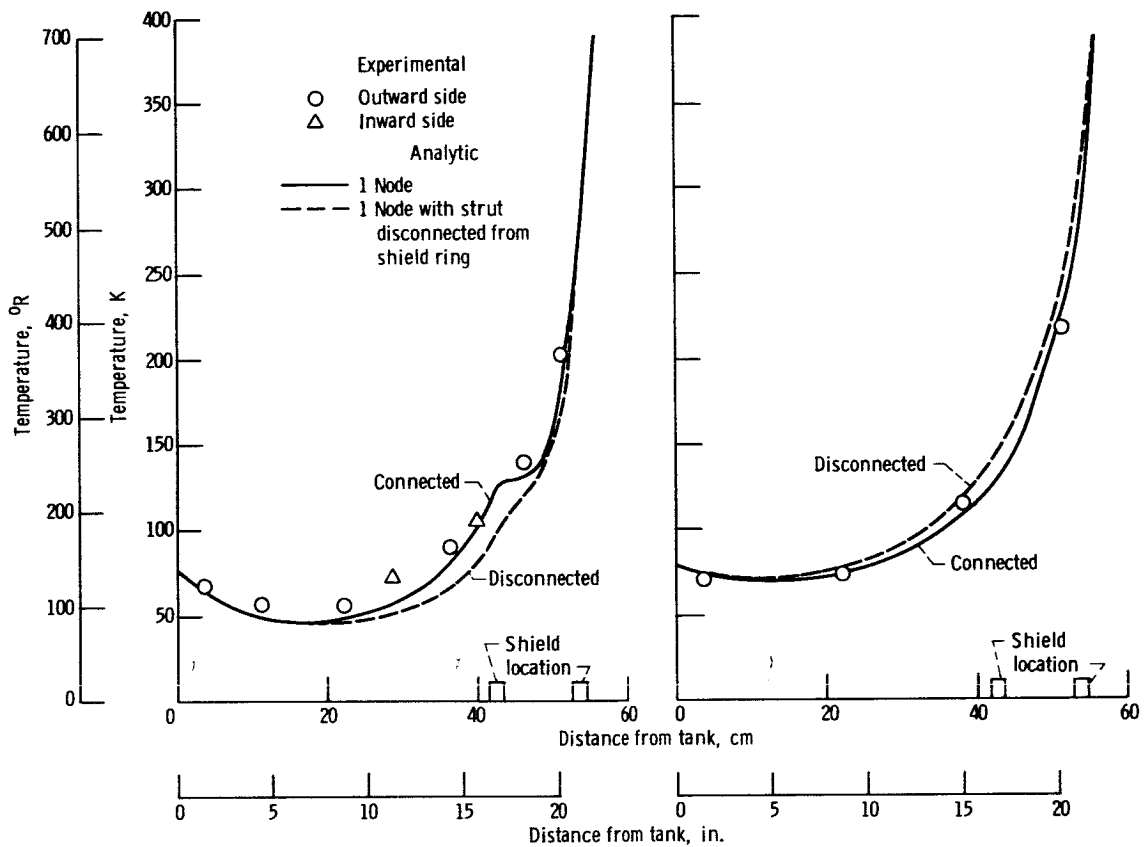


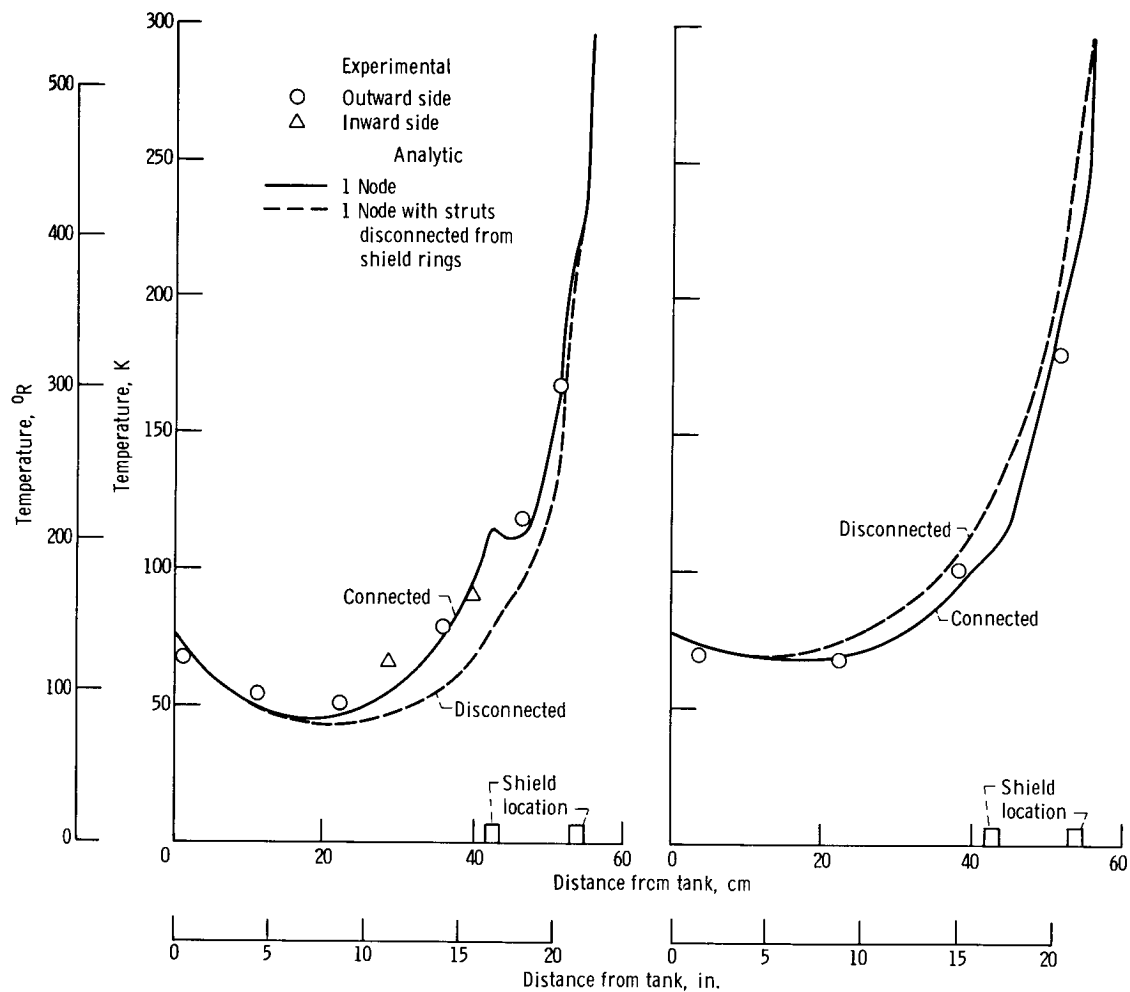
Figure 38. - Effect of strut-ring bushing material on temperature profiles for half-black titanium struts - test 5a. Closely spaced shields; heater temperature, 296 K (533° R); nitrogen in tank.



(a) Half-black fiberglass struts, no bushings.

(b) All-black titanium struts, Micarta bushings.

Figure 39. - Effect of strut-ring bushing material on strut temperature profiles - test 5b. Closely spaced shields; heater temperature, 388 K (699° R); nitrogen in tank.



(a) Half-black fiberglass struts, no bushings.

(b) All-black titanium struts, Micarta bushings.

Figure 40. - Effect of strut-ring bushing material on strut temperature profiles - test 5a. Closely spaced shields; heater temperature, 296 K (533° R); nitrogen in tank.

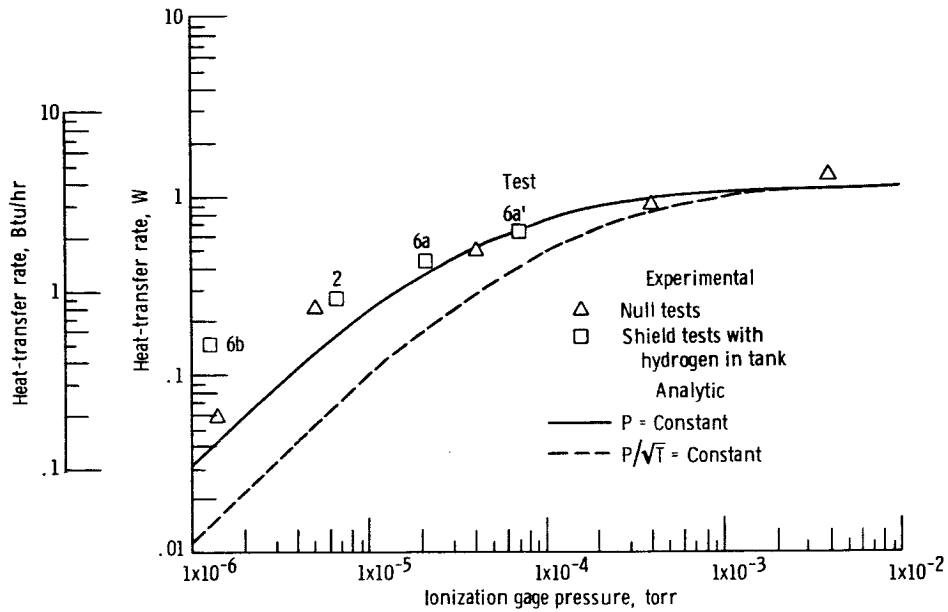


Figure 41. - Heat-transfer rate for null tests as function of vacuum gage pressure reading. Tank-to-shroud temperature difference, 7.2 K (13^o R).

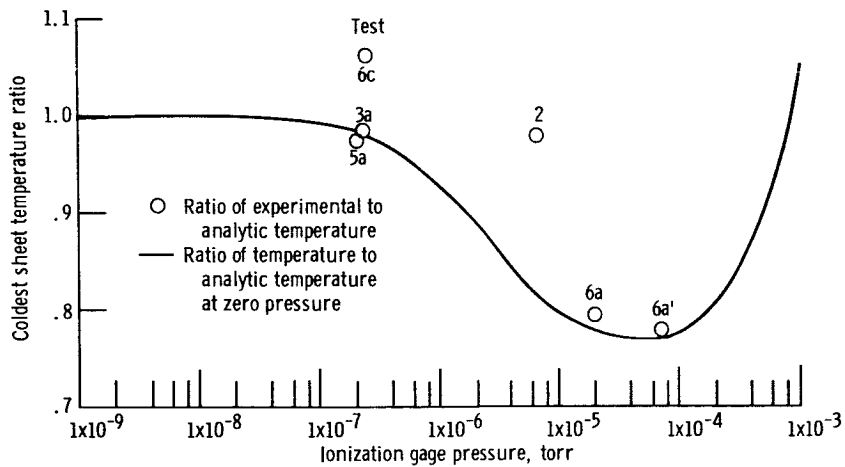
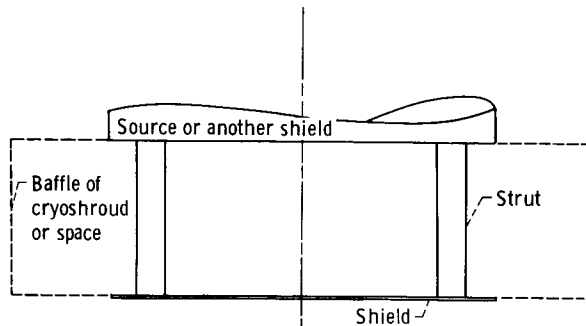
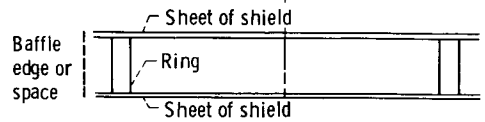


Figure 42. - Effect of pressure inside shroud on centerline temperature for coldest sheet. Room-temperature heater; pressure assumed constant inside shroud.



(a) Enclosure between shield and another surface.



(b) Enclosure between sheets of a shield.

Figure 43. - Schematic of the two types of enclosures used in analysis.

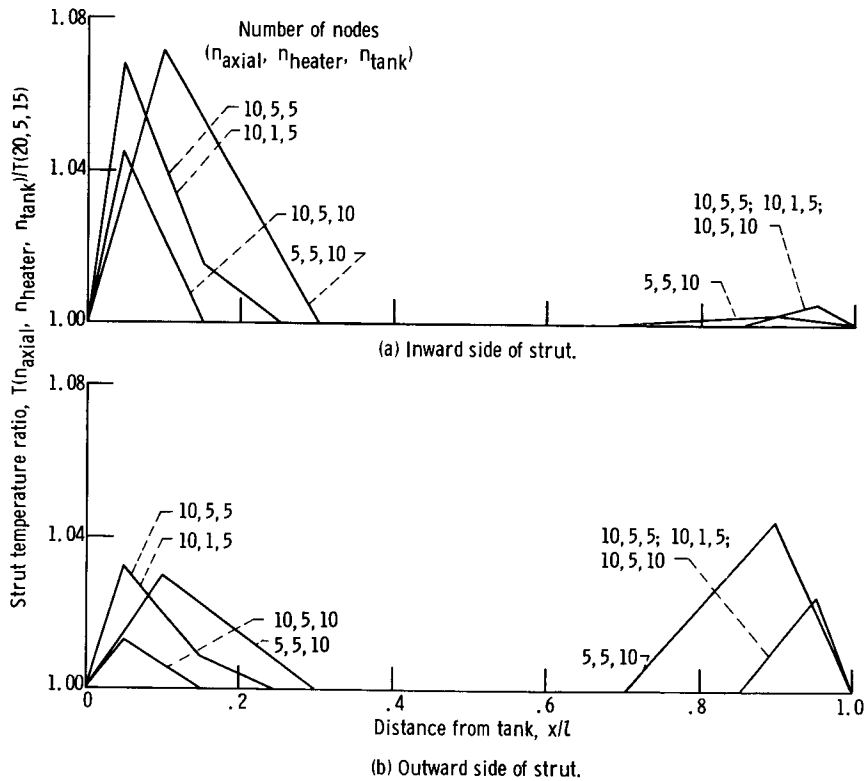


Figure 44. - Effect of number of nodes on analytic temperature profile for all-black fiber-glass strut with no shields. Heater temperature, 389 K (700° R); hydrogen in tank.

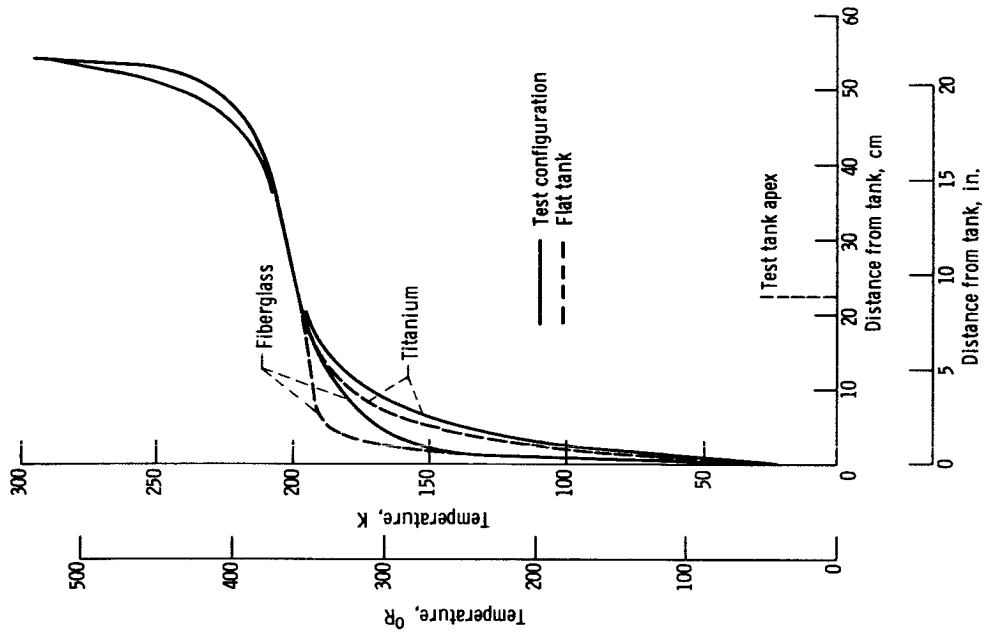


Figure 46. - Effect of tank geometry on temperature profiles of all-black struts with no shields. Strut length, 54.1 centimeters (21.3 in.); heater temperature, 294 K (530° R); hydrogen in tank.

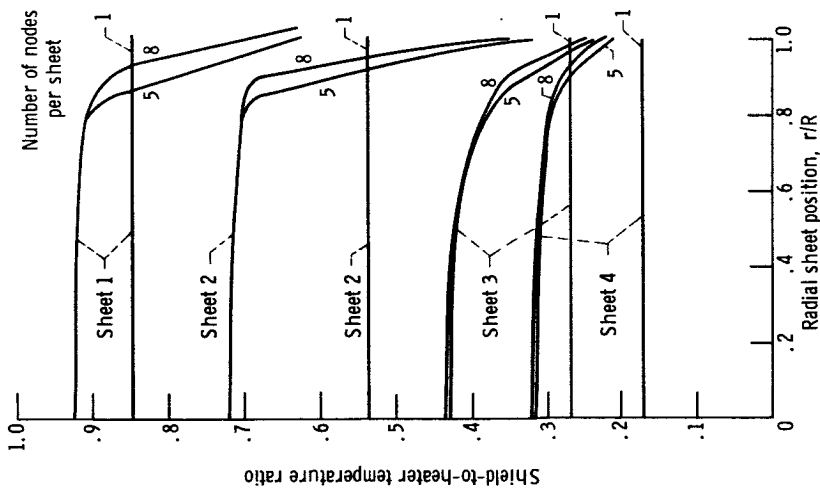


Figure 45. - Effect of number of sheet nodes on temperature profile. Evenly spaced shields; sheets disconnected from rings; emissivity, 0.03.

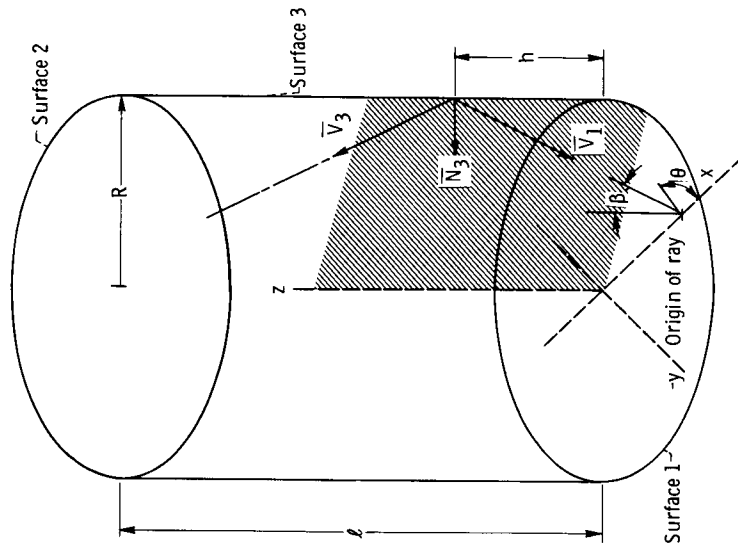


Figure 47. - Schematic for ray-tracing geometry.

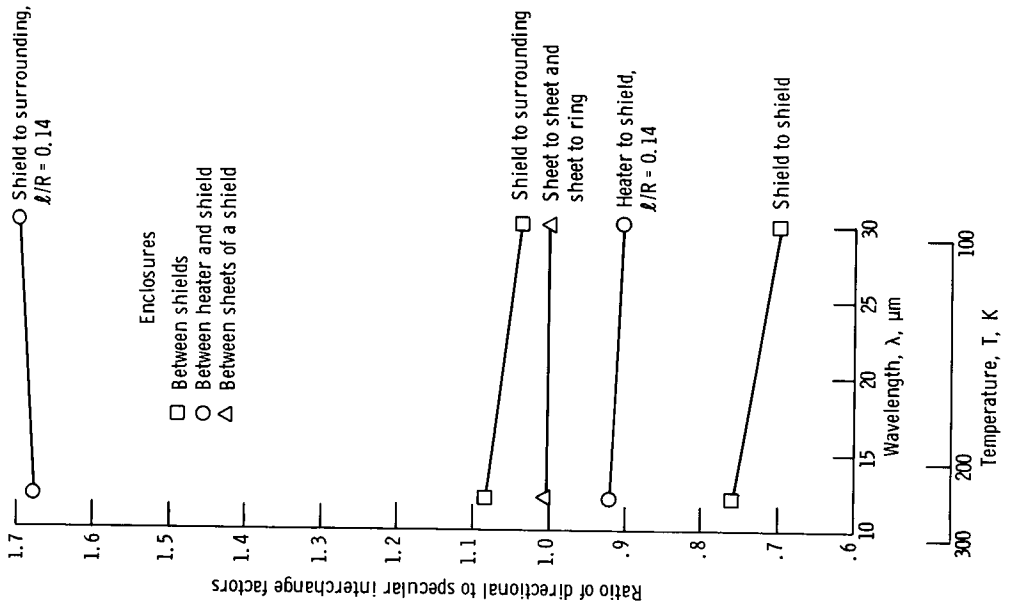


Figure 48. - Directional interchange factor as function of wavelength.

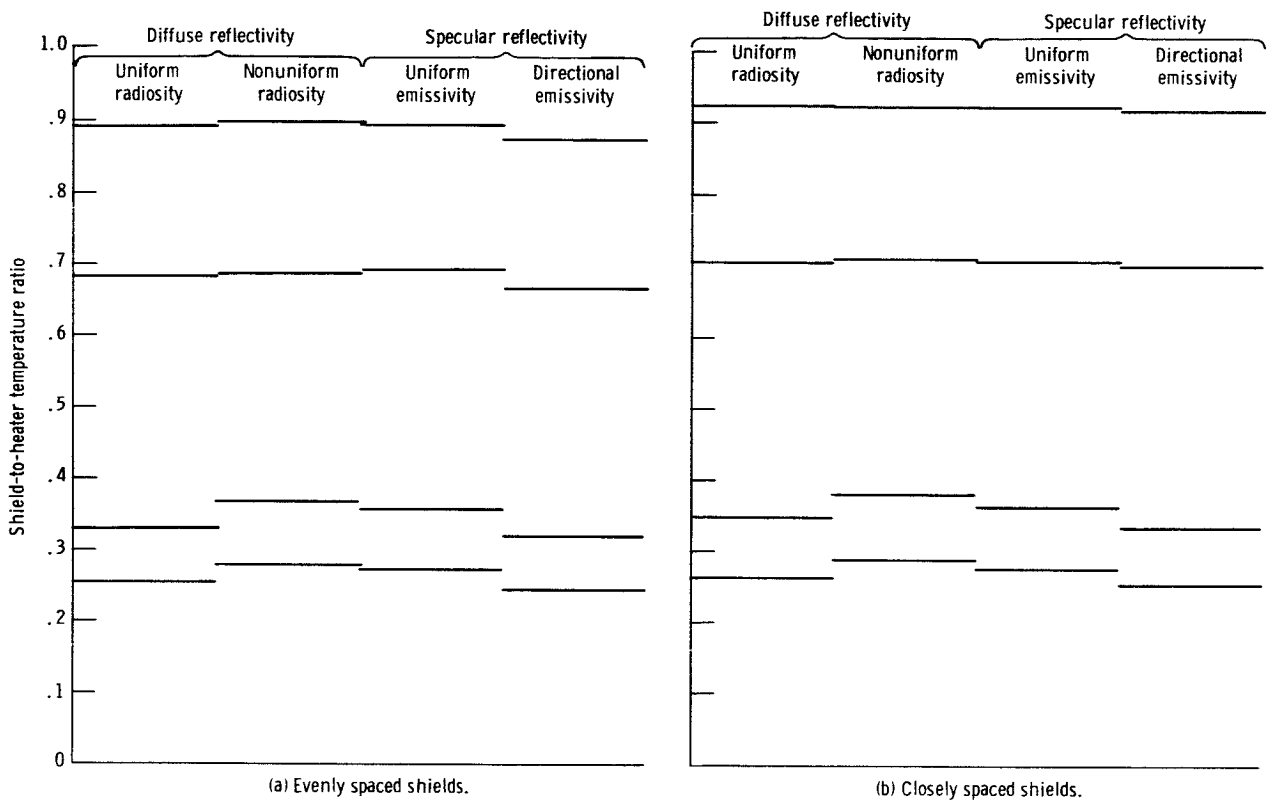


Figure 49. - Isothermal sheet temperatures for different reflectivity assumptions. Emissivity, 0.0245.